

DOE-ET-53088-220

IFSR#220

COMPUTER SIMULATION OF DRIVEN ALFVÉN WAVES

James L. Geary, Jr.
Institute for Fusion Studies
The University of Texas at Austin
Austin, Texas 78712-1060

April 1986

COMPUTER SIMULATION OF DRIVEN ALFVÉN WAVES

by

JAMES LEONARD GEARY JR., S.B.

DISSERTATION

Presented to the Faculty of the Graduate School of

The University of Texas at Austin

in Partial Fulfillment

of the Requirements

for the Degree of

DOCTOR OF PHILOSOPHY

THE UNIVERSITY OF TEXAS AT AUSTIN

May, 1986

ACKNOWLEDGEMENTS

I would like to express my deepest appreciation to Professor Toshiki Tajima for his enthusiasm and a judicious mixture of freedom to be creative and guidance to be productive. I would like to express my heartfelt gratitude to Dr. Jean-Noel Leboeuf for his unfailing kindness, patience, and support throughout this project. I would like to thank Professor Roger Bengtson for his helpful discussions and friendly advice. I am indebted to Professor William Drummond and Professor James Erskine for serving on my dissertation committee.

I would like to acknowledge Dr. David Ross and Dr. Swadesh Mahajan for their numerous useful comments and suggestions through the course of this work. I would like to express my gratitude for many useful discussions with Dr. Todd Evans, Dr. Yan-Ming Li, Dr. Shioh-Hwa Lin, and Saad Eways on Alfvén wave theory.

I would like to thank Ernest Zaidman for numerous discussions and assistance, especially when we began learning particle simulation. I would like to express my gratitude to Michael Sternberg and Jim Dibble for computer assistance. I would like to thank Suzy Crumley for typing this dissertation. There are many people who have aided in this work, but I can only mention a few here.

TABLE OF CONTENTS

Page	Chapter
I. INTRODUCTION	1
II. MAGNETOINDUCTIVE PARTICLE MODEL FOR STRONGLY MAGNETIZED PLASMAS	8
Part A – Ideas and Algorithm	8
2.1 General Remarks	8
2.2 Guiding Center Electron Motion	13
2.3 Magnetoinductive (Darwin) Model	18
2.4 Time Advancement	29
2.5 Boundary Conditions	34
Part B – Tests of Simulation Model	41
2.6 Dispersion Relations and Normal Mode Analysis	41
2.7 Electromagnetic Dissipation and Fluctuation Spectra	58
2.8 Boundary Effects	75
III. EXCITATION OF KINETIC ALFVÉN WAVES AND ASSOCIATED PLASMA HEATING	82
3.1 Introduction	82

3.2 Theoretical Survey	82
3.3 Driven Alfvén Waves in a Periodic, Uniform Plasma	88
3.4 Driven Alfvén Waves in a Bounded, Uniform Plasma	127
3.5 Driven Alfvén Waves in a Bounded, Nonuniform Plasma	141
IV. SUMMARY AND CONCLUSIONS	168
APPENDIX - Solution for the Transverse Electric Field	172
REFERENCES	180

LIST OF FIGURES

Figure	Page
2.1 Depiction of the bounded simulation model. Particles are moved in the left (active) half of the system shaded above	36
2.2 Shaded area indicates \mathbf{k} -space components that are allowed nonzero values. The wavenumbers $k_{x\max}$ and $k_{y\max}$ are the Nyquist wavenumbers.	39
2.3 Dispersion curves for plasma frequency waves from the $(0, k_y)$ modes.	48
2.4 Power spectrum for the mode $(9, 0)$ from the longitudinal (electrostatic) electric field spectrum.	50
2.5 Comparison of simulation results with theory for ion Bernstein modes.	51
2.6 Shear Alfvén wave dispersion curves comparing simulation results with cold plasma theory.	53
2.7 Dispersion curves for the shear Alfvén wave propagating obliquely to the ambient magnetic field.	54
2.8 Power spectra of the left-polarized magnetic field. The signal in a) is an antenna-driven mode while the signal in b) is from thermal noise.	56
2.9 Ion cyclotron dispersion curves from the $(k_x, 0)$ modes from the transverse electric field spectrum.	59
2.10 Longitudinal electric field fluctuation spectrum.	60
2.11 Magnetic field fluctuation spectrum for propagation vectors both parallel and perpendicular to the magnetic field.	62
2.12 Time-averaged magnetic field fluctuation spectrum for propagation purely parallel to the magnetic field.	69
2.13 Time-averaged magnetic field fluctuation spectrum for propagation purely perpendicular to the magnetic field.	74
3.1 Contour plots of the fields a) B_x , b) B_y , and c) E_{Tz} generated by the antenna	

at $\omega_{pet} = 0$ for a zero-temperature plasma in a doubly periodic system of size $L_x \times L_y = 64\Delta \times 320\Delta$	91
3.2 Contour plots of the fields a) B_x , b) B_y , and c) E_{Tz} for Case 1 of Sec. 3.3 at $\omega_{pet} = 0$	92
3.3 Contour plots of the fields a) B_x , b) B_y , and c) E_{Tz} for Case 1 of Sec. 3.3 at $\omega_{pet} = 13000$	94
3.4 Contour plots of the fields a) E_{Lx} and b) E_{Ly} For Case 1 of Sec. 3.3 at $\omega_{pet} = 13000$	95
3.5 Time evolution of a) total electromagnetic field energies, B) total ion kinetic energies, and c) total electron kinetic energies ending at $\omega_{pet} = 13000$ for Case 1 of Sec. 3.3.	96
3.6 Contour plots of the fields a) B_x , b) B_y , and c) E_{Tz} for Case 2 of Sec. 3.3 at $\omega_{pet} = 6000$	98
3.7 Contour plots of the fields a) E_{Lx} and b) E_{Ly} For Case 2 of Sec. 3.3 at $\omega_{pet} = 6000$	99
3.8 Contour plots of the fields a) B_x , b) B_y , and c) E_{Tz} for Case 2 of Sec. 3.3 at $\omega_{pet} = 16000$	101
3.9 Electron velocity distribution function parallel to the magnetic field at a) $\omega_{pet} = 0$ and b) $\omega_{pet} = 16000$ For Case 2 of Sec. 3.3.	102
3.10 Phase space scatter plots, $x - v_{e\parallel}$, of electrons at a) $\omega_{pet} = 0$ and b) $\omega_{pet} = 16000$ for Case 2 of Sec. 3.3.	103
3.11 Spatial dependence of the electron temperature at a) $\omega_{pet} = 0$ and b) $\omega_{pet} = 16000$ for Case 2 of Sec. 3.3.	104
3.12 Time evolution of a) total electromagnetic field energies, b) total ion kinetic energies, and c) total electron kinetic energies ending at $\omega_{pet} = 16000$ for Case 2 of Sec. 3.3.	105
3.13 Contour plots of the fields a) B_x , b) B_y , and c) E_{Tz} for Case 3 of Sec. 3.3	

at $\omega_{pet} = 24000$	107
3.14 Contour plots of the fields a) E_{Lx} and b) E_{Ly} at $\omega_{pet} = 24000$ for Case 3 of Sec. 3.3.	108
3.15 Electron velocity distribution function parallel to the magnetic field at a) $\omega_{pet} = 0$ and b) $\omega_{pet} = 36000$ for Case 3 of Sec. 3.3.	110
3.16 Spatial dependence of the electron temperature at a) $\omega_{pet} = 0$ and b) $\omega_{pet} = 24000$ for Case 3 of Sec. 3.3.	111
3.17 Spatial dependence of the ion y -temperature T_{iy} at a) $\omega_{pet} = 0$ and b) $\omega_{pet} = 24000$ for Case 3 of Sec. 3.3.	113
3.18 Distribution functions of a) y -component of the ion velocity and b) y -component of the electron $\mathbf{E} \times \mathbf{B}$ velocity at $\omega_{pet} = 24000$ for Case 3 of Sec. 3.3.	115
3.19 Time evolution of a) total electromagnetic field energies, b) total ion kinetic energies, and c) total electron kinetic energies ending at $\omega_{pet} = 36000$ for Case 3 of Sec. 3.3.	116
3.20 Contour plots of the fields a) B_x , b) B_y , and c) E_{Tz} at $\omega_{pet} = 12000$ for Case 4 of Sec. 3.3.	118
3.21 Contour plots of the fields a) E_{Lx} and b) E_{Ly} at $\omega_{pet} = 12000$ for Case 4 of Sec. 3.3.	119
3.22 Contour plots of the fields a) B_x , b) B_y , and c) E_{Tz} at $\omega_{pet} = 19200$ for Case 4 of Sec. 3.3.	120
3.23 Spatial dependence of the electron temperature at a) $\omega_{pet} = 0.0$, b) $\omega_{pet} = 12000$ and c) $\omega_{pet} = 19200$ for Case 4 of Sec. 3.3.	122
3.24 Electron velocity distribution function at times a) $\omega_{pet} = 0.0$, b) $\omega_{pet} = 12000$, and c) $\omega_{pet} = 24000$ For Case 4 of Sec. 3.3.	123
3.25 Time evolution of a) total electromagnetic field energies, b) total ion kinetic energies, and c) total electron kinetic energies ending at $\omega_{pet} = 24000$ for	

Case 4 of Sec. 3.3.	124
3.26 Contour plots of the fields a) B_x , b) B_y , and c) E_{Tz} generated by the antenna at $\omega_{pet} = 0$ for a zero-temperature plasma in a system bounded in the x -direction of size $L_x \times L_y = 32\Delta \times 320\Delta$	125
3.27 Contour plots of the fields a) B_x , b) B_y , and c) E_{Tz} at $\omega_{pet} = 18000$ for Case 1 of Sec. 3.4.	130
3.28 Contour plots of the fields a) E_{Lx} and b) E_{Ly} at $\omega_{pet} = 18000$ for Case 1 of Sec. 3.4.	131
3.29 Electron velocity distribution function to the magnetic Field at a) $\omega_{pe} = 0$ and b) $\omega_{pe} = 72000$ for Case 1 of Sec. 3.4.	132
3.30 Spatial dependence of the electron temperature at a) $\omega_{pet} = 0$ and b) $\omega_{pet} = 72000$ for Case 1 of Sec. 3.4.	133
3.31 Time evolution of a) total electromagnetic field energies, b) total ion kinetic energies, and c) total electron kinetic energies ending at $\omega_{pet} = 72000$ for Case 1 of Sec. 3.4.	135
3.32 Dependence in the increase of the a) total electron kinetic energies and b) total ion kinetic energies on the antenna strength W at $\omega_{pet} = 27000$ for Case 1 of Sec. 3.4.	138
3.33 Time evolution of a) total electromagnetic field energies, B) total ion kinetic energies, and c) total electron kinetic energies ending at $\omega_{pet} = 26400$ for Case 2 of Sec. 3.4.	140
3.34 Spatial variation of the Alfvén speed v_A for Case 1 of Sec. 3.5.	143
3.35 Contour plots of the fields a) B_x , b) B_y , and c) E_{Tz} generated by the antenna at $\omega_{pet} = 0$ for a zero- temperature plasma in a system bounded in x of size $L_x \times L_y = 64\Delta \times 320\Delta$	145
3.36 Contour plots of the magnetic field component B_x at a) $\omega_{pet} = 0$, b) $\omega_{pet} = 6000$, and c) $\omega_{pet} = 9000$ for Case 1 of Sec. 3.5.	146

3.37	Spatial dependence and temporal evolution of the field energy densities a) $ E_{Tz}(x, k_A, t) ^2$, b) $ B_x(x, k_A, t) ^2$ and c) $ E_{Ly}(x, k_A, t) ^2$ from different perspectives ending at $\omega_{pet} = 54000$ for Case 1 of Sec. 3.5.	148
3.38	Electron velocity distribution function parallel to the magnetic field at a) $\omega_{pet} = 0$, b) $\omega_{pet} = 12000$, c) $\omega_{pet} = 24000$, and d) $\omega_{pet} = 36000$ for Case 1 of Sec. 3.5.	150
3.39	Spatial dependence of the electron temperature at a) $\omega_{pet} = 0$, b) $\omega_{pet} = 12000$ c) $\omega_{pet} = 24000$, and d) $\omega_{pet} = 36000$ for Case 1 of Sec. 3.4.	151
3.40	Time evolution of the a) total electromagnetic field energies, b) total ion kinetic energies, and c) total electron kinetic energies ending at $\omega_{pet} = 54000$ for Case 1 of Sec. 3.5.	155
3.41	Contour plots of the fields a) B_x , b) B_y , and c) E_{Tz} generated by the antenna at $\omega_{pet} = 0$ for a zero-temperature plasma in a system bounded in the x -direction of size $L_x \times L_y = 128\Delta \times 320\Delta$	157
3.42	Contour plots of the magnetic field component B_x at a) $\omega_{pet} = 6000$ and b) $\omega_{pet} = 9000$ for Case 2 of Sec. 3.5.	158
3.43	Spatial dependence and temporal evolution of the field energy densities a) $ B_x(x, k_A, t) ^2$, b) $ E_{Ly}(x, k_A, t) ^2$, and c) $ E_{Tz}(x, k_A, t) ^2$ from different perspectives ending at $\omega_{pet} = 18000$ for Case 2 of Sec. 3.5.	159
3.44	Spatial dependence of the electron temperature at a) $\omega_{pet} = 0$ and b) $\omega_{pet} = 18000$ for Case 2 of Sec. 3.5.	160
3.45	Contour plots of the magnetic field component B_x at a) $\omega_{pet} = 0$ and b) $\omega_{pet} = 4800$ for Case 3 of Sec. 3.5.	162
3.46	Spatial dependence and temporal evolution of the field energy densities a) $ B_x(x, k_A, t) ^2$, b) $ E_{Ly}(x, k_A, t) ^2$, and c) $ E_{Tz}(x, k_A, t) ^2$ from different perspectives ending at $\omega_{pet} = 19200$ for Case 3 of Sec 3.5.	164
3.47	Electron velocity distribution function parallel to the magnetic field at a)	

$\omega_{pet} = 0$ and b) $\omega_{pet} = 19200$ For Case 3 of Sec. 3.5.	165
3.48 Time evolution of a) total electromagnetic field energies, b) total ion kinetic energies, and c) total electron kinetic energies ending at $\omega_{pet} = 19200$ for Case 3 of Sec. 3.5.	166

CHAPTER 1. INTRODUCTION

The resonant interaction of driven Alfvén waves with a magnetized plasma is studied using particle simulation. Alfvén waves have proven to be important in the description of a wide variety of plasma phenomena since H. Alfvén¹ predicted their existence in 1942. currently there is great interest in their use for heating magnetically confined plasmas. This has direct application for magnetic confinement fusion and is also of importance to space plasmas. A full kinetic treatment of Alfvén waves in a magnetized nonuniform plasma is a difficult theoretical problem to investigate analytically. Thus this research delves into Alfvén wave phenomena in nonuniform, nonideal magnetized plasmas.

It is well known that a plasma has to achieve a temperature sufficient for the fusion reaction to occur. One way to heat a plasma in a magnetic confinement system is to pass a current through the plasma. This method, called Ohmic heating, may not by itself be sufficient to achieve an ignition temperature. The plasma resistivity decreases as the temperature increases, thus reducing the effectiveness of Ohmic heating. The search for the best alternate methods is active at present. One of the promising areas of study is radio frequency (RF) electromagnetic wave heating. These generally involve coupling an external source of RF energy to a wave resonance within the plasma. Some of the candidates are electron cyclotron resonance heating, lower hybrid heating, ion cyclotron resonance heating, and Alfvén wave heating.

The Alfvén wave heating scheme was originally conceived as a method where a radio frequency wave, launched at the edge of the plasma, propagates from the edge until it couples its energy to plasma particles in the vicinity of the shear Alfvén resonance layer. A few of the advantages

are: 1) power supplies for this frequency range (Megahertz) are comparatively inexpensive and readily available, 2) coupling to remote sources reduces radiation damage, 3) this scheme is predicted to be an efficient way to heat the plasma interior, and 4) there is evidence that particle confinement improves possibly because the applied RF waves exert a ponderomotive force on the plasma. There are several potential problems that must be solved before this scheme is practical. First there may be difficulty in effectively coupling the RF energy to the plasma edge, particularly at the power levels required. Secondly, the manner in which the wave propagates to the resonance layer must be known. Finally, the processes by which the wave energy is absorbed by the plasma must also be elucidated. Understanding these dissipative processes is emphasized in this dissertation.

Using Alfvén waves to heat plasmas was first suggested by Dolgoplov and Stepanov.^{2,3} They examined compressional Alfvén wave heating for a cylindrical plasma and determined under what conditions heating can occur. Plasma heating using the shear Alfvén resonance was independently proposed by Hasegawa and Chen⁴ and by Tataronis and Grossman.⁵ In a non-uniform plasma, there exists a singularity in the ideal magnetohydrodynamic (MHD) equations associated with the shear Alfvén resonance in the continuum, $\omega = k_{\parallel}v_A$. At the singular point, the wave can propagate only along the magnetic field lines and the wave energy accumulates at the resonance layer, which must eventually be dissipated.

Further MHD calculations have been applied to cylindrical geometry^{6,7} with corrections for toroidal and ellipticity⁸ effects and for finite ion cyclotron frequency⁹ effects by the Lausanne group. Their analyses indicate that the optimum heating efficiency occurs when the pump generates a collective mode of the plasma response. The inclusion of toroidicity in-

creases the power deposition at the edge but does not otherwise significantly change the qualitative features at the cylindrical model. Plasma ellipticity may have a detrimental effect on the heating scheme. The incorporation of finite ion cyclotron frequency effects moves the resonant layer closer to the plasma edge. This is expected to be more significant for present experiments than for a fusion reactor. The problem was investigated with kinetic effects including finite electron inertia, finite ion Larmor radius, and collisions by Hasegawa and Chen.^{10,11} Various damping mechanisms both collisional and collisionless were examined in detail. Ross, Chen, and Mahajan¹² developed a numerical model that included important kinetic effects and realistic tokamak parameters in a cylindrical geometry. Their results indicate that the wave can penetrate to the resonance region and heat the interior of the plasma if the plasma is sufficiently warm. Finite electron inertia effects in their model introduce a surface wave not predicted by the MHD model. The presence of equilibrium currents with finite ion cyclotron frequency effects and curvature are seen to lead to a discrete spectrum of global Alfvén eigenmodes^{9,12,13} (GAE) whose eigenfrequency ω is less than the minimum shear Alfvén resonant frequency of the plasma.

Early experiments performed on low temperature stellarator-like devices in the mid-to-late 1970s demonstrated the viability of Alfvén wave heating. Results from the Proto-Cleo Stellarator^{14,15} displayed a doubling of both the ion and electron temperatures. Electron heating profiles were broad with some enhancement near the resonance regions. Similar heating results were reported on Heliotron-*D* by Obiki et al.¹⁷ along with an improvement in plasma confinement. They demonstrated a dependence of the heating rate on the initial electron temperature. Experiments on the R0-2 stellarator by Demirkhanov et al.¹⁷ find that the plasma was stabilized

when the RF was applied.

A number of Alfvén wave heating experiments are currently being conducted on tokamaks. The most comprehensive experimental study of Alfvén wave heating has been performed on the TCA Tokamak in Lausanne.¹⁸⁻²¹ Substantial electron and ion heating has been observed. The temperature increase for both species scales linearly with input RF power. The mechanism for the ion heating is, however, not understood. The plasma confinement improves with the application of RF energy. Their experiment experienced substantial problems with impurities that have recently improved with a new antenna design.

Measurements of the antenna impedance^{18,22} are dominated by peaks in the frequency spectrum identified with the GAE's. The structure of the driven GAE's in the PRETEXT tokamak has been measured by Evans²² et al. using CO_2 laser interferometry. The GAE mode resonances dominate the driven density fluctuation spectrum in PRETEXT. A direct observation of the kinetic Alfvén resonance by probe measurements of the magnetic field has been reported by Witherspoon et al.²³ on the TOKAPOLE-II tokamak.

The physics of the shear Alfvén resonance is expected to be of importance for space plasmas. It has been proposed by Ionson²⁴ that resonantly excited kinetic Alfvén waves help dissipate hydromagnetic energy in solar coronas leading to the heating of coronal loops. In geomagnetic plasmas Kinetic Alfvén waves may also be responsible for particle acceleration along auroral field lines (Goertz²⁵).

A plasma heating study involves both the wave dynamics, the plasma particle dynamics and the interaction between these in a self-consistent and often fully nonlinear fashion. Thus a full description requires a kinetic self-consistent investigation as is offered by particle simulation meth-

ods. In addition to theory and experiment, particle simulations in fact have been used to examine *RF* heating. Electron cyclotron and upper hybrid resonance heating (ECRH) has been studied by Lin et al.²⁶⁻²⁸ and by Smith et al.²⁹ using a 1-dimensional electromagnetic particle code. The lower hybrid frequency range has been studied by (Decyk et al.^{30,31}, Abe et al.³², and Nakajima et al.³³) retaining only electrostatic effects in the simulation. Some work has been done in the ion cyclotron frequency regime (Busnardo-Neto et al.³⁴, Kindel et al.³⁵, Abe et al.³⁶, and Sakai et al.³⁷). Lin et al.²⁶, examining the upper hybrid resonance heating using a fully self-consistent electromagnetic simulation, first confirmed the mode conversion of the incoming upper hybrid electromagnetic wave into mostly electrostatic cyclotron (Bernstein) waves. On the other hand, at the corresponding ion branches, the predicted mode conversion of the compressional Alfvén waves into mostly electrostatic ion cyclotron (ion Bernstein) waves has been more elusive due to its lower frequency and thus greater computing demand and also because of the noise due to electron motion in the code. However, recently Abe et al.³⁶ and Sakai et al.³⁷ have been able to confirm this conversion at the ion cyclotron waves via the technique of spectrum interferometry in fully self-consistent simulation.

A study has not yet been carried out to date to our knowledge on the Alfvén wave heating by a fully self-consistent nonlinear electromagnetic particle simulation. In particular, confirmation of mode conversion of the resonant shear Alfvén wave has not yet been made in a particle simulation. Similarly confirmation by particle simulation of the kinetic Alfvén wave resonance keeping electron motion has not yet been reported, either. Nor has any study of heating processes due to this method been investigated via the particle simulation. There are a few reasons why this has not

been done to date. One is that in order to carry out this investigation, it is almost mandatory to develop a plasma simulation model which (i) includes electromagnetic interaction in the range of Alfvén wave frequencies but dispenses with phenomena at much higher frequencies for efficiency of the simulation algorithm and (ii) removes the excessive electron noise that buries the ion response such as the ion cyclotron waves. This requires a sophisticated code development that has not been previously done to date. The required features of the code are: (i) self-consistent electromagnetic fields that are calculated efficiently, perhaps with Maxwell's equation without the transverse displacement current (Darwin's model), (ii) treating the electron gyromotion in a guiding center approximation to remove the high-frequency response, (iii) the presence of compressional and shear Alfvén waves and kinetic effects associated with them, including the finite Larmor radius effects. These requirements lead us to the adoption of the algorithm and development of the code featured in this dissertation, as described in the subsequent chapter.

Through this investigation, we present the first attempt to apply a fully nonlinear self-consistent electromagnetic particle simulation code to the Alfvén wave resonance heating and to confirmation of the Alfvén wave mode conversion. Particle simulation codes follow the temporal evolution of the problem while self-consistently including kinetic effects and nonlinearities. Earlier theoretical investigations have mostly examined the linear, stationary response of the plasma to an antenna. However, some of the experimental results are not easily understood from such linear, stationary analyses. A primary goal of this work is to pinpoint important areas that may not have received sufficient attention thus far.

Since it is difficult to represent all the aspects of a confinement device in a computer model, it becomes necessary to idealize the geometry and reduce the spatial scales to lengths manageable in a computer model. In the following model which we adopt, the time scales that can be examined are short compared to experimental operation times. Thus a study of only basic processes is given here, which provides a restricted but detailed view of the problem.

The standard particle simulation codes available to us either used too much computer time for the problem to evolve or did not incorporate enough physics in the model. For this purpose, a new computer model was developed that incorporates a massless guiding center model for electron motion perpendicular to the magnetic field with Darwin's radiationless (magnetoinductive) model for the electric and magnetic fields. The details of this model are discussed in part A of Chapter 2. Tests confirming the validity of the model are presented in part B of Chapter 2. Following a review of Alfvén wave theory emphasizing those aspects believed to be relevant to the present work, the reaction of the simulation plasma to an external source of RF energy, whose frequency is in the Alfvén wave frequency range, is presented in a number of case studies in Chapter 3. The details of the wave dynamics, heating processes, and the effects the wave has on the plasma properties are examined when the plasma is homogeneous and when an inhomogeneity is introduced by varying the magnetic field. Finally, Chapter 4 presents a summary and conclusion of the work.

CHAPTER 2. MAGNETOINDUCTIVE PARTICLE MODEL FOR STRONGLY MAGNETIZED PLASMAS

Part A — IDEAS AND ALGORITHM

2.1 General Remarks

With the development of more powerful computers, computational investigation has proven to be an increasingly important tool for understanding physical systems. There are many problems for which analytic methods are too complex to be practical. This occurs in nonlinear plasma physics where the interaction forces between particles are well known but the collective behavior of a large assembly of particles is often not known.

The Lorentz force law for particle motion and Maxwell's equations for the electric and magnetic fields describe most of the phenomena in plasma physics. Particle simulation models a plasma at this fundamental level. In these codes, the motion of a collection of charged particles is followed in their self-consistent electric and magnetic fields. Particle simulation techniques applied to plasma physics are discussed by Birdsall and Langdon³⁸ and by Hockney and Eastwood.³⁹ Hockney and Eastwood³⁹ discuss further applications of particle simulation to areas outside of plasma physics. A review article by John Dawson⁴⁰ gives a good description of the philosophy of the computer simulation model described here.

Because of limitations on the size and speed of computers, simulation plasmas contain far fewer particles than corresponding physical systems. Collisional effects would thereby be enhanced in the simulation model. However, it was an important realization in the 1960's that the effects of collisions can be decreased by the use of "finite size" particles, which are allowed to interpenetrate each other. Essentially collisionless behavior can be successfully modelled by particle simulation codes with only a few particles in

a Debye sphere. The interaction force between a pair of finite size particles remains approximately the same as between a pair of point particles for separations larger than the finite particle size but is diminished as the finite size particles overlap. Since the long range forces dominate collective effects, collective forces can thus be realistically simulated.

The force felt by a particle is not directly calculated from binary encounters with all of the other particles in the simulation system. Instead, the force is computed on a spatial grid for computational efficiency. The simulation volume is divided into cells which are typically about the size of the particles. The centers of these cells form a spatial mesh or grid. Source terms, such as the charge density, for the field equations are calculated on the grid from knowledge of the nearby particle positions and velocities. The charge density, current density, etc., represented by a finite-size particle is distributed by some weighting scheme to nearby grid points. Standard numerical methods are used to solve the field equations on the grid. The force felt by a particle is then determined by interpolation from nearby grid points to the particle position, usually by the same weighting scheme.

An electrostatic particle model will be described as an example. The simulation particles are assigned initial positions and velocities. At the first time step, the charge density is accumulated at the grid points from charge weighting of adjacent particles. The electric fields are then calculated on the grid from the charge density. The acceleration of the particles is interpolated from the field values of nearby grid points. The particle velocities are incremented forward in time from the finite differenced force equation. The particle positions are similarly stepped forward in time once the particle velocities are known. At this stage, the computational cycle begins again with the accumulation of the new charge density at the

grid points. This cycle is repeated hundreds or thousands of times as the simulation evolves.

There are many possible techniques that can be used to solve the field equations on the grid once the sources are known. One particularly convenient technique makes use of the Fast Fourier Transform (FFT). Spatial differential operators in the field equations are replaced by simple multiplications when the field equations are transformed from configuration space to Fourier \mathbf{k} -space. After the solutions are obtained in the Fourier representation, the fields can be inverse transformed back to configuration space. The main advantages of using the FFT are speed and accuracy. The number of operations to compute a Fourier transform using the FFT is proportional to $n \log(n)$ where n is the number of grid points. Fourier transform methods are employed to solve the field equations because they are fast and relatively easy to use.

Considerable thought was given to the choice of the appropriate particle code model for the problem addressed in this dissertation. One important criterion for the model is that all necessary physical effects are incorporated. Some elements which we deemed important to include are finite ion Larmor radius effects, electron Landau damping, and low frequency electromagnetic waves. A typical choice might be a standard fully electromagnetic particle code. This follows the relativistic Lorentz particle motion and solves the full set of Maxwell's equations. In order for these models to remain stable, the time step, Δt , must satisfy the criteria

$$\omega_{pe} \Delta t < 1$$

$$\Omega_e \Delta t < 1$$

$$kc \Delta t < 1$$

where ω_{pe} is the plasma frequency and Ω_e is the electron cyclotron frequency. However, the frequencies of Alfvén waves are normally much lower than either the plasma frequency or the electron cyclotron frequency. The conventional electromagnetic particle codes are thus very expensive to use on this problem because of the many time steps needed to progress forward one Alfvén period.

There are many problems in plasma physics where low frequency behavior is sensitively dependent on the details of individual particle motion. The development of different algorithms that allow substantial increases in the time step without compromising the simulated physics is an active field of research, (Lee and Okuda,⁴¹ Mason,⁴² Denavit,⁴³ and Barnes et al.⁴⁴). One example is the development of an electrostatic code with an averaging of the electron gyromotion (Lee and Okuda⁴¹). The electron motion in the plane perpendicular to the magnetic field is treated in a massless guiding center approximation.

The computational model that we found most suitable for this application combined Darwin's⁴⁵ magnetoinductive model for the electric and magnetic fields with a guiding center scheme for electron motion perpendicular to the magnetic field. The magnetoinductive approximation eliminates light wave propagation. The electromagnetic codes often have excessive bremsstrahlung radiation because the greater particle discreteness results in larger current fluctuations than is physically realistic. The magnetoinductive model is nonradiative in character and thus has a lower overall background noise level while retaining self-consistent electric and magnetic fields. Both radiation and the full details of the electron gyromotion are assumed not to be necessary for the description of Alfvén waves or of the important dissipa-

tion processes. The restrictions on the time step,

$$kc\Delta t < 1$$

$$\Omega_e\Delta t < 1$$

thus are not applicable here. The most important restrictions remaining on the time step are

$$\frac{k_{\parallel}}{k}\omega_{pe}\Delta t \lesssim 0.5 \quad (2.1a)$$

$$\omega_{pi}\Delta t \lesssim 0.5 \quad (2.1b)$$

$$\Omega_i\Delta t \lesssim 0.25 \quad (2.1c)$$

$$v_{\max}\Delta t \lesssim \Delta x. \quad (2.1d)$$

This model is powerful when the condition $k_{\parallel} \ll k_{\perp}$ applies. A simpler version, which neglects compressional Alfvén waves, has been used by Lee et al.⁴⁶ to investigate anomalous transport due to shear Alfvén waves.

Most other numerical models either were too slow or neglected some important pieces of physics. One possibly feasible alternative is presented by the implicit electromagnetic codes.⁴⁴ The implicit schemes are, in principle, stable for any value of the time step. The implicit methods are, however, still in the research stage. It has not been determined yet which particular algorithm is most suitable nor is it fully known what is their operable parameter range. The successful description of the kinetic Alfvén wave requires the full resolution of the ion cyclotron motion. This probably limits the time step of the implicit electromagnetic codes to the same range of values as the model used here.

The particle simulation code employed in this dissertation has $2\frac{1}{2}$ dimensions, i.e., two spatial coordinates (x, y) and three velocity components (v_x, v_y, v_z) . The finite size particles, or quasi particles, act like charged

rods extending to $\pm\infty$ in the z -direction. All quantities are presumed homogeneous in the z -direction. The background magnetic field vector lies in the $y - z$ plane. Most of the heating results were obtained with a code that is bounded in the x -direction. Some of the test results are from a code that is periodic in both the x - and y -directions.

The remaining sections of part A discuss and describe these elements of the computational model in detail; the electron guiding center motion, Darwin's model with descriptions of the electric and magnetic field solutions, the time differencing and algorithm, the boundary conditions, and the initial conditions. Part B discusses the tests of the validity of the model. These concentrate on the properties of the homogeneous plasma in thermal equilibrium. The electric and magnetic field mode structures from thermal fluctuations are checked with plasma theory and the mode dispersion is checked with the fluctuation-dissipation theorem.

2.2 Guiding Center Electron Motion

The nonrelativistic Lorentz force law for a point particle of species α is given by

$$m_\alpha \frac{d\mathbf{v}_\alpha}{dt} = q_\alpha \mathbf{E} + q_\alpha \frac{\mathbf{v}_\alpha}{c} \times \mathbf{B}. \quad (2.2)$$

This force law is modified in the simulation to encompass the finite size of the quasiparticles. The field acceleration must be integrated over the charge distribution of the quasiparticles. The concepts for quasiparticle motion will be deduced using the simpler equations of motion for point particles. Once developed, the model will be extended to include finite size particle effects. The electron motion in the model is not described by the full Lorentz force law, instead a guiding center drift approximation is utilized. The approximations and implications of the electron motion are discussed here.

Magnetic confinement fusion devices are characterized by strong magnetic fields externally applied. There can be various levels in a hierarchy of time scales for a magnetized plasma. For a typical case the time scale of the electron gyromotion is the shortest (or one of the shortest) time scales. When one is interested in a phenomenon of a time scale much longer than this, it is convenient to treat this motion by the guiding center model (Alfvén⁴⁷). The usual mathematical formulation of the guiding center motion assumes that the scale lengths of spatial variation of the surrounding electric and magnetic fields are much longer than the gyroradius ($k\rho \ll 1$) and that the frequencies of interest are much less than the gyrofrequency ($\omega \ll \Omega$). The approximations $\omega \ll \Omega_e$ and $k\rho_e \ll 1$ are normally quite valid for the Alfvén wave heating scheme.

The leading terms up to $\mathcal{L}(\omega/\Omega)$ for drift motion perpendicular to the magnetic field are

$$\mathbf{v}_{D\perp} = \frac{c\mathbf{E} \times \hat{b}}{B} - \left[\frac{v_{\parallel}^2}{\Omega} (\hat{b} \cdot \nabla) \hat{b} + \frac{v_{\perp}^2}{2B\Omega} \nabla B \right] \times \hat{b} + \frac{c}{\Omega B} \frac{d\mathbf{E}_{\perp}}{dt}, \quad (2.3)$$

where \hat{b} is unit vector of the magnetic field. The first term on the right-hand side of Eq. (2.3) is identified with the $\mathbf{E} \times \mathbf{B}$ drift, the second term with the curvature drift, the third term with the ∇B drift and the last term with the polarization drift. Only the guiding center motion from the $\mathbf{E} \times \mathbf{B}$ drift is kept in our models. The curvature drift will not be a factor because of the geometry of the problem. The polarization drift velocity compared to the $\mathbf{E} \times \mathbf{B}$ drift velocity is smaller by $\mathcal{L}(\omega/\Omega_e)$. The polarization term is consequently neglected in our model, since frequencies of interest are much smaller than the electron cyclotron frequency. The ∇B drift term is also neglected. If the model is restricted to the low- β regime, $\beta = 8\pi n_0(T_i + T_e)/B^2$, gradients of the magnetic field are much smaller than gradients of

the electric field thus reducing the magnitude of the ∇B drifts. The last three drift terms on the right side of Eq. (2.3) arise from the finite inertia of the particles. The $\mathbf{E} \times \mathbf{B}$ drift is independent of the particle mass. Therefore, this model uses massless perpendicular guiding center drift motion for electrons. In the low- β approximation, it is presumed that the plasma contribution to the magnetic field is negligible compared to the background magnetic field in the way that it affects the drift motion. This approximation reduces the computational complexity.

The electron motion parallel to the background magnetic field retains full dynamics. Thus parallel kinetic effects resulting from finite electron inertia are retained. The resulting equations of motion for electrons are

$$\frac{dv_{e\parallel}}{dt} = -\frac{e}{m}\mathbf{E}_{\parallel} \quad (2.4)$$

$$\mathbf{v}_{e\perp} = \frac{c}{B_0^2}\mathbf{E} \times \mathbf{B}_0 \quad (2.5)$$

$$\frac{d\mathbf{x}_e}{dt} = \mathbf{v}_e, \quad (2.6)$$

where $\mathbf{E}_{\parallel}(\mathbf{x}) = \hat{b}(\mathbf{x}) \left[\hat{b}(\mathbf{x}) \cdot \mathbf{E}(\mathbf{x}) \right]$ and where $\hat{b}(\mathbf{x}) = \mathbf{B}_0(\mathbf{x})/B_0(\mathbf{x})$. The ion motion in this code model is governed by the full nonrelativistic Newton-Lorentz equations of motion

$$\frac{d\mathbf{v}_i}{dt} = \frac{e}{M}\mathbf{E} + \frac{e}{Mc}\mathbf{v}_i \times \mathbf{B} \quad (2.7)$$

$$\frac{d\mathbf{x}_i}{dt} = \mathbf{v}_i. \quad (2.8)$$

This model contains the essential ingredients of particle motion for simulation of Alfvén wave heating processes. The $\mathbf{E} \times \mathbf{B}$ motion of the electrons is necessary for the existence of Alfvén waves. Electron Landau damping, which is expected to be a primary heating mechanism is included in our model. The

Alfvén wave period and the ion gyrofrequency are not sufficiently removed from each other for the treatment of ions. Moreover, finite ion Larmor radius effects influence the character of the kinetic Alfvén wave.

Finite size particle effects will now be included in the dynamical equations. Integrating over the quasiparticle charge yields the following form of the ion Lorentz force equation

$$m_{pi} \frac{d\mathbf{v}_j}{dt} = q_{pi} \int_V S(\mathbf{x}' - \mathbf{x}_j) \left[\mathbf{E}(\mathbf{x}') + \frac{\mathbf{v}_j}{c} \times \mathbf{B}(\mathbf{x}') \right] d\mathbf{x}' \quad (2.9)$$

where m_{pi} and q_{pi} are the ion quasiparticle mass and charge. The conservation of charge and mass in the simulation require that

$$q_{pi} = \frac{en_0V}{N_0}$$

$$m_{pi} = \frac{Mn_0V}{N_0}$$

where n_0 is the average physical number density, N_0 is the number of finite size ions in the simulation, and V is the simulation volume. For a $2\frac{1}{2}D$ (dimension) slab model, V is given by

$$V = L_x L_y.$$

It follows that the finite size electron charge and mass are

$$q_{pe} = -\frac{en_0V}{N_0}$$

$$m_{pe} = \frac{mn_0V}{N_0}.$$

The variable $S(\mathbf{x})$ is the shape factor that describes the quasiparticle charge and mass distribution. The simulation model uses Gaussian-shaped particles, whose explicit form is

$$S(\mathbf{x}) = \frac{1}{2\pi a_x a_y} \exp\left(-\frac{x^2}{2a_x^2} - \frac{y^2}{2a_y^2}\right) \quad (2.10)$$

for a particle located at the origin. The mean widths of the quasiparticles are a_x and a_y . The position of the finite size particle refers to the particle center. Application of the Fourier transform allows the integral to display a more computationally convenient form. The one-dimensional Fourier transform of a function E that is periodic over length L_x is defined by

$$\mathbf{E}(x) = \sum_{m=-\infty}^{\infty} \mathbf{E}(k_m) e^{ik_m x}$$

where

$$k_m = \frac{2\pi m}{L_x}.$$

The inverse Fourier transform is given by

$$\mathbf{E}(k) = \frac{1}{L_x} \int_0^{L_x} \mathbf{E}(x) e^{-ikx} dx.$$

To generalize these definitions to any dimension, we use the notation

$$\mathbf{E}(\mathbf{x}) = \sum_{\mathbf{k}} \mathbf{E}(\mathbf{k}) e^{i\mathbf{k}\cdot\mathbf{x}} \quad (2.11)$$

and

$$\mathbf{E}(\mathbf{k}) = \frac{1}{V} \int_V \mathbf{E}(\mathbf{x}) e^{-i\mathbf{k}\cdot\mathbf{x}} d\mathbf{x} \quad (2.12)$$

for the periodic Fourier transform and its inverse. Using the Fourier expansion of $S(x)$, $\mathbf{E}(\mathbf{x})$, and $\mathbf{B}(\mathbf{x})$, the force equation (2.10) can assume the form

$$\begin{aligned} \frac{d\mathbf{v}_j}{dt} &= \frac{e}{M} \sum_{\mathbf{k}} V S(-\mathbf{k}) \left[\mathbf{E}(\mathbf{k}) + \frac{\mathbf{v}_j}{c} \times \mathbf{B}(\mathbf{k}) \right] e^{i\mathbf{k}\cdot\mathbf{x}_j} \\ &= \frac{e}{M} FFT^{-1} [V S(-\mathbf{k}) \mathbf{E}(\mathbf{k})] + \frac{e}{M} \frac{\mathbf{v}_j}{c} \\ &\quad \times \{ FFT^{-1} [V S(-\mathbf{k}) \mathbf{B}(\mathbf{k})] \}. \end{aligned} \quad (2.13)$$

If we define an electric force \mathbf{F}_E and a magnetic force \mathbf{F}_B by

$$\mathbf{F}_E(\mathbf{k}) = V S(-\mathbf{k}) \mathbf{E}(\mathbf{k}) \quad (2.14a)$$

$$\mathbf{F}_B(\mathbf{k}) = V S(-\mathbf{k}) \mathbf{B}(\mathbf{k}), \quad (2.14b)$$

the Lorentz force law for finite size ions reduces to

$$\frac{d\mathbf{v}_j}{dt} = \frac{e}{M} \mathbf{F}_E(\mathbf{x}_j) + \frac{e}{M} \frac{\mathbf{v}_j}{c} \times \mathbf{F}_B(\mathbf{x}_j) \quad (2.15)$$

which is identical in form to the point particle force equation. The arguments given earlier for point particle motion are applicable to finite size particles when the electric and magnetic fields are replaced by their corresponding forces. It is evident that Eqs. (2.4) and (2.5) for point electrons are replaced by

$$\mathbf{v}_{e\perp} = \frac{c}{|\mathbf{F}_B|^2} \mathbf{F}_E \times \mathbf{F}_B \quad (2.16)$$

$$\frac{dv_{e\parallel}}{dt} = -\frac{e}{m} \mathbf{F}_{\parallel} \quad (2.17)$$

where

$$\mathbf{F}_{\parallel}(\mathbf{k}) = VS(-\mathbf{k})\mathbf{E}_{\parallel}(\mathbf{k}),$$

for finite size particles. The expressions for updating the quasiparticle positions remain the same as Eqs. (2.6) and (2.8).

2.3 Magnetoinductive (Darwin) Model

The Darwin⁴⁵ model neglects the transverse displacement current. The original intention of the Darwin model is to obtain the most accurate Lagrangian of the field-particle system as a function of the instantaneous velocities and positions of the particles. Such a Lagrangian must necessarily exclude radiation since its structure implies instantaneous action-at-a-distance. The explicit form of the Lagrangian is not required for present purposes.

The full electromagnetic equations are

$$\nabla \times \mathbf{E}_T = -\frac{1}{c} \frac{\partial \mathbf{B}}{\partial t} \quad (2.18)$$

$$\nabla \times \mathbf{B} = \frac{4\pi}{c} \mathbf{J}_T + \frac{1}{c} \frac{\partial \mathbf{E}_T}{\partial t} \quad (2.19)$$

$$\nabla \cdot \mathbf{E}_L = 4\pi\rho \quad (2.20)$$

$$\nabla \cdot \mathbf{B} = 0 \quad (2.21)$$

where the subscript T denotes the divergence-free (transverse) and where the subscript L denotes the curl-free (longitudinal) components of a vector. With these definitions, \mathbf{E}_L and \mathbf{E}_T satisfy

$$\nabla \times \mathbf{E}_L = \nabla \cdot \mathbf{E}_T = 0.$$

From this point forward, the words longitudinal and transverse will only refer to the curl-free and divergence-free components of a vector. The Darwin approximation drops the $\dot{\mathbf{E}}_T$ term in Eq. (2.19). Ampere's law assumes the form

$$\nabla \times \mathbf{B} = \frac{4\pi}{c} \mathbf{J}_T. \quad (2.22)$$

Magnetic induction from Faraday's law, Eq. (2.18), is still retained. This is why the model is called magnetoinductive rather than magnetostatic.

The magnetoinductive field equations differ by only one term from the full set of Maxwell's equations. This alteration changes the character of the field equations from hyperbolic to elliptic. The ellipticity of the reduced electromagnetic equations increases the difficulty of solving them. The two time derivatives in the full electromagnetic equations can be used to advance them forward in time. A straightforward attempt to finite difference Faraday's law in time to solve for the transverse electric field leads to violent numerical instabilities. The attempt to propagate information at a finite speed implied by the differencing is inconsistent with the nature of the instant action-at-a-distance model. The solution for \mathbf{E}_T proceeds by eliminating the magnetic field from Eqs. (2.18) and (2.22) to obtain

$$\nabla^2 \mathbf{E}_T = \frac{4\pi}{c^2} \frac{\partial \mathbf{J}_T}{\partial t}. \quad (2.23)$$

The instability is avoided by expressing \mathbf{J} in a way that uses only present values of particle positions and velocities.

The electric and magnetic fields are computed on the grid using the Fast Fourier transform. For the longitudinal electric field, the charge density is calculated on the grid from quasiparticle positions. The charge density for a simulation plasma is given by

$$\rho(\mathbf{x}) = \sum_j q_{pj} S(\mathbf{x} - \mathbf{x}_j) \quad (2.24)$$

where q_{pj} is the charge of the j th quasiparticle. The summation is over all the particles in the simulation. The continuous function $\rho(\mathbf{x})$ is sampled at the grid to form a discrete set of values. There are many sampling methods that interpolate particle information to the grid. The method implemented in our simulation codes is the subtracted-dipole scheme (SUDS). Let the charge density of the particles be Taylor-expanded around the grid point nearest them. Truncation of the Taylor series to the first order terms yields

$$\rho(\mathbf{x}) \simeq \sum_g \sum_{j \in g} q_{pj} \{ S(\mathbf{x} - \mathbf{x}_g) + (\mathbf{x}_j - \mathbf{x}_g) \cdot \nabla_g S(\mathbf{x} - \mathbf{x}_g) \} \quad (2.25)$$

where the outside summation is over all the grid points and where the notation $j \in g$ refers to the particles nearest \mathbf{x}_g . The spatial derivatives in Eq. (2.25) are approximated by a centered differencing over adjacent grid cells. The number of computations and the storage space are thereby reduced compared to full evaluation of the dipole terms. The explicit steps in one dimension will be followed here. The extension to a higher number of dimensions is straightforward. In one dimension, Eq. (2.25) after differencing is

$$\rho(x) = \frac{en_0 L_x}{N_0} \sum_g \sum_{i \in g} \frac{q}{e} \left\{ S(x - x_g) + \frac{(x_i - x_g)}{2\Delta} [S(x - x_{g+1}) - S(x - x_{g-1})] \right\}.$$

Switching indices yields

$$\rho(x) = \frac{en_0 L_x}{N_0} \sum_g S(x - x_g) \left\{ \sum_{j \in g} \frac{q_j}{e} + \sum_{j \in g-1} \frac{q_j}{e} \frac{(x_i - x_{g-1})}{2\Delta} - \sum_{j \in g+1} \frac{q_j}{e} \frac{(x_i - x_{g+1})}{2\Delta} \right\}. \quad (2.26)$$

The quantity in the curly brackets is a measure of the number of charge weighted simulation particles in the vicinity of grid points. This number is a dimensionless charge density function which will be denoted by the variable G as follows.

$$\rho(x) = \frac{en_0}{N_0} L_x \sum_g S(x - x_g) G(x_g). \quad (2.27)$$

Generalization to higher dimensions yields

$$\rho(\mathbf{x}) = \frac{en_0}{N_0} V \sum_g S(\mathbf{x} - \mathbf{x}_g) G(\mathbf{x}_g). \quad (2.28)$$

The charge density in Eq. (2.28) is expressed as a sum of values on a grid rather than as a sum over individual particles.

The form of the charge density in Eq. (2.28) is convenient for the FFT. The Fourier transform and its inverse given by Eqs. (2.11) and (2.12) require modification since ρ is only known at regular spaced intervals. It becomes necessary to use the discrete form of Eq. (2.12) to ascertain the inverse Fourier transform. In one dimension, the discrete inverse Fourier transform is given by

$$\rho(k_m) = \frac{1}{N_g} \sum_{g=1}^{N_g} f(x_g) e^{-ik_m x_g} \quad (2.29)$$

where N_g is the number of grid points. Furthermore, with a spatial grid, wavelengths smaller than twice the spacing between adjacent grid points, Δ ,

can no longer be resolved. In analogy with digital time series, the wavenumber associated with this wavelength will be called the Nyquist wavenumber. The discrete Fourier transform truncates the sum in Eq. (2.11) to wavenumbers smaller than the Nyquist wavenumber. For a one dimensional system, the discrete Fourier transform is

$$\rho(x_g) = \sum_{m=-\frac{N_g}{2}+1}^{\frac{N_g}{2}-1} \rho(k_m) e^{ik_m x_g}. \quad (2.30)$$

Again it is straightforward to generalize Eqs. (2.29) and (2.30) to include more spatial dimensions.

The presence of a spatial grid modifies the physical properties of a simulation plasma. The imposition of a spatial grid leads to information loss. As was shown in the preceding paragraph, any structure in the simulation whose wavenumber is larger than the Nyquist wavenumber is no longer resolved. This information loss manifests itself as the coupling of an oscillation with principal harmonic k to oscillations that differ by an integer number times the grid wavenumber, $k_g = \frac{2\pi}{\Delta}$, from the principal harmonic. This spurious coupling is called aliasing. Fortunately, the significance of this coupling can be reduced if the quasiparticle size and the Debye length are not much smaller than the grid spacing.

Once the charge density is accumulated on the grid, it is Fourier transformed to \mathbf{k} -space. The Fourier transform of Eq. (2.20), Poisson's law, becomes

$$i\mathbf{k} \cdot \mathbf{E}_L(\mathbf{k}) = 4\pi\rho(\mathbf{k}).$$

The equation for the longitudinal electric field is given by

$$\mathbf{E}_L(\mathbf{k}) = -i4\pi en_0 N_g \frac{V}{N_0} \frac{\mathbf{k}}{k^2} S(\mathbf{k}) G(\mathbf{k}) \quad (2.31)$$

where we have used the Fourier transform of Eq. (2.28) to express \mathbf{E}_L in terms of G .

The simulation does not calculate the electric field but rather the electric force. Let \mathbf{F}_L and \mathbf{F}_T be defined as

$$\mathbf{F}_L(\mathbf{k}) = VS(-\mathbf{k})\mathbf{E}_L(\mathbf{k}) \quad (2.32a)$$

$$\mathbf{F}_T(\mathbf{k}) = VS(-\mathbf{k})\mathbf{E}_T(\mathbf{k}) \quad (2.32b)$$

with

$$\mathbf{F}_E(\mathbf{k}) = \mathbf{F}_L(\mathbf{k}) + \mathbf{F}_T(\mathbf{k}). \quad (2.32c)$$

Poisson's law for the longitudinal electric force is easily seen to be

$$\mathbf{F}_L(\mathbf{k}) = -i \frac{m}{e} \omega_{pe}^2 N_g \frac{V^2}{N_0} \frac{\mathbf{k}}{k^2} |S(\mathbf{k})|^2 G(\mathbf{k}). \quad (2.33)$$

The inverse transform of Eq. (2.33) yields values of \mathbf{F}_L that are defined only at the grid points. The SUDS interpolation scheme is used to calculate the force at the particle position. To illustrate this, let us Taylor-expand the force felt by a particle about the nearest grid point such that

$$F(\mathbf{x}_i) = \mathbf{F}(\mathbf{x}_g) + (\mathbf{x}_i - \mathbf{x}_g) \cdot \nabla_g \mathbf{F}(\mathbf{x}_g).$$

The gradient is finite-differenced about the grid points adjacent to the nearest grid point and is interpolated in the manner outlined for the charge density.

It is straightforward to solve Ampere's law for the magnetic field using the FFT. Remembering Ampere's law in the Darwin model is

$$\nabla \times \mathbf{B}(\mathbf{x}) = \frac{4\pi}{c} \mathbf{J}_T(\mathbf{x})$$

where

$$\mathbf{J}(\mathbf{x}) = \sum_j q_{pj} S(\mathbf{x} - \mathbf{x}_j).$$

The accumulation of the current density proceeds in the same way as the accumulation of the charge density. The equation for the current density expressed in terms of grid values is given by

$$\mathbf{J}(\mathbf{x}) = en_0 \frac{V}{N_0} \sum_g S(\mathbf{x} - \mathbf{x}_g) \mathbf{U}(\mathbf{x}_g). \quad (2.34)$$

The replacement of $q_j e$ by $q_j e \mathbf{v}_j$ on the right-hand side of Eq. (2.26) shows how the particle velocities are interpolated with \mathbf{U} representing the sum in the curly brackets. The variable \mathbf{U} in Eq. (2.34) is a measure of the charge weighted velocity of the quasiparticles in the vicinity of the grid points. The Fourier transform of Ampere's law yields

$$i\mathbf{k} \times \mathbf{B}(\mathbf{k}) = \frac{4\pi}{c} \mathbf{J}_T(\mathbf{k}). \quad (2.35)$$

Taking the cross product of \mathbf{k} with Eq. (2.35) and using Eq. (2.21), Ampere's law becomes

$$\mathbf{B}(\mathbf{k}) = i \frac{4\pi}{c} \frac{\mathbf{k} \times \mathbf{J}(\mathbf{k})}{k^2}. \quad (2.36)$$

The magnetic force, \mathbf{F}_B , is the quantity actually used to accelerate the quasiparticles. From Eqs. (2.14), (2.34), and (2.36), the expression that the code solves for the magnetic force is given by

$$\mathbf{F}_B(\mathbf{k}) = i \frac{m \omega_{pe}^2}{e c} \frac{N_g}{N_0} V^2 |S(\mathbf{k})|^2 \frac{\mathbf{k} \times \mathbf{U}(\mathbf{k})}{k^2}. \quad (2.37)$$

After the current density is accumulated of the grid, it is Fourier-transformed to k -space. The magnetic force is computed in k -space by Eq. (2.37) and is subsequently inverse Fourier transformed to configuration space for ion acceleration.

Solving for the transverse electric fields proves to be more arduous than solving for the magnetic field and for the longitudinal electric

field. The method of solution developed here parallels the techniques reported by Busnardo-Neto⁴⁸ et al. Changing the model to guiding center motion adds complexity to their approach. Another valuable reference by Nielson and Lewis⁴⁹ presents a broader discussion of plasma simulation codes incorporating the Darwin model.

Let us first examine the solution to equation for the transverse electric field using a Vlasov description of the plasma. This approach will lend some insight to the physical nature of the terms later encountered when a plasma of finite size particles is considered. The time derivative of the current density is given by

$$\frac{\partial \mathbf{J}}{\partial t} = \frac{\partial \mathbf{J}_i}{\partial t} + \frac{\partial \mathbf{J}_e}{\partial t} = e \int \mathbf{v} \left[\frac{\partial f_i}{\partial t} - \frac{\partial f_e}{\partial t} \right] d\mathbf{v} \quad (2.38)$$

for a hydrogen-like plasma. The integral in the equation can be evaluated following steps analogous to those used in the derivation of the momentum transfer equation. The Vlasov equation is used for the evaluation of partial time derivative of the ion distribution function

$$\frac{\partial f}{\partial t} = -\mathbf{v} \cdot \nabla f_i - \frac{e}{m} \left(\mathbf{E} + \frac{\mathbf{v}}{c} \times \mathbf{B} \right) \cdot \nabla_v f_i. \quad (2.39)$$

The corresponding kinetic equation for the electron response, the drift-kinetic equation, is given as

$$\frac{\partial f_e}{\partial t} = - \left(v_{\parallel} \nabla_{\parallel} f_e + \frac{c\mathbf{E}}{B_0} \times \hat{b} \cdot \nabla f_e \right) + \frac{e}{m} \mathbf{E}_{\parallel} \cdot \nabla_v f_e. \quad (2.40)$$

If Eq. (2.30) is subtracted from Eq. (2.29), then multiply by \mathbf{v} and integrate over all velocity space we obtain for \mathbf{J}

$$\frac{\partial \mathbf{J}(\mathbf{x})}{\partial t} = -\nabla \cdot \mathcal{R}(\mathbf{x}) + \frac{e^2}{m} n_e(\mathbf{x}) \mathbf{E}_{\parallel}(\mathbf{x}) + \frac{e^2}{M} n_i(\mathbf{x}) \mathbf{E}(\mathbf{x}) + \frac{e}{Mc} \mathbf{J}_i(\mathbf{x}) \times \mathbf{B}(\mathbf{x}) \quad (2.41)$$

where

$$\mathcal{R}(\mathbf{x}) = en_0[\langle \mathbf{v}\mathbf{v} \rangle_i(\mathbf{x}) - \langle \mathbf{v}\mathbf{v} \rangle_e(\mathbf{x})]$$

where

$$\langle \mathbf{v}\mathbf{v} \rangle = \int \mathbf{v}\mathbf{v}f(\mathbf{x})d\mathbf{x}.$$

The equation for the transverse electric field can then be expressed by

$$c^2 \nabla^2 \mathbf{E}_T - [\omega_{pe}^2 \mathbf{E}_{\parallel}(\mathbf{x}) + \omega_{pi}^2 \mathbf{E}(\mathbf{x})]_T = 4\pi [\mathbf{J}_i \times \boldsymbol{\Omega}_i(\mathbf{x}) - \nabla \cdot \mathcal{R}(\mathbf{x})]_T \quad (2.42)$$

where

$$\boldsymbol{\Omega}_i = \frac{e\mathbf{B}}{Mc}.$$

The second term on the left side of Eq. (2.42) is the divergence of the current transfer tensor. The first term on the right side represents an ion flux crossed with the magnetic field. The second term on the left side of Eq. (2.42) accounts for the bulk electron acceleration along the magnetic field lines and the third term accounts for the bulk ion electric acceleration.

If an external current is allowed, the transverse electric field is calculated from

$$\nabla^2 \mathbf{E}_T = \frac{4\pi}{c^2} \left[\frac{\partial \mathbf{J}_p}{\partial t} + \frac{\partial \mathbf{J}_{\text{ext}}}{\partial t} \right]_T \quad (2.43)$$

where \mathbf{J}_p is the contribution from the plasma particles and where \mathbf{J}_{ext} is the contribution from some external source such as an antenna. The plasma contribution is given by

$$\frac{\partial \mathbf{J}_p}{\partial t} = \sum_j q_{pj} \left[\frac{d\mathbf{v}_j}{dt} S(\mathbf{x} - \mathbf{x}_j) - \mathbf{v}_j \mathbf{v}_j \cdot \nabla S(\mathbf{x} - \mathbf{x}_j) \right]. \quad (2.44)$$

The full time derivative is applied to the particle because the time derivative is evaluated in the particle's frame of reference. The second term on the right side of Eq. (2.44) is a convective derivative over the current density of the particle.

The difficulty in obtaining the transverse electric field is apparent from the particle acceleration term of Eq. (2.44). The acceleration contains the very same transverse electric field that is being solved for. Using the particle equations of motion for the acceleration, the plasma contribution to the time derivative of the current becomes

$$\begin{aligned}
\frac{\partial \mathbf{J}_p}{\partial t} = & q_p \frac{e}{M} \sum_j^{\text{ions}} S(\mathbf{x} - \mathbf{x}_j) \int \\
& \times \left[\mathbf{E}(\mathbf{x}') + \frac{\mathbf{v}_j}{c} \times \mathbf{B}(\mathbf{x}') \right] S(\mathbf{x}' - \mathbf{x}_j) d\mathbf{x}' \\
& + q_p \frac{e}{m} \sum_j^{\text{electrons}} S(\mathbf{x} - \mathbf{x}_j) \int \left\{ \hat{\mathbf{b}}(\mathbf{x}') \left[\hat{\mathbf{b}}(\mathbf{x}') \cdot \mathbf{E}(\mathbf{x}') \right] \right\} \\
& S(\mathbf{x}' - \mathbf{x}) d\mathbf{x}' - \nabla \cdot \sum_j^{\text{all particles}} q_{pj} \mathbf{v}_j \mathbf{v}_j S(\mathbf{x} - \mathbf{x}_j). \tag{2.45}
\end{aligned}$$

The first summation on the right side of Eq. (2.45) includes the ion acceleration. The second summation includes the parallel electron acceleration. The last summation expresses a convective derivative concerned with the flux of the current density of the particles into or from the neighborhood of \mathbf{x} .

An important difference between this expression of $\dot{\mathbf{J}}$ from the previous cases⁴⁸ is the absence of an electron acceleration term perpendicular to the magnetic field. The averaging of the electron Larmor acceleration results in a zero net force on the electron guiding center. The acceleration of the perpendicular electric field results in the instantaneous motion of the electron guiding center due to the $\mathbf{E} \times \mathbf{B}$ drift. Thus the perpendicular acceleration of the electron guiding center responds to is from the temporal change of the electric field. This is the acceleration that produces the polarization drift. This acceleration is one order smaller in the expansion parameter ω/Ω_e than what is otherwise retained in the model. A preliminary attempt to include the $\dot{\mathbf{E}} \times \mathbf{B}$ acceleration was unstable, therefore this

term is not included.

The combination of Eqs. (2.43) and (2.45) forms an integro-differential equation for the transverse electric field. The equation in this form is difficult to exactly solve. The equation assumes a more tractable form if all of the variables are Fourier transformed. In particular, the equation is simplified if the equations for the transverse electric force is solved rather than the transverse electric field. The integrals over the acceleration terms develop into a dependence of basic variables of wavenumber \mathbf{k} on summations involving a second wave number \mathbf{k}' . The summations contain the transverse electric force, resulting in a matrix with as many levels as there are \mathbf{k} -modes. Rather than the computational costly direct inversion of the matrix, a renormalization method is used which iteratively solves for the transverse electric field. We believe that this approach is more satisfactory than the Born approximation for the transverse electric force. The steps followed in ascertaining the transverse electric force are detailed in Appendix A. The transformed equation for the transverse electric force is given by Eq. (A14)

$$\begin{aligned}
& \frac{k^2 c^2}{V^2 |S(k)|^2} \frac{N_0}{N_g} \mathbf{F}_T(\mathbf{k}) + \omega_{pi}^2 \left[\sum_{\mathbf{k}'} n_i(\mathbf{k}') \mathbf{F}_E(\mathbf{k} - \mathbf{k}') \right]_T \\
& + \omega_{pe}^2 \left[\sum_{\mathbf{k}'} n_e(\mathbf{k}') \mathbf{F}_{\parallel}(\mathbf{k} - \mathbf{k}') \right]_T \\
& = \left\{ \frac{m}{e} \omega_{pe}^2 i \mathbf{k} \cdot \mathcal{IP}(\mathbf{k}) - \omega_{pi}^2 \sum_{\mathbf{k}'} \frac{\mathbf{U}_i(\mathbf{k}')}{c} \right. \\
& \left. \times \mathbf{F}_B(\mathbf{k} - \mathbf{k}') - \frac{4\pi}{VS(\mathbf{k})} \frac{N_0}{N_g} \frac{\partial}{\partial t} \mathbf{J}_{\text{ext}}(\mathbf{k}) \right\}_T \quad (\text{A14})
\end{aligned}$$

where n_e and n_i are the electron and ion number densities, \mathcal{IP} is the tensor formed by accumulating the charge weighted velocity products $\mathbf{v}\mathbf{v}$ of the particles on the grid, and \mathbf{U}_i is the grid weighted ion velocity. The necessary

particle information is accumulated using the same SUDS scheme described earlier. A ready identification can be made between corresponding terms of Eqs. (A14) and (2.42).

The simplification inherent in the renormalization method also has its drawbacks. The renormalization method assumes that the $\mathbf{k}' \neq 0$ elements of the summations on the left side of Eq. (A14) are small compared to the $\mathbf{k}' = 0$ terms. There are three physical quantities besides the electric force included in the summations. They are the ion and electron number densities and the magnetic field direction unit vector. The iterative procedure used to solve Eq. (A14) implies that the size of the deviations of n_e , n_i , and \mathbf{b} are much smaller than their average ($\mathbf{k}' = 0$) values. Busnardo-Neto et al.⁴⁸ reported that this procedure broke down when the maximum density exceeded twice the background density. In addition to the density restriction, the change in the magnetic field direction is similarly limited. However, the magnitude of the magnetic field can change considerably without affecting the iterative procedure as long as its direction vector remains relatively constant. Requiring that the electron ∇B drift remain much smaller than the $\mathbf{E} \times \mathbf{B}$ drift limits the magnitude of the change in the magnetic field. The iterative method of solution for the transverse electric force works best when the density is loaded uniformly and when the angles between various components of the background magnetic field remain constant.

2.4 Time Advancement

The time dependence expressly appears in the equations of particle motion. A stable and accurate method of time differencing must be devised for the successful application of the model. This task is complicated by the differing structures of the equations governing the electron parallel

motion and ion motion versus the electron perpendicular motion. Simplified models for each of the two sets of equations will be given and the techniques of time differencing each set will be presented. This approach is expected to delineate the essential elements of the numerical scheme more clearly than a complete discussion with all of the details. A flow chart is presented at the end of this chapter that explains the full algorithm.

At time $t=0$, the program begins with the definition of some appropriate initial conditions for the particle velocities and positions. The background magnetic fields are assigned their prescribed values. The electric and magnetic fields derived from the plasma are initially set to zero. The particle positions are then advanced forward one-half time step by finite differencing Eqs. (2.6) and (2.8) as follows

$$x_j^{1/2} = x_j^0 + v_j^0 \frac{\Delta t}{2}$$

where the superscripts denote the time level. The time levels have either an integer or half integer value of the time step. The time t^n is given by

$$t^n = n\Delta t$$

where Δt is the time step. With the initialization complete, the computational cycle begins and usually repeats itself hundreds or thousands of time as the phenomena of interest unfold.

The coupled field-particle equations for the ion motion and parallel electron motion are comparable to the following set of differential equations

$$\frac{dv}{dt} = f(x) + g(x, v). \quad (2.46a)$$

$$\frac{dx}{dt} = v \quad (2.46b)$$

The function f is identified with the longitudinal electric fields and the function g is identified with the magnetic and transverse electric fields. The finite differencing scheme implemented in the program is

$$\begin{aligned}
 x^n &= x^{n-1/2} + \frac{v^n \Delta t}{2} \\
 g^n &= g(x^n, v^n) \\
 x^{n+1/2} &= x^n + v^n \frac{\Delta t}{2} \\
 f^{n+1/2} &= f(x^{n+1/2}) \\
 \bar{g}^{n+1/2} &= 3/2 g^n - 1/2 g^{n-1} \\
 v^{n+1} &= v^n + \Delta t (f^{n+1/2} + \bar{g}^{n+1/2}).
 \end{aligned}$$

This time differencing technique is a variant of the leap-frog method. The leap-frog method is normally applied to a second-order hyperbolic differential equation in which the right side is only a function of x , e.g., the function g is missing. The primary difference we have introduced is the linear extrapolation one-half time step forward of the function g . The leap-frog scheme is a simple yet stable method if the time step is sufficiently small. The time-centered nature of this scheme is the key to its stability because the errors introduced by the time differencing are not numerically systematic. The function g is extrapolated forward to recover time centering. The function g can be evaluated only at integral time steps because of its dependence on the velocity. The function f is evaluated at half-integral time steps and is already time-centered for the velocity update.

The extrapolation of g is not expected to introduce serious problems for the algorithm. For parameter ranges of concern, the magnitudes of the longitudinal electric fields from charge separation are much larger than the corresponding current-induced transverse electric fields. Similarly, the plasma contribution to the magnetic field is small compared with background

magnetic field. Thus the dominant components of the electric and magnetic fields are time-centered. This extrapolation is expected to be sufficiently accurate for our purposes. If the magnetic fields and transverse electric fields are driven larger than their equilibrium values by the sinusoidal variation of an external driver, then the extrapolation should provide a good estimate if the period of the exciter is much larger than the time step.

The field-particle equations for the electron motion are in the form of the differential equations

$$v = f(x) + g(x, v) \quad (2.47a)$$

$$\frac{dx}{dt} = v. \quad (2.47b)$$

Again f is associated with the longitudinal electric field and g is associated with the transverse electric field. This pair of equations is more difficult to finite difference in a time-centered way than Eq. (2.46). If the function g is absent, the predictor-corrector scheme shown below provides a virtual time-centered method of advancing the equations forward in time:

$$\begin{aligned} x^{n+1/2} &= x^{n-1/2} + v^n \Delta t \\ f^{n+1/2} &= f(x^{n+1/2}) \\ x_{\text{pred}}^{n+3/2} &= x^{n-1/2} + 2\Delta t f^{n+1/2} \\ f_{\text{pred}}^{n+3/2} &= f(x_{\text{pred}}^{n+3/2}) \\ v^{n+1} &= \frac{f_{\text{pred}}^{n+3/2} + f^{n+1/2}}{2} \end{aligned}$$

This scheme was successfully applied by Lee and Okuda⁴¹ to a purely electrostatic system. Introduction of the function g again leads to an extrapolation of g to preserve virtual time-centering. The method we have chosen is a

modified version of the predictor-corrector scheme shown below

$$\begin{aligned}
 x^n &= x^{n-1/2} + \frac{v^n \Delta t}{2} \\
 g^n &= g(x^n, v^n) \\
 x^{n+1/2} &= x^n + \frac{v^n \Delta t}{2} \\
 f^{n+1/2} &= f(x^{n+1/2}) \\
 \bar{g}^{n+1/2} &= 3/2 g^n - 1/2 g^{n-1} \\
 x_{\text{pred}}^{n+3/2} &= x^{n-1/2} + 2\Delta t(f^{n+1/2} + \bar{g}^{n+1/2}) \\
 f_{\text{pred}}^{n+3/2} &= f(x_{\text{pred}}^{n+3/2}) \\
 \bar{g}^{n+1} &= 2g^n - g^{n-1} \\
 v_{\text{pred}}^{n+1} &= \bar{g}^{n+1} + \frac{f_{\text{pred}}^{n+3/2} + f^{n+1/2}}{2} \\
 x_{\text{pred}}^{n+1} &= x^{n+1/2} + v_{\text{pred}}^{n+1} \frac{\Delta t}{2} \\
 g_{\text{pred}}^{n+1} &= g(v_{\text{pred}}^{n+1}, x_{\text{pred}}^{n+1}) \\
 v^{n+1} &= g_{\text{pred}}^{n+1} + \frac{f_{\text{pred}}^{n+3/2} + f^{n+1/2}}{2}.
 \end{aligned}$$

Present information at the $n-1$, n , and $n+1/2$ time levels is used to predict future values of the particle velocities and positions. Predicted values of the electric and magnetic fields can be obtained from the predicted particle velocities and positions. These predicted fields can then be used to advance the electron velocity in a virtual time-centered way.

2.5 Boundary Conditions

It is easiest to mathematically model an infinite, homogeneous plasma. However, all plasmas that physically exist are inhomogeneous and have boundaries that limit their extent. There are many problems where it is important to model inhomogeneous plasmas. Particle simulation codes that utilize the Fourier transform are naturally suited for periodic systems. FFT techniques are efficient at solving the field equations and are particularly convenient for the iterative transverse electric field solver.

One straightforward way of including an inhomogeneity in a periodic system is to require that all quantities become symmetric with respect to the center of the model. Let us consider the x -direction inhomogeneous and define $L_x/2$ as the center of the system. The condition for periodicity requires that any quantity ψ satisfy either

$$\psi(x) = \psi(L_x - x) \quad (2.48a)$$

or

$$\psi(x) = -\psi(L_x - x) \quad (2.48b)$$

for $0 \leq x \leq L_x/2$. Functions that satisfy Eq. (2.48a) are termed even and functions that satisfy Eq. (2.48b) are termed odd. This idea is implemented in the x -direction of the simulation. It is clear from the symmetry conditions that the system is completely specified from information from only half of the system. We take advantage of this to follow particles in only half of the system, called the active system. The other half we denote as the image system. Our simulation model is bounded in the x -direction in the sense described above. The y -direction is periodic. Boundaries are placed at $x=0$ and $x = L_x/2$ that particles are not allowed to cross. Functions such as the background magnetic field or density can vary in the region $0 \leq x \leq L_x/2$

as long as the active system plus the image system remain periodic. In the y -direction, variation is continuous such that for a function ψ ,

$$\psi(y) = \psi(L_y + y).$$

Figure 2.1 shows a picture of the computational system.

For each particle in the active system, a corresponding image particle is presumed to exist. The image particle is defined to be at the same distance from the centerline of the system as the active particle. The motion of the image particle mirrors the motion of the corresponding active particle with respect to the center of the system. As the active particle approaches or moves away from the system centerline, the image particle moves in the same manner. Both the image and active particle execute the same motion in the plane parallel to the boundary.

This boundary technique has one degree of freedom, the sign of the image charge. If an image particle has the opposite charge of its complementary active particle, the electric fields tangent to the boundary are odd functions and thus must be zero at $x=0$ and $x = L_x/2$. This choice physically resembles a plasma bounded by conducting walls. If both the image and active particles have the same charge, the electric field normal to the boundary is an odd function and is zero at the boundaries.

When a boundary is introduced into a simulation plasma, the way in which the particles interact with the boundary deserves special attention. Boundary conditions should be devised that do not disturb the phenomena of interest in the plasma interior. Naitou et al.,^{50,51} have studied in detail the sources of non-physical boundary effects caused by reflecting particles. In our codes, particles that cross a boundary in the y -direction are simply reinserted at the other end. Particles that cross the x -boundary are reflected back into the active system.

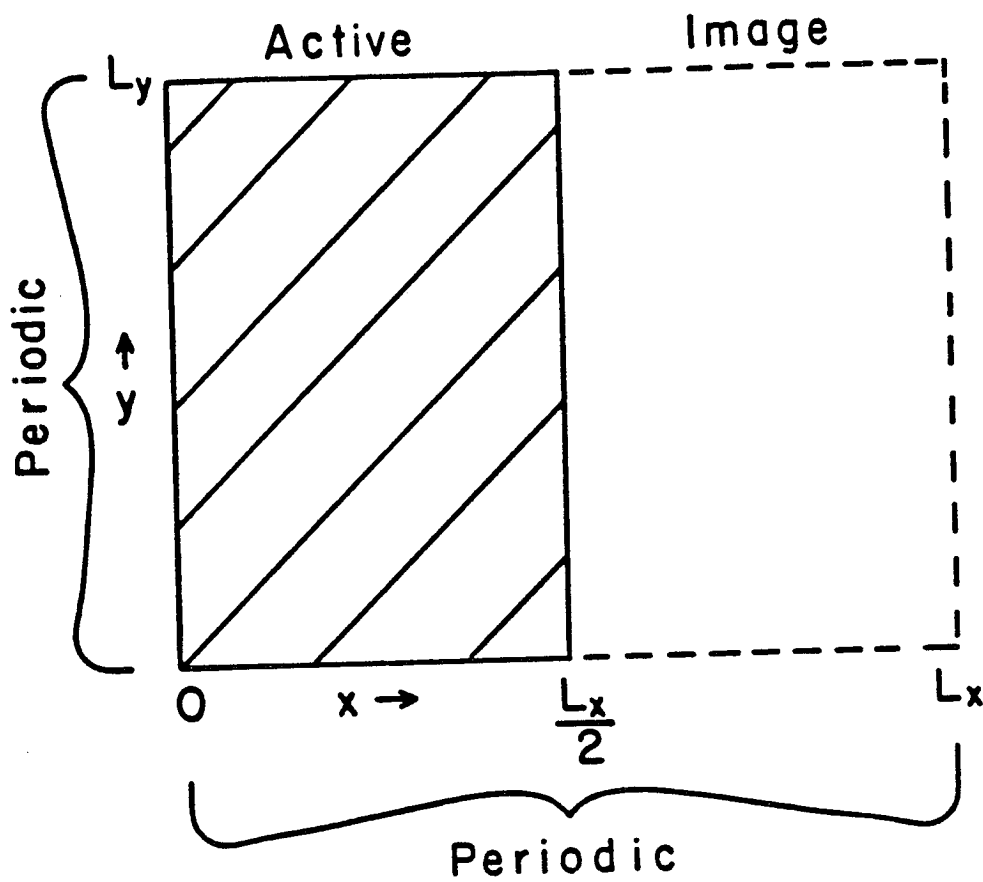


Figure 2.1. Depiction of the bounded simulation model. Particles are moved in the left (active) half of the system shaded above.

The particle reflection scheme implemented in the code is adapted from a method (Method I) suggested by Naitou⁵¹ et al. When an electron crosses an x -boundary, it is reflected back into the active system subject to the following conditions:

$$\begin{aligned}
v_x(\text{new}) &= -v_x(\text{old}) \\
v_y(\text{new}) &= v_y(\text{old}) \\
v_z(\text{new}) &= v_z(\text{old}) \\
x(\text{new}) &= 2x_B - x(\text{old}) \\
y(\text{new}) &= y(\text{old})
\end{aligned} \tag{2.49}$$

where x_B is the x -coordinate of the particle reflection. The electrons respond as if they had an elastic collision with the boundary. The ion reflection conditions are

$$\begin{aligned}
v_x(\text{new}) &= -v_x(\text{old}) \\
v_y(\text{new}) &= -v_y(\text{old}) \cos 2\theta + v_z(\text{old}) \sin 2\theta \\
v_z(\text{new}) &= v_y(\text{old}) \sin 2\theta + v_z(\text{old}) \cos 2\theta \\
x(\text{new}) &= 2x_B - x(\text{old}) \\
y(\text{new}) &= y(\text{old}) + [x_B - x(\text{old})] \frac{v_y(\text{new}) - v_y(\text{old})}{v_x(\text{old})}
\end{aligned} \tag{2.50}$$

where θ is the angle between \mathbf{B}_0 and the z -direction. This reflection scheme conserves particle energy. It is designed to minimize sheath currents at the boundary that can occur from shifts between the electron and ion guiding centers.

This section concludes with a discussion of a computational features not previously mentioned. The implementation of these features increases the operational efficiency of the simulation. Since the model is

$2\frac{1}{2} D$, the spatial mesh extends in the x - and y -directions. Typically, the spacings between adjacent grid points in the x -direction, Δ_x , and the y -direction, Δ_y , are the same. For heating applications, we have found it advantageous to increase the y -spacing compared to the x -spacing. The simulations have run successfully for the case of

$$\Delta_y = 10\Delta_x.$$

The antenna wavelength was then increased with respect to L_x enabling improved penetration of the excited wave from the edge into the interior. A second beneficial effect of increasing Δ_y is that the separation between the pump frequency and the ion cyclotron frequency can be increased without diminishing computational efficiency.

The second feature involves the selective filtering of \mathbf{k} -modes to decrease background noise and increase the time step. The $2\frac{1}{2} D$ model has a discrete \mathbf{k} -spectrum whose components are given by

$$k_x(m) = \frac{2\pi m}{L_x} \quad m = 0, 1, 2 \dots \quad (2.51a)$$

$$k_y(n) = \frac{2\pi n}{L_y} \quad n = 0, 1, 2 \dots \quad (2.51b)$$

$$k^2 = k_x^2 + k_y^2. \quad (2.51c)$$

The parallel component of the wavenumber is given by

$$k_{\parallel} = k_y \sin \theta. \quad (2.52)$$

There are two types of filtering implemented in the code. The first type decreases background noise by setting to zero all modes above some k_{\max} . The second type of filtering increases efficiency by decreasing the maximum value of k_{\parallel}/k . This is accomplished by requiring all modes that

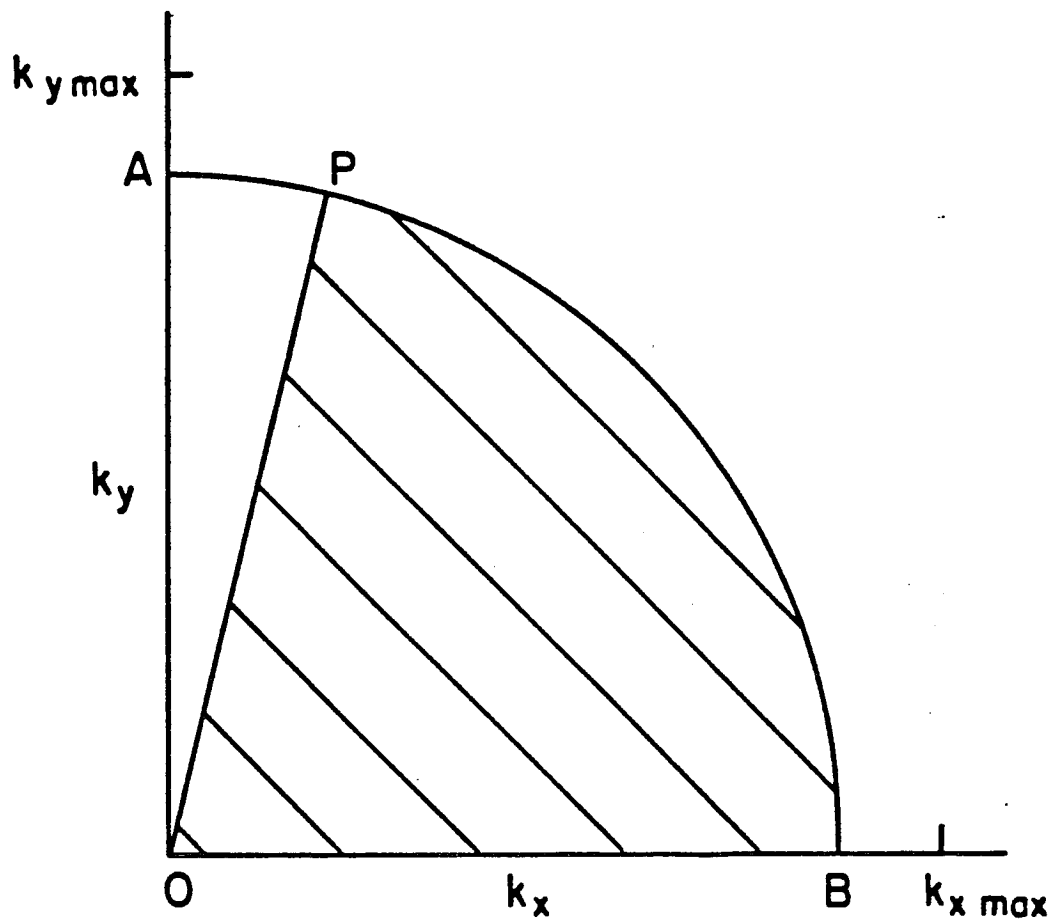


Figure 2.2. Shaded area indicates k -space components that are allowed nonzero values. The wavenumbers $k_{x \max}$ and $k_{y \max}$ are the Nyquist wavenumbers.

lie on or are above a line placed in (m, n) space to have zero energy. Figure 2.2 graphically exhibits the k -space filtering. The shaded area in Fig. 2.2, that is below the quarter circle AB and the line OP , shows which modes in (m, n) space are retained in our model. We have achieved a 50% increase in efficiency when the line OP contains the points $(1, 2)$, $(2, 4)$, $(3, 6)$.

Part B — TESTS OF SIMULATION MODEL

2.6 Dispersion Relations and Normal Mode Analysis

This section investigates the frequency, ω , and wavenumber, k , characteristics of the thermal spectrum for a homogeneous simulation plasma. The plasma, with its original placement of particle positions and velocities, forms an initial value problem where many modes are initially excited. Modes or quasi-modes that dissipate away exchange energy with the multitude of other modes and the thermal motion of the particles, i.e., the heat bath of the system. As a result of this energy exchange and damping, the total system exhibits fluctuations in the spectrum of various modes. The normal modes of oscillation exhibit the largest fluctuation levels. These normal modes are delineated by zeroes of the dispersion function, for which the eigenfrequency is almost purely real with only a small negative imaginary part. Thus, the fluctuations of normal modes dissipate slowly compared to the other modes of the system. The comparison between the frequency characteristics of the fluctuation spectra produced by the simulation plasma with the predictions from linear homogeneous dispersion relations is an important test of the reactive characteristics of the numerical model. Results from a doubly-periodic system and from a singly periodic system, bounded in the x -direction are presented along with theoretical expectations. The remainder of this section discusses the diagnostic methods, the dispersion relations for this model and presents the simulation results on the dispersion relations.

The normal modes of oscillation in the simulation may be determined by examination of the power spectral density functions of the electric and magnetic fields. When a field component, E , is a zero-mean stationary process, the power spectral density, $P_k(\omega)$, of $E_k(t)$ is defined by the

Fourier transform of the autocovariance function $C_{\mathbf{k}}(\tau)$ such that⁵²

$$P_{\mathbf{k}}(\omega) = \int_{-\infty}^{\infty} e^{-i\omega\tau} C_{\mathbf{k}}(\tau) d\tau, \quad (2.47)$$

where the autocovariance function is given by

$$\lim_{T \rightarrow \infty} \left\{ \frac{1}{2T} \int_{-T}^T E_{\mathbf{k}}(t) E_{\mathbf{k}}^*(t + \tau) dt \right\}$$

and where τ is the time lag. The spatial Fourier modes of the electric and magnetic fields are written to an external file over the length of the run.

The autocovariance function cannot be computed for a time lag greater than the length of the run. Since the data is only available at discrete times, the autocovariance function for E is calculated by the formula⁵³

$$C_{\mathbf{k}}(r\Delta t) = \frac{1}{N-r} \sum_{n=1}^{N-r} E_{\mathbf{k}}[n\Delta t] E_{\mathbf{k}}^*[(n+r)\Delta t], \quad r = 0, 1, \dots, m$$

where $r\Delta t$ is the lag time, $m\Delta t$ is the maximum lag time, and N is the number of data points. The autocovariance function is calculated using the FFT such that N is chosen to be power of 2, $N = 2^k$. The maximum lag time was constrained to $\tau \leq 0.3N\Delta t$ to reduce statistical errors in the estimate of $C_{\mathbf{k}}(\tau)$.

The discretized form of Eq. (2.47) can be improved for the estimate of the power spectral density. A windowing function is introduced to filter out spurious high frequency components that are introduced by the finite sample size. In our case, the autocovariance function is multiplied by the Parzen lag weighting function⁵⁴

$$W(r\Delta t) = \begin{cases} 1 - 6(r/m)^2 + 6(r/m)^3 & r = 0, 1, \dots, m/2 \\ 2(1 - r/m)^3 & r = m/2 + 1, \dots, m \\ 0 & r > m \end{cases}$$

to obtain a smooth estimate of $P_{\mathbf{k}}(\omega)$. The power spectral density is calculated by

$$P_{\mathbf{k}}(\omega) = \text{FFT}[C_{\mathbf{k}}(r\Delta t)W(r\Delta t)].$$

The power spectral densities are only computed at discrete frequencies $\omega_j = j\Delta\omega$ where $\Delta\omega = 2\pi/m\Delta t$. Statistical errors in the power spectral can be reduced by choosing $m \ll N$. However, reducing the number of data points in the lag, m reduces the spectral resolution $\Delta\omega$. We are generally constrained by the requirement for good spectral resolution along with the reduction of the errors in spectral amplitudes.

To obtain the dispersion relation the electric and magnetic fields are assumed to have the phasor dependence $e^{i(\mathbf{k}\cdot\mathbf{x}-\omega t)}$. The electric field is expressed in terms of the current density when \mathbf{B} is eliminated from Eqs. (2.18), (2.20), and (2.22) to yield

$$(n^2 + 1) \frac{\mathbf{k}(\mathbf{k} \cdot \mathbf{E})}{k^2} - n^2 \mathbf{E} = \frac{-4\pi i}{\omega} \mathbf{J}$$

where $n^2 = k^2 c^2 / \omega^2$. In terms of indicial notation, we have

$$\gamma_{ij} E_j = \frac{-4\pi i}{\omega} J_i \quad (2.48)$$

where

$$\gamma_{ij} = (n^2 + 1) \frac{k_i k_j}{k^2} - n^2 \delta_{ij}$$

and where δ_{ij} is the Kronecker delta function. Using linearized Vlasov theory, the Fourier transformed plasma current of particle species α can be expressed as a linear function of the electric field through the susceptibility tensor χ_{ij}^α ;

$$J_i^\alpha(\omega, \mathbf{k}) = -i\omega \chi_{ij}^\alpha(\omega, \mathbf{k}) E_j(\omega, \mathbf{k}). \quad (2.49)$$

The current densities of all species can be summed and combined with Eq. (2.48) to yield

$$\Lambda_{ij}(\omega, \mathbf{k}) E_j(\omega, \mathbf{k}) = 0 \quad (2.50)$$

where Λ_{ij} is the dispersion tensor defined by

$$\Lambda_{ij} = \gamma_{ij} + 4\pi \chi_{ij}$$

and $\chi_{ij} = \sum_{\alpha} \chi_{ij}^{\alpha}$. The dispersion relation is obtained from setting the determinant of the dispersion tensor to zero

$$\Delta \equiv \det |A_{ij}| = 0. \quad (2.51)$$

The roots of Eq. (2.51) for a given set (ω, \mathbf{k}) determine the normal modes of oscillation.

The elements of the susceptibility tensor can be drawn directly from the particle equations of motion when the plasma is treated like a cold fluid. Without loss of generality, the coordinate axes can be defined such that

$$\mathbf{B}_0 = B_0 \hat{k}$$

$$\mathbf{k} = k_x \hat{i} + k_z \hat{k} = k(\sin \varphi \hat{i} + \cos \varphi \hat{k})$$

where φ is the angle between \mathbf{k} and \mathbf{B}_0 . From Eqs. (2.4) and (2.5), the electron conductivity tensor elements are given by

$$4\pi\chi_{ij}^e = \begin{pmatrix} 0 & \frac{-i\omega_{pi}^2}{\Omega_i \omega} & 0 \\ \frac{i\omega_{pi}^2}{\omega \Omega_i} & 0 & 0 \\ 0 & 0 & -\omega_{pe}^2/\omega^2 \end{pmatrix} \quad (2.52)$$

Using Eq. (2.7), the ion conductivity tensor is given by

$$4\pi\chi_{ij}^i = \begin{pmatrix} \frac{-\omega_{pi}^2}{\omega^2 - \Omega_i^2} & -i \frac{\Omega_i}{\omega} \frac{\omega_{pi}^2}{\omega^2 - \Omega_i^2} & 0 \\ \frac{i\Omega_i}{\omega} \frac{\omega_{pi}^2}{\omega^2 - \Omega_i^2} & \frac{-\omega_{pi}^2}{\omega^2 - \Omega_i^2} & 0 \\ 0 & 0 & -\frac{\omega_{pi}^2}{\omega^2} \end{pmatrix} \quad (2.53)$$

in the cold plasma limit. Finite size particle effects can be included in Eqs. (2.52) and (2.53) by replacing ω_{pi}^2 and ω_{pe}^2 by $\omega_{pi}^2 e^{-k^2 a^2}$ and $\omega_{pe}^2 e^{-k^2 a^2}$ respectively.

In a thermal plasma, the electric and magnetic fields depend on the particle distribution functions. When the electron motion is represented by the guiding center motion, the electron thermal motion and associated gyromotion cease to exchange energy with waves as effectively as electrons with the ballistic motion. In fact Eq. (2.6) does not involve any kinetic energy in the direction perpendicular to the magnetic field. The electron perpendicular motion is insulated from the whole thermal system in which fluctuations and dissipation of various modes are taking place simultaneously. The linearized drift-kinetic equation,

$$\frac{\partial f_{e1}}{\partial t} + v_{\parallel} \nabla_{\parallel} f_{e1} = \frac{e}{m} \mathbf{E}_{\parallel} \cdot \nabla_v f_{e0},$$

is the appropriate expression for the electron distribution function. Solving for the perturbed distribution function, f_{e1} yields

$$f_{e1} = \frac{ie}{m} \frac{\mathbf{E}_{\parallel} a \cdot \nabla_v f_{e0}}{\omega - k_{\parallel} v_{\parallel}}.$$

The linearized electron current density can be expressed as

$$\begin{aligned} \mathbf{J}^e &= -n_0 e \int_L v_{\parallel} f_{e1} dv_{\parallel} \hat{\mathbf{k}} - \frac{n_0 e c}{B_0^2} \mathbf{E} \times \mathbf{B}_0 \\ \mathbf{J}^e &= \frac{-n_0 e^2}{m} \int_L \frac{v_{\parallel} \frac{\partial f_{e0}}{\partial v_{\parallel}}}{\omega - k_{\parallel} v_{\parallel}} dv_{\parallel} E_{\parallel} \hat{\mathbf{k}} - \frac{n_0 e c}{B_0^2} \mathbf{E} \times \mathbf{B}_0 \end{aligned}$$

where the path of integration is prescribed by the Landau contour. From Eq. (2.54), we see that only the (3,3) element of electron susceptibility tensor differs from the cold plasma case. For a Maxwellian distribution, the integral in Eq. (2.54) can be evaluated to obtain⁵⁵

$$4\pi\chi_{33}^e = \frac{1}{k_{\parallel}^2 \lambda_{De}^2} W \left(\frac{\omega}{k_{\parallel} (T_e/m)^{1/2}} \right) \quad (2.55)$$

where

$$W(x) = 1 - xe^{-x^2/2} \int_0^x e^{y^2/2} dy + \frac{i\pi}{2} xe^{-x^2/2}$$

$$\lambda_{De}^2 = \frac{T_e}{m\omega_{pe}^2}.$$

The full ion Vlasov equation must be used for the perturbed ion distribution function in order to describe our model

$$\begin{aligned} \frac{\partial f_{i1}}{\partial t} + \mathbf{v} \cdot \nabla f_{i1} + \frac{e}{Mc} (\mathbf{v} \times \mathbf{B}_0) \cdot \nabla_v f_{i1} \\ = \frac{-e}{M} (\mathbf{E} + \frac{\mathbf{v}}{c} \times \mathbf{B}_1) \cdot \nabla_v f_{i0} \end{aligned}$$

where \mathbf{B}_1 is the perturbed magnetic field. The integration over velocity space needs to be integrated along the unperturbed trajectory in phase space. This has been done for a Maxwellian distribution function (c.f. Ichimaru⁵⁵) to give

$$4\pi\chi_{ij}^i = -\frac{\omega_{pe}^2}{\omega^2} \left\{ \sum_{n=-\infty}^{\infty} \frac{z_0}{z_n} \pi_{ij}(\beta, z_n, n) \times [1 - W(z_n)] - z_0^2 \delta_{3i} \delta_{3j} \right\} \quad (2.56)$$

where

$$\pi_{ij} = \begin{pmatrix} \frac{n^2}{\beta} \psi_n(\beta) & in\psi'_n(\beta) & \frac{k_{\parallel}}{|k_{\parallel}|} \frac{n}{\sqrt{\beta}} z_n \psi_n(\beta) \\ -in\psi'_n(\beta) & \frac{n^2}{\beta} \psi_n(\beta) - 2\beta\psi'_n(\beta) & \frac{-ik_{\parallel}}{|k_{\parallel}|} \sqrt{\beta} z_n \psi'_n(\beta) \\ \frac{k_{\parallel}}{|k_{\parallel}|} \frac{n}{\sqrt{\beta}} z_n \psi_n(\beta) & \frac{ik_{\parallel}}{|k_{\parallel}|} \sqrt{\beta} z_n \psi'_n(\beta) & z_n^2 n \psi_n(\beta) \end{pmatrix}$$

$$\beta = \frac{k_{\perp}^2 T_i}{M\Omega_i^2}$$

$$z_n = \frac{\omega - n\Omega_i}{|k_{\parallel}| \left(\frac{T_i}{m}\right)^{1/2}}$$

$$\psi_n(\beta) = I_n(\beta) e^{-\beta}$$

where I_n is the modified Bessel function of the 1st kind.

The dispersion relation of a cold, homogeneous plasma for the magnetoinductive model with perpendicular guiding center electron motion is derived from Eqs. (2.50), (2.52), and (2.53) and is given by

$$\tan^2 \phi = \frac{-\left(1 + \frac{\omega_p^2}{\omega^2}\right) \left[\frac{k^2 c^2}{\omega^2} - \frac{\omega_{pi}^2}{\Omega_i(\omega + \Omega_i)}\right] \left[\frac{k^2 c^2}{\omega^2} + \frac{\omega_{pi}^2}{\Omega_i(\omega - \Omega_i)}\right]}{\left(\frac{\omega_p^2 + k^2 c^2}{\omega^2}\right) \left[\left(1 - \frac{\omega_{pi}^2}{\omega^2 - \Omega_i^2}\right) \frac{k^2 c^2}{\omega^2} + \frac{\omega_{pi}^2}{\omega^2 - \Omega_i^2} \left(1 + \frac{\omega_{pi}^2}{\Omega_i^2}\right)\right]} \quad (2.57)$$

where $\omega_p^2 = \omega_{pe}^2 + \omega_{pi}^2$. Gaussian-shaped finite size particle effects are again included in Eq. (2.57) by simply replacing ω_{pi}^2 and ω_{pe}^2 by $\omega_{pi}^2 e^{-k^2 a^2}$ and $\omega_{pe}^2 e^{-k^2 a^2}$. The dispersion relation can be expressed as a cubic polynomial in ω^2 . The roots of this polynomial determine the eigenfrequencies of the normal mode oscillations.

The analysis of these modes simplifies if the wave propagation is either completely parallel or perpendicular to the magnetic field. For purely parallel propagation, $\phi=0$, setting the numerator on the right side of Eq. (2.57) to zero yields the dispersion relation. Three modes are predicted, plasma frequency oscillations, Whistler (or helicon) waves, and shear Alfvén waves. For purely perpendicular propagation, setting the denominator on the right side of Eq. (2.57) gives the dispersion relation. Only the compressional Alfvén-lower hybrid and ion cyclotron waves are predicted in this case. The upper hybrid wave present in a fully electromagnetic model reduces to a constant term here.

For propagation parallel to the magnetic field, the dispersion relation for electrostatic plasma oscillations is

$$\omega^2 = \omega_p^2 e^{-k^2 a^2} + 3 \frac{k^2 T_e}{m}. \quad (2.58)$$

The first order thermal correction and finite size particle effects are included in Eq. (2.58). The spectrum of plasma oscillations has been investigated for a

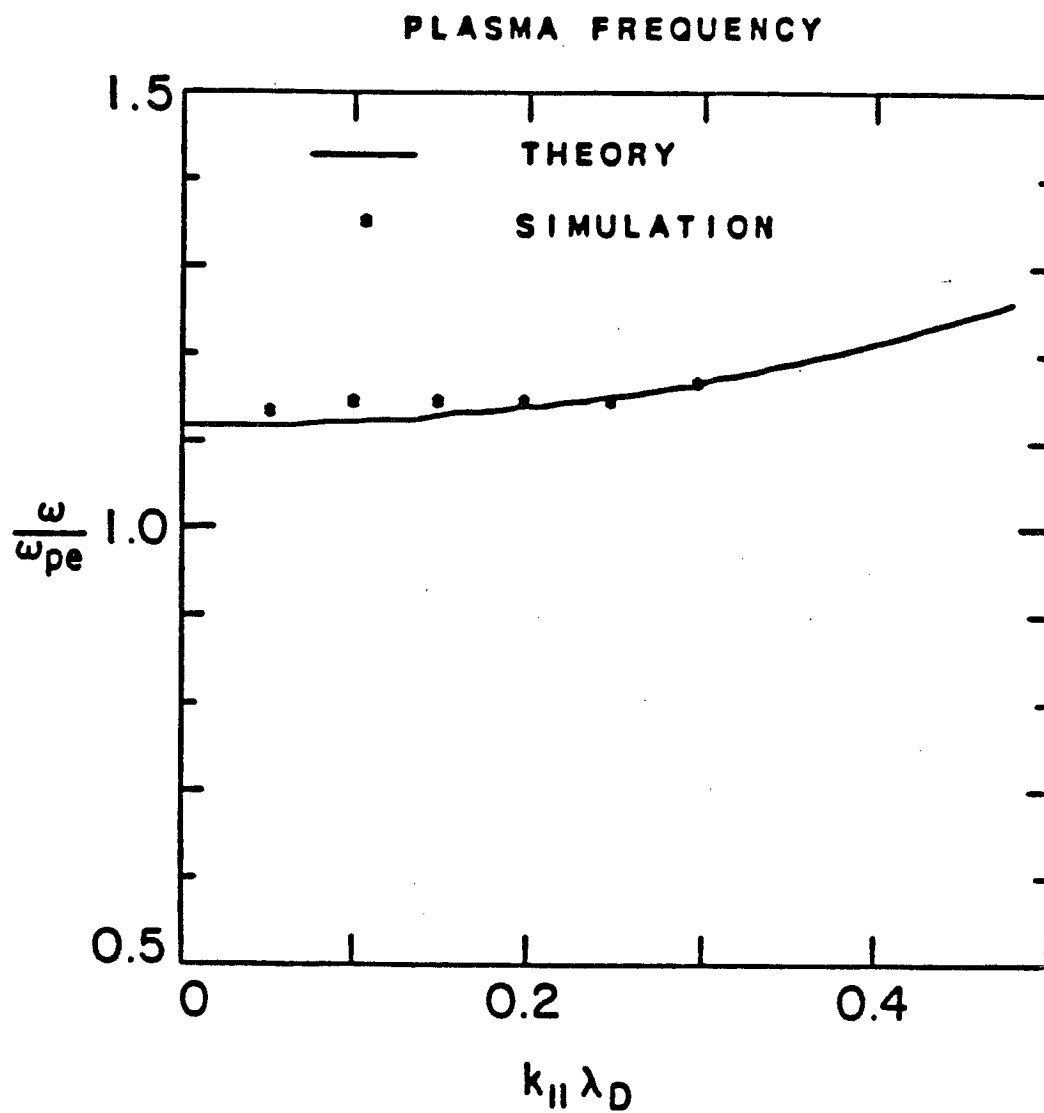


Figure 2.3. Dispersion curves for plasma frequency waves from the $(0, k_y)$ modes.

doubly periodic system in a test run with parameters: $L_x \times L_y = 32\Delta \times 128\Delta$, $a_x = a_y = 1.5\Delta$, $v_T = 1.0\omega_{pe}\Delta$, $M/m = 4.0$, $T_i/T_e = 1.0$, $\Omega_e/\omega_{pe} = 1.2$, and $\theta = 90^\circ$ where $\theta = \tan^{-1}(B_y/B_z)$. The frequency peaks of the power spectra for the plasma frequency branch are plotted versus $k\Delta$ in Fig. 2.3. There is good correspondence between the line determined by Eq. (2.58) and points from the simulation results.

For propagation perpendicular to the magnetic field, the electrostatic spectrum exhibits peaks in the vicinity of the lower hybrid frequency, $\omega_{LH}^2 = \omega_{pi}^2 + \Omega_i^2$, and of harmonics of the cyclotron frequency. These peaks correspond to the ion Bernstein modes, which are predicted from warm plasma theory. The analysis of the electron Bernstein modes for the full dynamics electron model has been investigated by Kamimura et al.⁵³ The dispersion relation for perpendicular propagation of the ion Bernstein modes is predicted by⁵⁵

$$1 - \frac{e^{-k^2 a^2}}{k^2 \lambda_{Di}^2} \sum_{n=-\infty}^{\infty} \psi_n(\beta_i) \frac{n\Omega_i}{\omega - n\Omega_i} = 0, \quad (2.59)$$

where $\lambda_{Di}^2 = T_i/M\omega_{pi}^2$, with finite size particle effects included. The power spectrum of the ($k_x = 18\pi m/L_x, k_y = 0$) mode of an electrostatic field is depicted in Fig. 2.4. The parameters for the run that produced this spectrum are: $L_x \times L_y = 128\Delta \times 320\Delta$, $a_x = 1.5\Delta$, $a_y = 15\Delta$, $v_T = 1.0\omega_{pe}\Delta$, $M/m = 1600$, $T_i/T_e = 1.0$, $\Omega_i/\omega_{pi} = 1/3$ and $\theta = 3.1^\circ$. The largest peaks of the spectrum are located at the lower hybrid frequency $\omega_{LH} \sim 3.2\Omega_i$. The spectrum has a zero frequency peak which is a zero frequency "convective mode" originating from the damping of parallel electron motion (Chu et al.⁵⁶). The frequency peaks of the power spectra for the ($k_x, k_y = 0$) modes are plotted as a function of $k\Delta$ in Fig. 2.5. The agreement between the points originating from the simulation results and the lines predicted by Eq. (2.59)

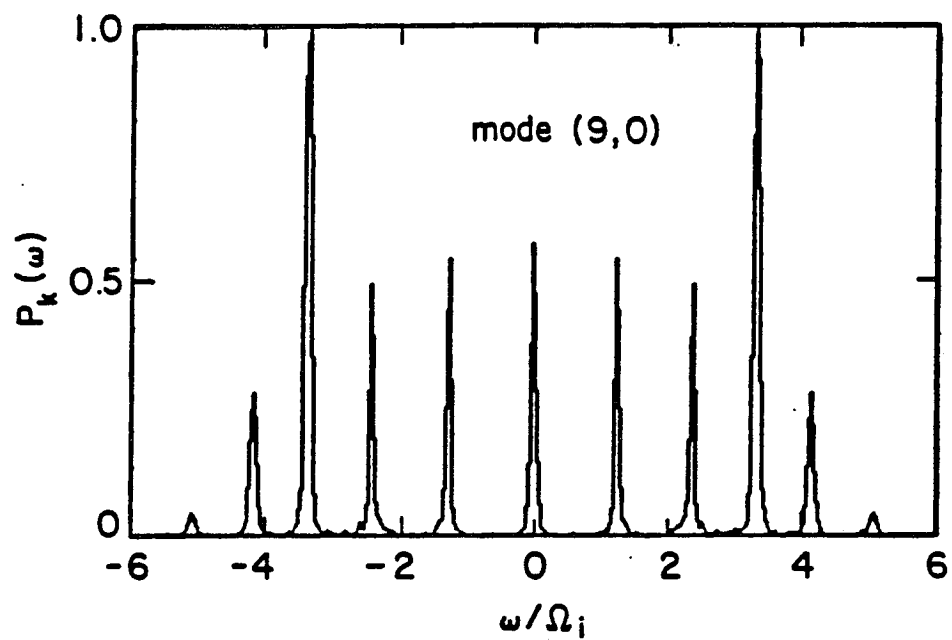


Figure 2.4. Power spectrum for the mode (9,0) from the longitudinal (electrostatic) electric field spectrum.

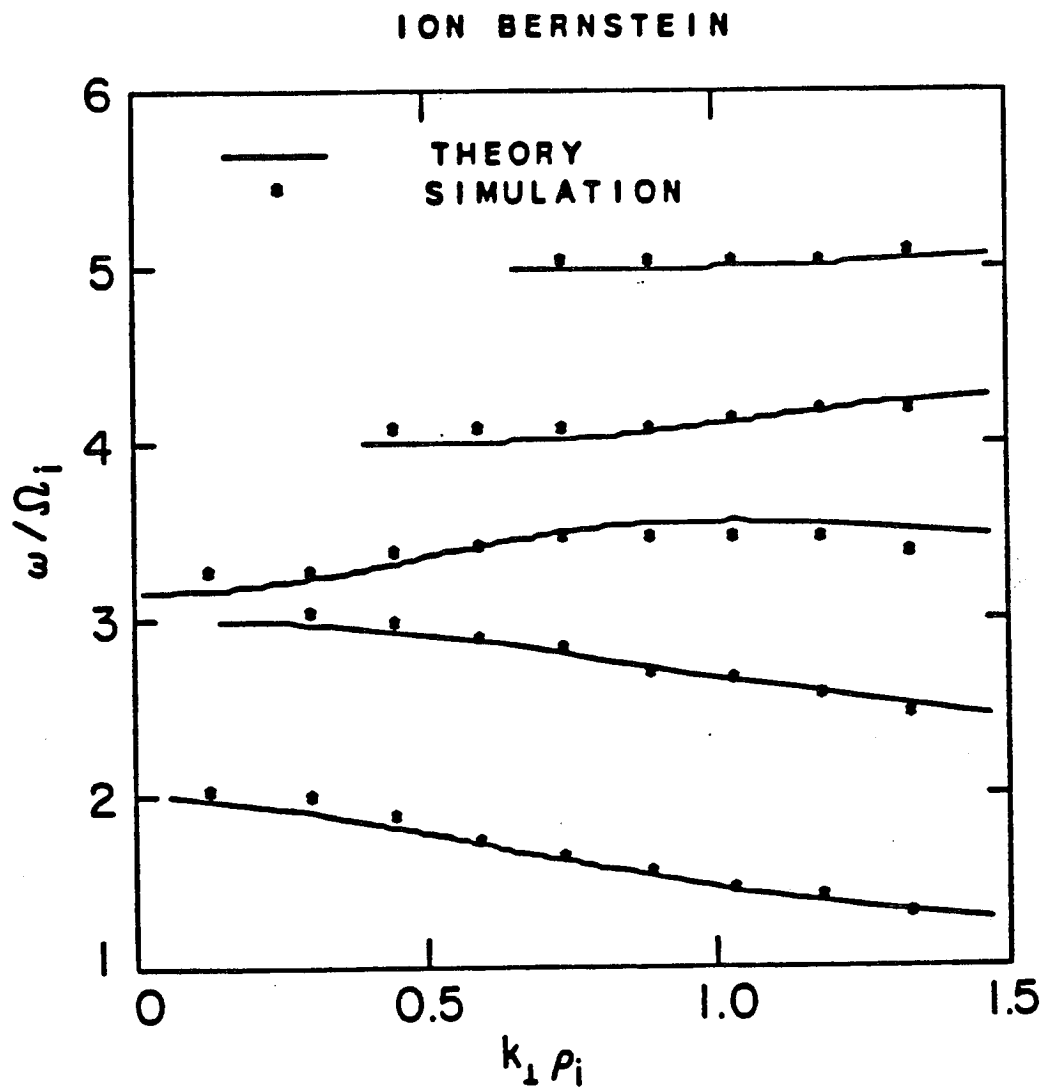


Figure 2.5. Comparison of simulation results with theory for ion Bernstein modes.

is quite good. For the fourth and fifth harmonics of the Bernstein modes, the simulation points do not extend past the values predicted by the theory.

For purely parallel propagation, the two electromagnetic modes predicted by the cold plasma analysis are the Whistler waves and the shear Alfvén waves. These waves are circularly polarized. The Whistler wave rotates in the same direction as the electron cyclotron motion and the shear Alfvén rotates in the same direction as the ion cyclotron motion. The shear Alfvén wave frequency is given by

$$\omega_s = \frac{k^2 v_A^2}{2\Omega_i} e^{k^2 a^2} \left[\left(1 + \frac{4\Omega_i^2}{k^2 v_A^2} e^{-k^2 a^2} \right)^{1/2} - 1 \right]. \quad (2.60)$$

For small k , the frequency ω has an approximately linear relationship to k , $\omega = kv_A$ and, for large k , the frequency approaches the ion cyclotron frequency $\omega = \Omega_i$. The peaks of the simulation frequency spectrum for $(k_x = 0, k_y)$ modes are compared with the cold plasma relation, Eq. (2.60), in Fig. 2.6 for the parameters: $L_x \times L_y = 32\Delta \times 128\Delta$, $a_x = a_y = 1.5\Delta$, $v_T = 0.4\omega_{pe}\Delta$, $M/m = 40$, $T_i/T_e = 1.0$, $\Omega_e/\omega_{pe} = 2.0$, and $\theta = 90^\circ$. There is reasonable correspondence between the simulation points and the theory. The observed differences are within the frequency resolution of the simulation. The simulation which produced these results assumed complete charge neutrality, i.e., electrostatic interactions are neglected. The linear portion of the shear Alfvén branch does not have representative wavenumbers in the simulation in Fig. 2.6. We will be interested in the characteristics of Alfvén waves propagating obliquely to the magnetic field in the following chapters. The linear part of the shear Alfvén wave for oblique propagation is displayed in Fig. 2.7. The $(k_x = 0, k_y)$ modes are plotted from a simulation run with parameters: $L_x \times L_y = 128\Delta \times 320\Delta$, $a_x = 1.5\Delta$, $a_y = 15\Delta$, $v_T = 1.0\omega_{pe}\Delta$, $M/m = 1600$, $T_i/T_e = 1.0$, $\Omega_i/\omega_{pi} = 1/3$, and $\theta = 3.1^\circ$. The

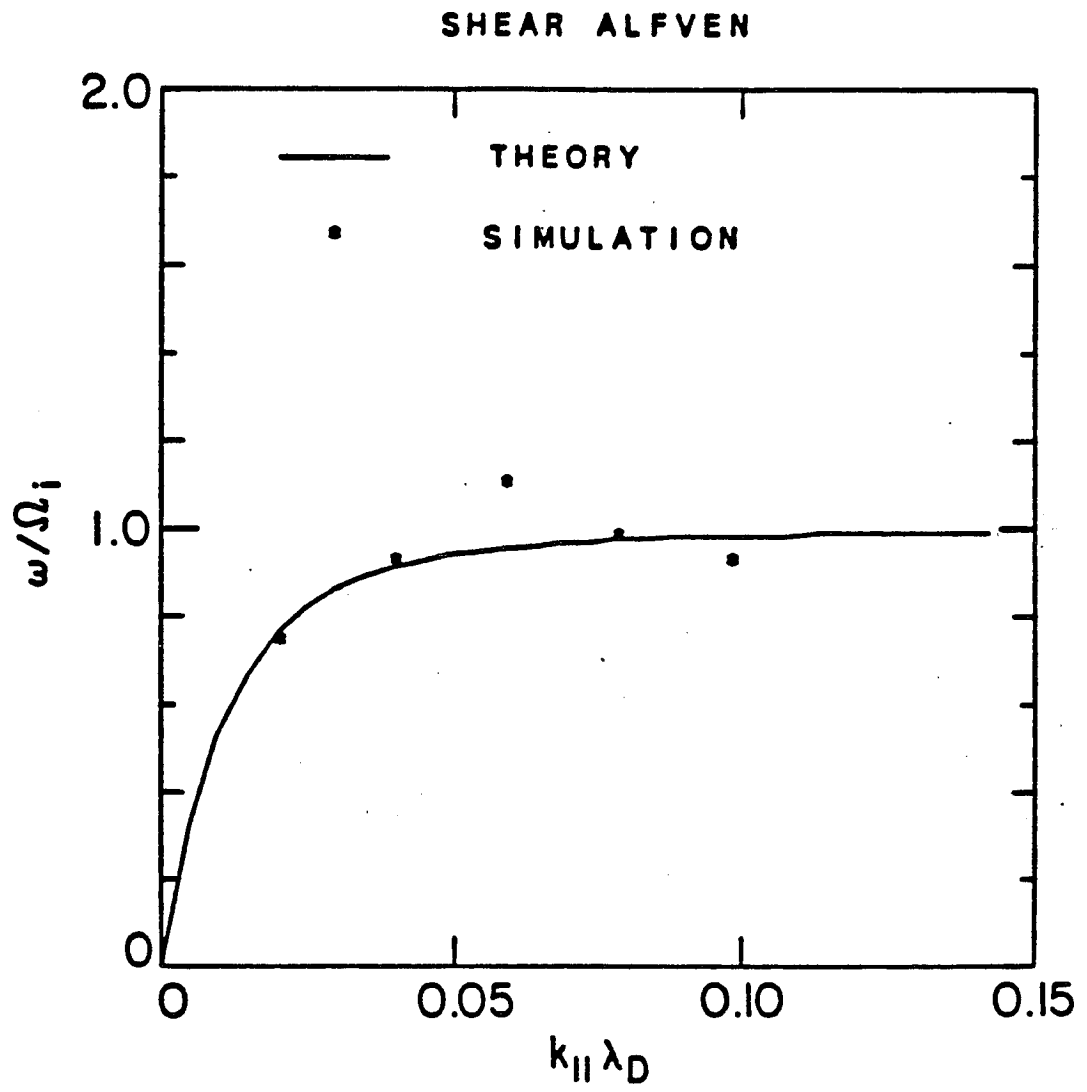


Figure 2.6. Shear Alfvén wave dispersion curves comparing simulation results with cold plasma theory.

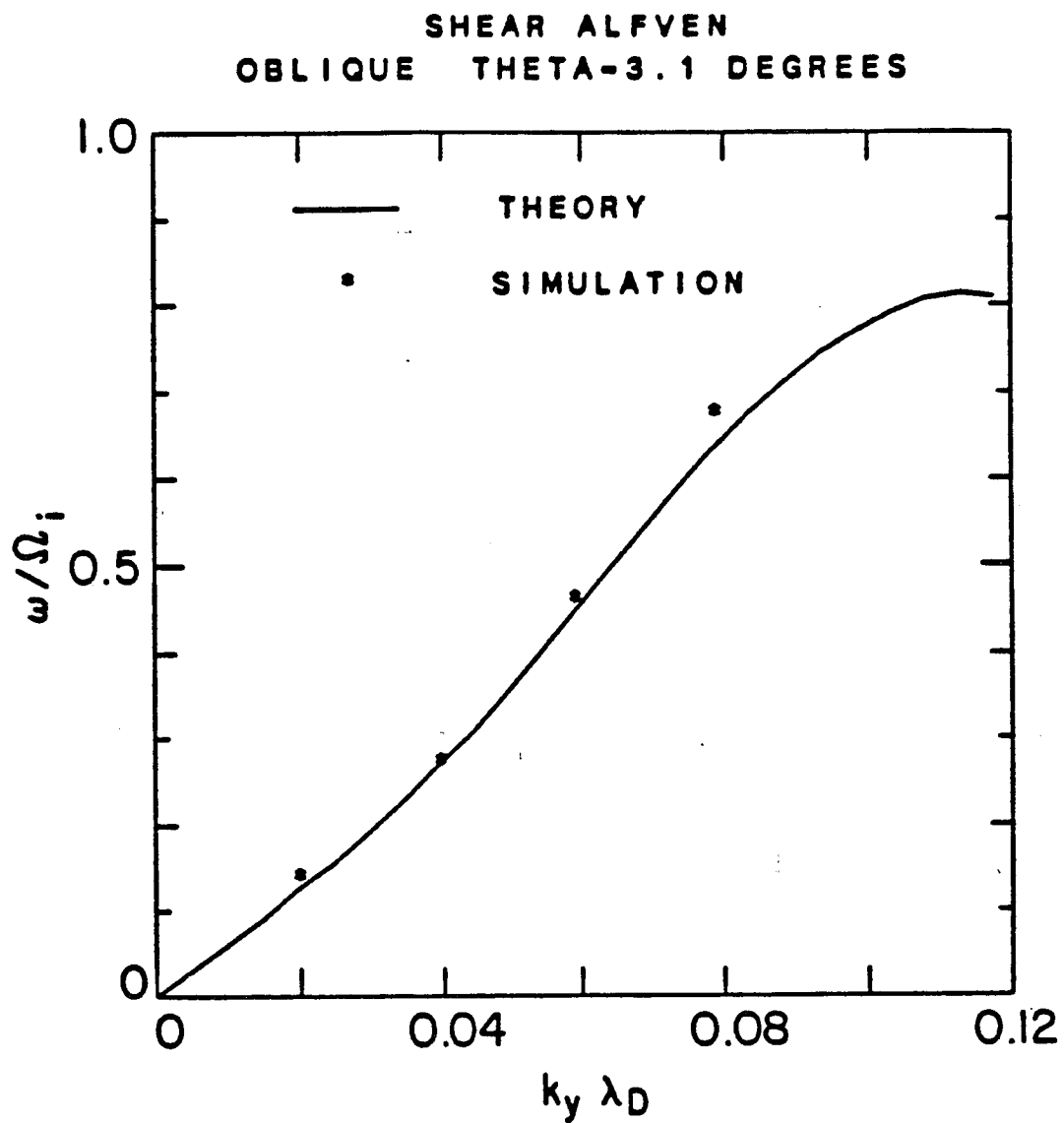


Figure 2.7. Dispersion curves for the shear Alfvén wave propagating obliquely to the ambient magnetic field.

agreement between the simulation results and theory in Fig. 2.7 is quite good. The line in Fig. 2.7 is the prediction from the full cold plasma dispersion relation, Eq. (2.56), including the finite size particle effects. In this case, finite size particle effects shift the Alfvén branch upward in the mid- k domain.

While the shear Alfvén wave is observed in the power spectrum, the Whistler wave is not observed from thermal fluctuations. This is attributed to the lack of thermal electron motion perpendicular to the magnetic field in the model which was mentioned earlier. The thermal ion cyclotron motion is apparently rotating in the wrong direction to couple energy into the Whistler mode. However, the Whistler wave is allowed in the system. This can be seen and was in fact tested by driving a linearly polarized standing wave at the ω and k expected of the parallel propagation Whistler wave from the dispersion relation

$$\omega_w = \frac{k^2 v_A^2}{2\Omega_i} e^{k^2 a^2} \left[\left(1 + \frac{4\Omega_i^2}{k^2 v_A^2} e^{-k^2 a^2} \right)^{1/2} + 1 \right] \quad (2.61)$$

with an antenna. The resulting output data was transformed to circularly polarized fields by the relations

$$B_R = B_x - iB_y$$

$$B_L = B_x + iB_y.$$

For the antenna runs, electrostatic effects are not included. The antenna excited a current defined by

$$\mathbf{J}_A = J_0 \sin(\omega_A t) \sin(k_A y) \hat{k}.$$

In one run, the antenna was driven with the antenna frequency ω_A and wavenumber k_A matching the conditions imposed by Eq. (2.61) for the

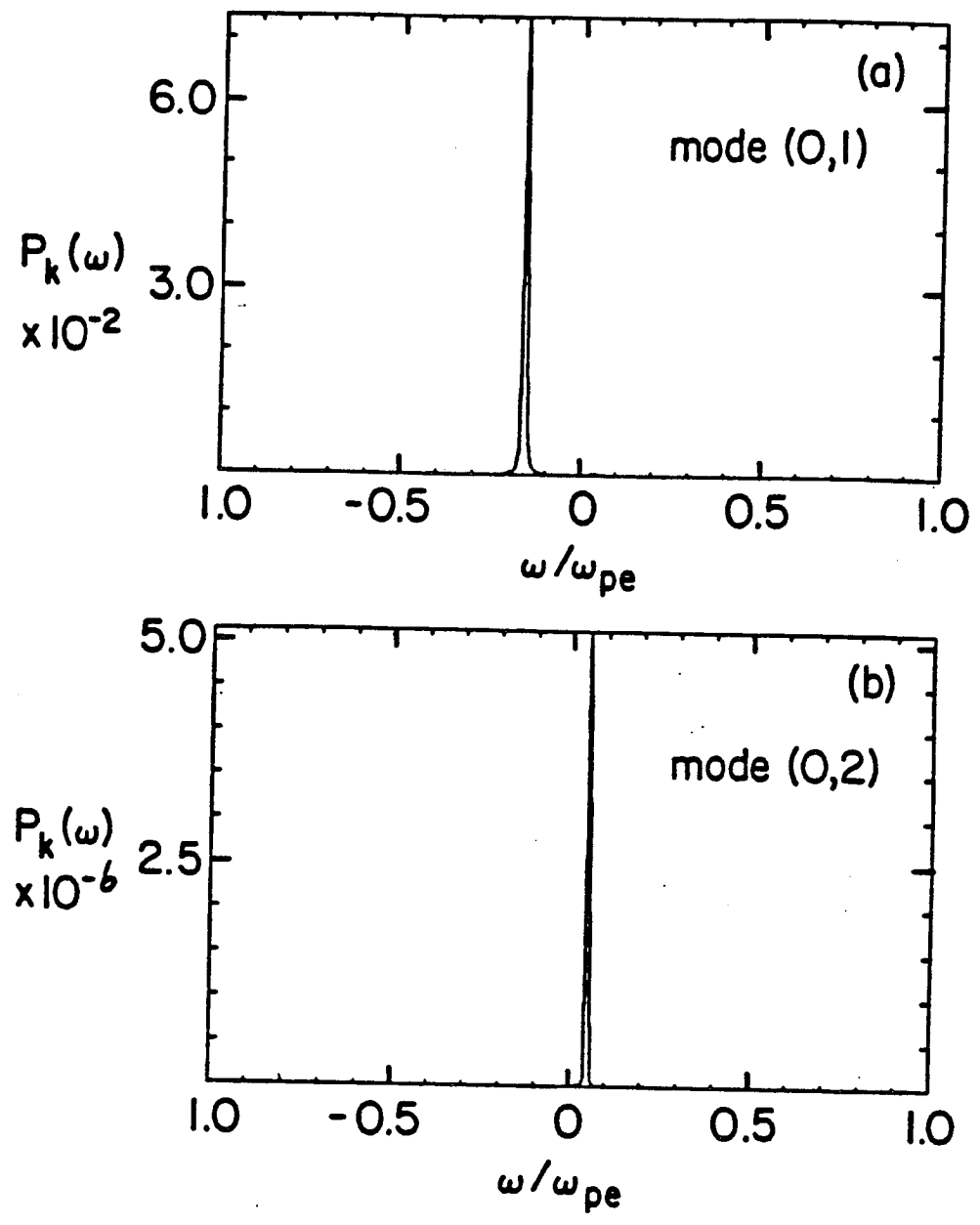


Figure 2.8. Power spectra of the left-polarized magnetic field. The signal in a) is an antenna-driven mode while the signal in b) is from thermal noise.

Whistler wave with parameters $\omega_A/\omega_{pe} = 0.158$, $k_A\Delta = 0.049$, $L_x \times L_y = 32\Delta \times 128\Delta$, $a_x = a_y = 1.5\Delta$, $v_T = 0.4\Delta\omega_{pe}$, $M/m = 40$, $T_i/T_e = 1.0$, $\Omega_e/\omega_{pe} = 2.0$, and $\theta = 90^\circ$. The power spectrum of the left polarized magnetic field, B_L for the $(k_x = 0, k_y = k_A)$ mode is shown in Fig. 2.8a. There is an intense peak at the negative value of the antenna frequency, representing the antenna driven sharp spectrum of the Whistler mode. The power spectra for the thermally excited shear Alfvén wave from the $(k_x = 0, k_y = 2k_A)$ mode for B_L shown in Fig. 2.8b clearly demonstrates that the peak from the antenna response has a circular polarization opposite to the shear Alfvén wave with much less (thermal) power than the antenna power for the Whistler wave. Other runs for an antenna driven at a frequency different from the Whistler frequency exhibited a power spectrum that was not circularly polarized. However, for the same value of J_0 , the height of the power spectra for $\omega \neq \omega_w$ was approximately the same or smaller than the power spectrum for $\omega = \omega_w$. This leads to the conclusion that the simulation model displays the correct response in the dispersion characteristics but that the Whistler wave is not a resonant mode of the model.

As the angle ϕ between \mathbf{k} and \mathbf{B}_0 is increased from 0° to 90° , the Whistler wave merges with the compressional Alfvén wave. The shear Alfvén wave frequency goes to zero in the limit of purely perpendicular propagation. The magnetic field power spectrum for perpendicular propagation is dominated by a zero frequency mode. However, both the shear Alfvén wave and the “magnetized” sound wave have zero frequency in this case. This mode will be discussed further in the next section. The compressional Alfvén is not observed in the power spectrum. This wave seems to depend on the thermal excitation from electron cyclotron motion.

For perpendicular propagation, the transverse electric fields

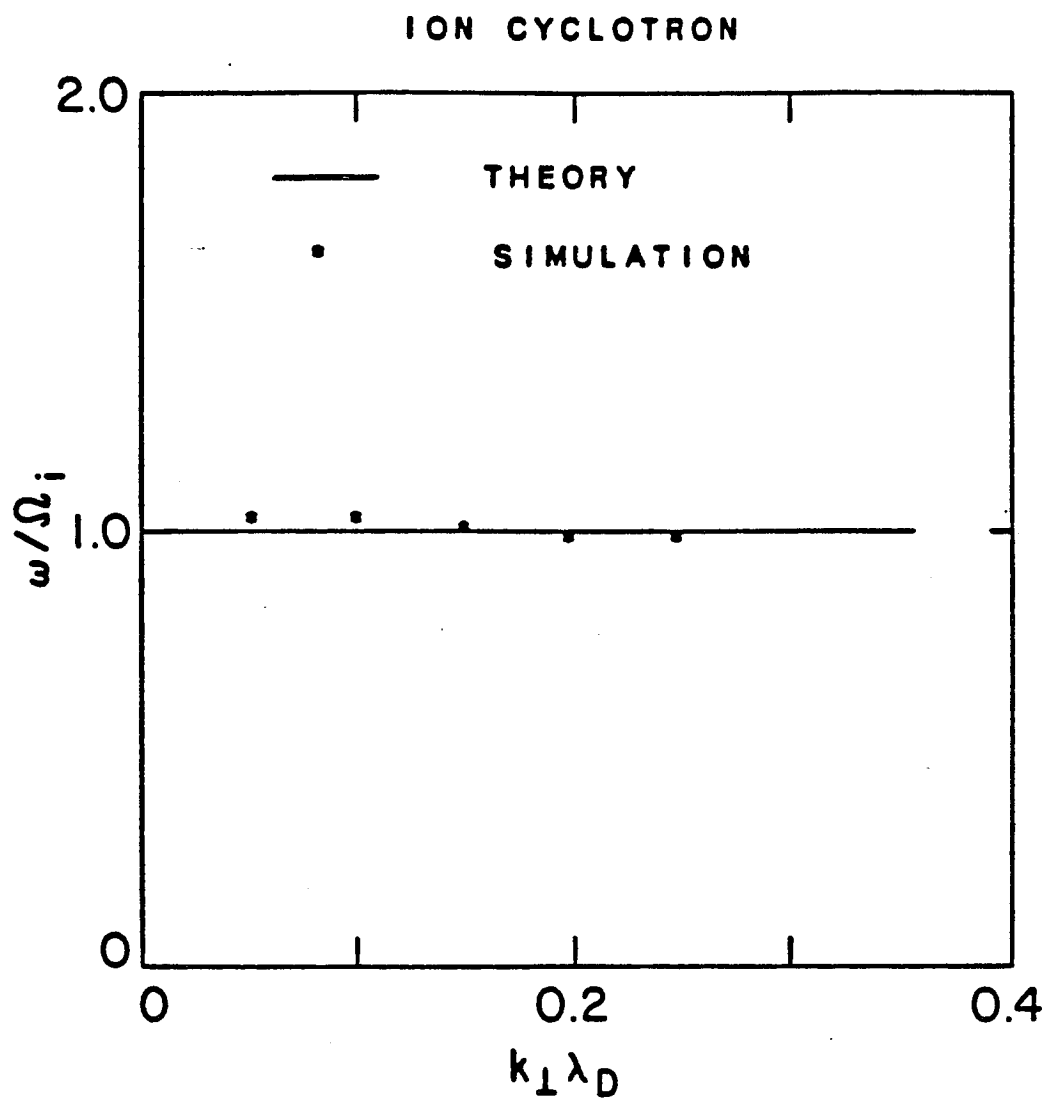


Figure 2.9. Ion cyclotron dispersion curves from the $(k_x, 0)$ modes from the transverse electric field spectrum.

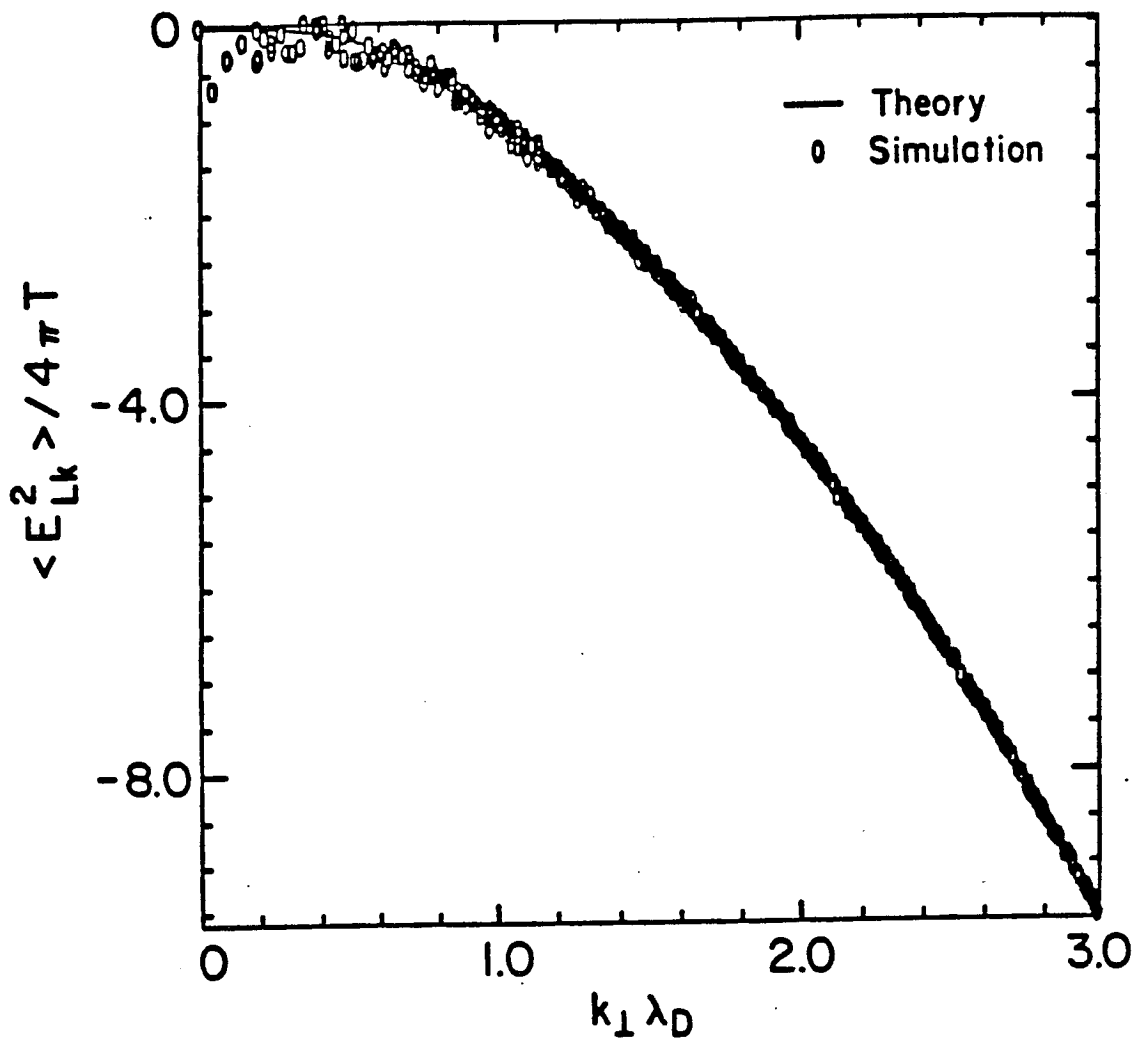


Figure 2.10. Longitudinal electric field fluctuation spectrum.

the simulation observations and the expected values shown in Fig. 2.10 is excellent except for a few long wavelength modes, which take more time to approach equilibrium than the run time.

The level of the magnetic field fluctuations proves to be a function of the angle ϕ between \mathbf{k} and the magnetic field. The magnetic field fluctuations can be obtained if the current density fluctuations are known. The fluctuations of the current density can be computed from the linear response function using the fluctuation dissipation theorem.⁵⁷ The time averaged fluctuation spectrum of the magnetic field, $\langle B^2 \rangle_{\mathbf{k}} / 4\pi T$, is depicted in Fig. 2.11. This test run has the parameters: $L_x \times L_y = 32\Delta \times 128\Delta$, $a_x = a_y = 1.5\Delta$, $V_T = 0.4\omega_{pe}\Delta$, $M/m = 40$, $T_i/T_e = 1.0$, $\Omega_e/\omega_{pe} = 2.0$, and $\theta = 90^\circ$. The fluctuation spectra were averaged over approximately 8 cyclotron periods. The bottom line of points in Fig. 2.11 correspond to modes where $k_\perp = k_x = 0$. The fluctuation levels increase sharply as the angle ϕ between \mathbf{k} and \mathbf{B}_0 increases.

The fluctuation spectra are calculated for an isothermal, anisotropic plasma. The simulation model is effectively composed of three different species responses, electron motion perpendicular to the magnetic field, electron motion parallel to the magnetic field, and ion motion. The perpendicular electron motion is uncoupled to fluctuation energy, and thus yields an effective zero temperature. Generalizing the fluctuation-dissipation theorem, A.G. Sitenko⁵⁹ has calculated the current density fluctuations in an infinite, nonisothermal plasma in terms of the imaginary (dissipative) part of the response function to be

$$\begin{aligned} \langle J_i J_j \rangle_{\mathbf{k}, \omega} &= i\omega [\gamma_{ik} A_{km}^{-1}]^* \\ &\times [\gamma_{jl} A_{ln}^{-1}] \sum_{\alpha} T^{\alpha} (\chi_{mn}^{*\alpha} - \chi_{nm}^{\alpha}) \end{aligned} \quad (2.63)$$

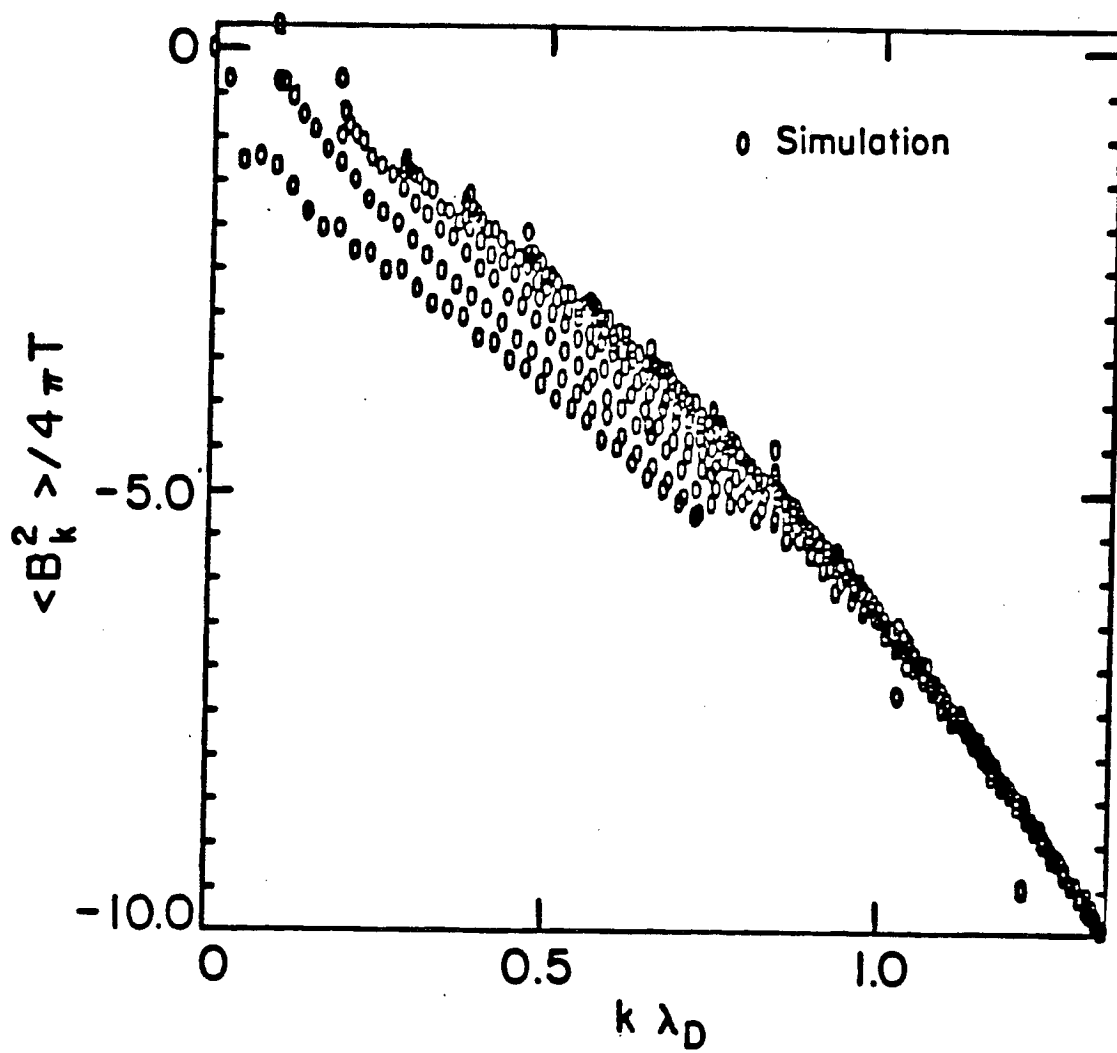


Figure 2.11. Magnetic field fluctuation spectrum for propagation vectors both parallel and perpendicular to the magnetic field.

where γ_{ij} and Λ_{ij} are given by Eqs. (2.48) and (2.50), where \sum_{α} denotes the sum over different species, and where T^{α} is the temperature of species α .

Following Sitenko,⁵⁹ let us introduce the tensor λ_{ij} whose elements are the cofactors of the dispersion tensor Λ_{ij} . By definition,

$$\Lambda_{ij}\lambda_{jk} = \Lambda\delta_{ik}.$$

The elements of λ_{ij} are expressed in terms of the elements of Λ_{ij} by means of the formula

$$\lambda_{ij} = 0.5\mathcal{E}_{ikl}\mathcal{E}_{jmn}\Lambda_{mk}\Lambda_{nl} \quad (2.64)$$

where \mathcal{E}_{ijk} is the fully antisymmetric tensor. The inverse Λ_{ij}^{-1} is given by the relation

$$\Lambda_{ij}^{-1} = \frac{\lambda_{ij}}{\Lambda}$$

from the above expression. The current density fluctuations from Eq. (2.63) can then be expressed as

$$\langle J_i J_j \rangle = i\omega \frac{\gamma_{ik}\lambda_{km}^*\gamma_{jl}\lambda_{ln}}{|\Lambda|^2} \sum_{\alpha} T^{\alpha} (\chi_{mn}^{\alpha*} - \chi_{nm}^{\alpha}). \quad (2.66)$$

Inspection of the above formula indicates that the fluctuation spectrum has sharp peaks near the normal modes of plasma oscillation because of zeroes in the dispersion relation of the denominator, given by $\Lambda = 0$. For simplicity, we adopt the cold plasma theory to evaluate magnetic field fluctuations. This should be a reasonable approximation as long as the cold plasma theory can predict those weakly damped modes that contain the most energy.

For our model, the current density fluctuation spectrum can be obtained from Eq. (2.66) to be

$$\begin{aligned} \langle J_i J_j \rangle_{\mathbf{k}, \omega} = & \frac{i\omega}{|\Lambda|^2} \left\{ T_{\parallel}^e \gamma_{ik}\lambda_{k3}^*\gamma_{jl}\lambda_{l3} (\chi_{33}^{e*} - \chi_{33}^e) \right. \\ & \left. + T^i \gamma_{ik}\lambda_{kn}^*\gamma_{jl}\lambda_{ln} (\chi_{mn}^{i*} - \chi_{nm}^i) \right\} \quad (2.67) \end{aligned}$$

where the background magnetic field points in the z -direction. From Eq. (2.36), the magnetic field fluctuation spectrum can be computed by

$$\frac{\langle B^2 \rangle_{\mathbf{k}, \omega}}{8\pi} = \frac{2\pi}{k^2 c^2} \left[\langle J^2 \rangle_{\mathbf{k}, \omega} - \frac{\langle k_i J_i k_j J_j \rangle_{\mathbf{k}, \omega}}{k^2} \right] \quad (2.68)$$

if the current density fluctuations are known. The integration of Eq. (2.68) over all frequencies yields the time averaged fluctuation spectrum of the magnetic field

$$\frac{\langle B^2 \rangle_{\mathbf{k}}}{8\pi} = \int \frac{\langle B^2 \rangle_{\mathbf{k}, \omega}}{8\pi} \frac{d\omega}{2\pi}. \quad (2.69)$$

The dispersion tensor contains the information for determining the current density fluctuations which subsequently can yield the magnetic field fluctuation spectrum. The explicit calculation of the fluctuation spectrum in terms of the dispersion matrix for the general case will not be presented here. We shall examine the special cases where wave propagation is either completely parallel or perpendicular to the background magnetic field.

Let us first investigate fluctuation spectra for propagation parallel to the magnetic field. The magnetic field fluctuation spectrum in Eq. (2.68) reduces to

$$\frac{\langle B^2 \rangle_{\mathbf{k}, \omega}}{8\pi} = \frac{2\pi}{k^2 c^2} \left[\langle J_x^2 \rangle_{\mathbf{k}, \omega} + \langle J_y^2 \rangle_{\mathbf{k}, \omega} \right]. \quad (2.70)$$

The tensor γ_{ij} is diagonal having the values

$$\begin{aligned} \gamma_{11} = \gamma_{22} &= \frac{-k^2 c^2}{\omega^2} \\ \gamma_{33} &= -1. \end{aligned}$$

From Eq. (2.67), the xx -component of the current density fluctuation matrix becomes

$$\begin{aligned} \langle J_x^2 \rangle_{\mathbf{k}, \omega} &= \frac{i\omega}{|A|^2} \frac{k^4 c^4}{\omega^4} \left\{ T_{e||} |\lambda_{13}|^2 \left(\chi_{33}^{*e} - \chi_{33}^e \right) \right. \\ &\quad \left. + T^i \lambda_{1m}^* \lambda_{1n} \left(\chi_{mn}^{i*} - \chi_{nm}^i \right) \right\}. \end{aligned} \quad (2.71)$$

The elements λ_{11} , λ_{12} , and λ_{13} of the cofactor tensor λ_{ij} and are defined by

$$\begin{aligned}\lambda_{11} &= A_{22}A_{33} - A_{23}A_{32} \\ \lambda_{12} &= A_{23}A_{31} - A_{21}A_{33} \\ \lambda_{13} &= A_{21}A_{32} - A_{22}A_{31}.\end{aligned}$$

Using Eqs. (2.50), (2.52), and (2.53) for Maxwell's equations and cold fluid response of the particles demonstrates that the elements $A_{13} = A_{23} = A_{31} = A_{32} = 0$ for the propagation angles $\phi = 0^\circ$ and $\phi = 90^\circ$. The elements λ_{ij} simplify to

$$\begin{aligned}\lambda_{11} &= A_{22}A_{33} \\ \lambda_{12} &= -A_{21}A_{33} \\ \lambda_{13} &= 0.\end{aligned}$$

The formula for $\langle J_x^2 \rangle_{\mathbf{k}, \omega}$ from Eq. (2.71) becomes

$$\langle J_x^2 \rangle_{\mathbf{k}, \omega} = \frac{i\omega}{|A|^2} \frac{k^4 c^4}{\omega^4} \left[T^i \lambda_{1m}^* \lambda_{1n} \left(\chi_{mn}^{i*} - \chi_{nm}^i \right) \right] m, n \neq 3.$$

It is convenient at this point to replace the matrix λ_{ij} by the inverse dispersion tensor A_{ij}^{-1} such that

$$\langle J_x^2 \rangle_{\mathbf{k}, \omega} = \frac{i}{\omega} \frac{k^4 c^4}{\omega^2} \left[T^i A_{1m}^{-1*} A_{1n}^{-1} \left(\chi_{mn}^{i*} - \chi_{nm}^i \right) \right] m, n \neq 3. \quad (2.72)$$

From Eq. (2.50), it can be shown that

$$\chi_{mn}^{i*} - \chi_{nm}^i = \frac{1}{4\pi} (A_{mn}^* - A_{nm}) \quad m, n \neq 3$$

where we have used the relations

$$\gamma_{ij} = \gamma_{ij}^* = \gamma_{ji}$$

$$\chi_{mn}^e = -\chi_{nm}^e = -\chi_{mn}^{e*} \quad m, n \neq 3.$$

Combining this with Eq. (2.7) yields the expression for $\langle J_x^2 \rangle$ shown below

$$\langle J_x^2 \rangle_{\mathbf{k},\omega} = \frac{iT^i k^4 c^4}{4\pi\omega \omega^2} \left(A_{11}^{-1} - A_{11}^{-1*} \right). \quad (2.73)$$

A similar calculation for $\langle J_y^2 \rangle$ reveals that

$$\langle J_y^2 \rangle = \frac{iT^i k^4 c^4}{4\pi\omega \omega^2} \left(A_{22}^{-1} - A_{22}^{-1*} \right). \quad (2.74)$$

The current density fluctuations are now expressed in a simpler form than earlier and are now amenable to evaluation from the dispersion tensor A_{ij} .

The expression for the magnetic field fluctuation from Eqs. (2.70), (2.73), and (2.74) is

$$\frac{\langle B^2 \rangle_{\mathbf{k},\omega}}{8\pi} = \frac{iT^i k^2 c^2}{2\omega \omega^2} \left[\frac{\lambda_{11} + \lambda_{22}}{A} - c.c. \right] \quad (2.75)$$

where c.c. is used to denote the complex conjugate. When $\phi=0$, it can be seen that

$$\frac{\lambda_{11} + \lambda_{22}}{A} = \frac{A_{11} + A_{22}}{A_{11}A_{22} + A_{12}^2}.$$

The elements A_{11} , A_{12} , and A_{22} can be computed from Eqs. (2.50), (2.52), and (2.53) to yield

$$\frac{\langle B^2 \rangle_{\mathbf{k},\omega}}{8\pi} = \frac{iT^i k^2 c^2}{2\omega \omega^2} \times \left\{ \frac{2 \left(\frac{k^2 c^2}{\omega^2} + \frac{\omega_{pi}^2}{\omega^2 - \Omega_i^2} \right)}{\left[\frac{\omega_{pi}^2}{\Omega_i(\omega + \Omega_i)} - \frac{k^2 c^2}{\omega^2} \right] \left[\frac{\omega_{pi}^2}{\Omega_i(\omega - \Omega_i)} + \frac{k^2 c^2}{\omega^2} \right]} - c.c. \right\} \quad (2.76)$$

The dispersion relations for the Whistler and the shear Alfvén waves propagating parallel to the magnetic field are obtained from equating the denominator of Eq. (2.76) to zero.

To obtain the time averaged spectrum, Eq. (2.76) is integrated over ω as described by Eq. (2.68). The resulting integral has the form

$$\frac{f(\omega)}{\omega - \omega'} d\omega$$

where ω' is the resonant frequency of a normal mode. Certain mathematical difficulties are encountered here. The undamped ideal normal modes have purely real frequencies so that the above type of integral over frequency encounters a singularity along the real axis of ω . Physical arguments show how to avoid the singularity. Since the cold plasma undamped modes are idealized from the thermal weakly damped modes, it is natural to introduce a small imaginary frequency for damping to the (complex) frequency upon integration. From the theory of analytic functions, the integral contribution by the finite damping part can be analytically continued to the infinitesimally small damping part. A vanishingly small damping frequency is added to the cold plasma resonances allowing the use of the Plemelj formula

$$\lim_{\nu \rightarrow 0} \int_{-\infty}^{\infty} \frac{f(\omega)}{\omega - \omega' + i\nu} d\omega = P \int_{-\infty}^{\infty} \frac{f(\omega)}{\omega - \omega'} d\omega - \pi i \int_{-\infty}^{\infty} f(\omega) \delta(\omega - \omega') d\omega$$

to evaluate the integral. Since the relevant integral contains a function minus its complex conjugate, we find that

$$\lim_{\nu \rightarrow 0} \int_{-\infty}^{\infty} \left[\frac{f(\omega)}{\omega - \omega' + i\nu} - c.c \right] \times d\omega = -2\pi i \int_{-\infty}^{\infty} f(\omega) \delta(\omega - \omega') d\omega \quad (2.77)$$

since only the imaginary part of the integral survives.

The observed power spectra for the magnetic field reveal that, for parallel propagation, most of the energy is deposited in the shear Alfvén

mode. Therefore the Plemelj formula is applied only to the poles representing the shear Alfvén resonance of Eq. (2.76). From Eqs. (2.68), (2.76) and (2.77), the magnetic field fluctuation spectrum is

$$\frac{\langle B^2 \rangle_{\mathbf{k}}}{8\pi} = \int_{-\infty}^{\infty} \frac{T^i k^2 v_A^2 [\omega^2 (k^2 c^2 + \omega_{pi}^2) - k^2 c^2 \Omega_i^2]}{\omega \omega_{pi}^2 (\omega - \omega_w^2)} \left[\frac{\delta(\omega - \omega_s)}{(\omega + \omega_s)} + \frac{\delta(\omega + \omega_s)}{(\omega - \omega_s)} \right] d\omega$$

where ω_s and ω_w are the shear Alfvén and Whistler resonance frequencies. After some algebraic manipulation, we find that

$$\frac{\langle B^2 \rangle_{\mathbf{k}}}{8\pi} = T^i \left(1 + \frac{4\Omega_i^2}{k^2 v_A^2} \right)^{-1/2} \left[\frac{\Omega_i^2}{\omega_s^2} - \left(1 + \frac{\omega_{pi}^2}{k^2 c^2} \right) \right]. \quad (2.78)$$

The inclusion of finite size particle effects and the periodicity of the simulation plasma modifies Eq. (2.78) to

$$V \frac{\langle B^2 \rangle_{\mathbf{k}}}{4\pi T^i} = 2 \left[1 + \frac{4\Omega_i^2}{k^2 v_A^2} e^{-k^2 a^2} \right]^{-1/2} \left[\frac{\Omega_i^2}{\omega_s^2} - \left(1 + \frac{\omega_{pi}^2 e^{-k^2 a^2}}{k^2 c^2} \right) \right]. \quad (2.79)$$

where ω_s is given by Eq. (2.61). The bottom line of points of Fig. 2.11 correspond to modes that propagate parallel to the magnetic field. These points are plotted in Fig. 2.12 along with a line described by Eq. (2.79). There is excellent agreement between the simulation results and the prediction from Eq. (2.79). If the contribution from the pole representing the Whistler wave is evaluated with the shear Alfvén wave, the fluctuation spectra is given by

$$\frac{\langle B^2 \rangle_{\mathbf{k}}}{8\pi} = T^i.$$

There is an equipartition of energy between the shear Alfvén and Whistler modes when both modes are thermally excited.

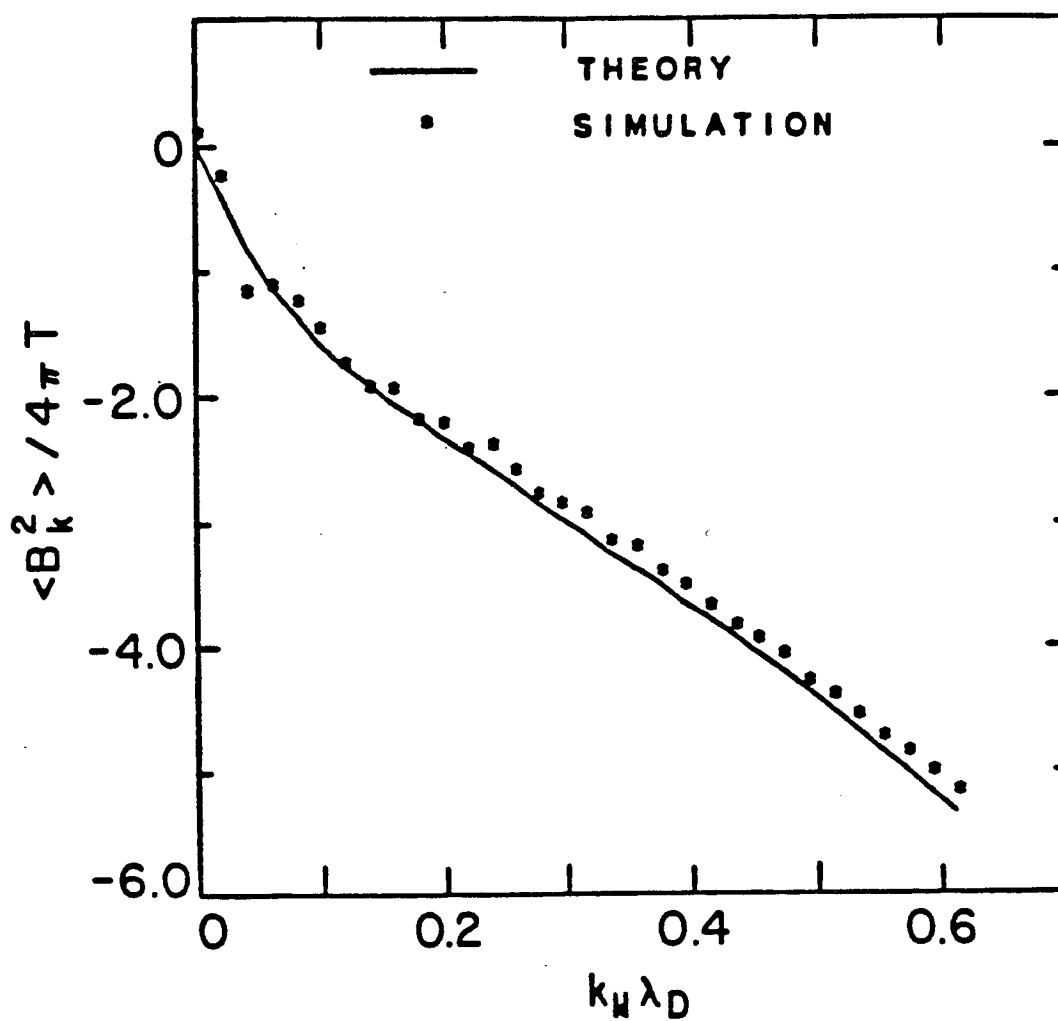
FLUCTUATION DISSIPATION
PARALLEL PROPAGATION

Figure 2.12. Time-averaged magnetic field fluctuation spectrum for propagation purely parallel to the magnetic field.

Let us now investigate the magnetic field fluctuation spectrum for wave propagation perpendicular to the magnetic field. The magnetic field fluctuations are given by

$$\frac{\langle B^2 \rangle_{\mathbf{k}, \omega}}{8\pi} = \frac{2\pi}{k^2 c^2} \left[\langle J_y^2 \rangle_{\mathbf{k}, \omega} + \langle J_z^2 \rangle_{\mathbf{k}, \omega} \right] \quad (2.80)$$

from Eq. (2.67). The matrix γ_{ij} is diagonal again with values

$$\begin{aligned} \gamma_{11} &= 1 \\ \gamma_{22} &= \gamma_{33} = -n^2. \end{aligned}$$

From Eq. (2.66), the yy -element of the current density fluctuation spectrum becomes

$$\langle J_y^2 \rangle_{\mathbf{k}, \omega} = \frac{i\omega k^4 c^4}{|A|^2 \omega^4} \left\{ T_{\parallel}^e |\lambda_{23}|^2 (\chi_{33}^{e*} - \chi_{33}^e) + T^i \lambda_{2m}^* \lambda_{2n} (\chi_{mn}^{i*} - \chi_{nm}^i) \right\}$$

and the zz -element becomes

$$\langle J_z^2 \rangle_{\mathbf{k}, \omega} = \frac{i\omega k^4 c^4}{|A|^2 \omega^4} \left\{ T_{\parallel}^e |\lambda_{33}|^2 (\chi_{33}^{e*} - \chi_{33}^e) + T^i \lambda_{3m}^* \lambda_{3n} (\chi_{mn}^{i*} - \chi_{nm}^i) \right\}.$$

The cofactor matrix, λ_{ij} , of the dispersion tensor has elements

$$\begin{aligned} \lambda_{21} &= A_{33} A_{12} \\ \lambda_{22} &= A_{11} A_{33} \\ \lambda_{33} &= A_{11} A_{22} + A_{12}^2 \\ \lambda_{23} &= \lambda_{31} = \lambda_{32} = 0 \end{aligned} \quad (2.81)$$

for a cold plasma with propagation perpendicular to the magnetic field. Using these, it can be shown that

$$\langle J_y^2 \rangle_{\mathbf{k}, \omega} = \frac{iT^i k^4 c^4}{4\pi\omega \omega^2} [A_{22}^{-1} - c.c] \quad (2.82)$$

and

$$\langle J_z^2 \rangle_{\mathbf{k}, \omega} = \frac{i k^4 c^4 |\lambda_{33}|^2}{\omega \omega^2 |A|^2} \left\{ T_{\parallel}^e (\chi_{33}^{e*} - \chi_{33}^e) + T^i (\chi_{33}^{i*} - \chi_{33}^i) \right\}.$$

The magnetic field fluctuation spectrum depends on both the electron and ion temperatures for perpendicular propagation whereas for parallel propagation, it depends only on the ion temperature.

For the test results displayed here, the electron temperature is equal to the ion temperature such that $T_{\parallel}^e = T^i = T$. In this instance, the zz -element of the current density fluctuation matrix simplifies from Eq. (2.83) to

$$\langle J_z^2 \rangle_{\mathbf{k}, \omega} = \frac{iT k^4 c^4}{4\pi\omega \omega^2} [A_{33}^{-1} - c.c]. \quad (2.84)$$

The magnetic field fluctuation spectrum for perpendicular propagation is given by

$$\frac{\langle B^2 \rangle_{\mathbf{k}, \omega}}{8\pi} = \frac{iT k^2 c^2}{2\omega \omega^2} [A_{22}^{-1} + A_{33}^{-1} - c.c] \quad (2.85)$$

from Eqs. (2.80), (2.82), and (2.84).

The observations of the power spectra indicate that most of the energy is deposited in a zero-frequency mode when $k_{\parallel} = 0$. The first term in brackets in Eq. (2.85), A_{22}^{-1} yields

$$A_{22}^{-1} = \frac{\lambda_{22}}{A} = \frac{A_{11}}{A_{11}A_{22} + A_{12}^2}.$$

This term contributes only to the compressional Alfvén wave resonant terms. The zero-frequency wave is not one that is derived from the Vlasov equation. This mode has been proposed as a mechanism responsible for electron diffusion across the magnetic field by Chu, Chu, and Ohkawa.⁶⁰ The electron parallel momentum equation, (2.4), has dissipation added as follows⁶⁰

$$\frac{dv_{ez}}{dt} = \frac{-e}{m} E_z + \mu \nabla^2 v_{ez} - \nu v_{ez}$$

where ν is the electron-ion collision frequency and μ is the kinematic electron viscosity. The zz -element of the electron susceptibility tensor, χ_{33} , is given by

$$4\pi\chi_{33} = \frac{-\omega_{pe}^2}{\omega(\omega + i\eta)},$$

where $\eta = \nu + \mu k^2$, from this modified equation of motion. The zz -element of the dispersion tensor is subsequently given by

$$A_{33} = \frac{-k^2 c^2}{\omega^2} - \frac{\omega_{pi}^2}{\omega^2} - \frac{\omega_{pe}^2}{\omega(\omega + i\eta)}. \quad (2.86)$$

The magnetic field fluctuation spectrum from Eq. (2.85) becomes

$$\frac{\langle B^2 \rangle_{\mathbf{k}, \omega}}{8\pi} = \frac{-iT k^2 c^2}{2\omega \omega^2} \left[\frac{1}{\frac{k^2 c^2}{\omega^2} + \frac{\omega_{pi}^2}{\omega^2} + \frac{\omega_{pe}^2}{\omega(\omega + i\eta)}} - c.c. \right].$$

The contribution from $\langle J_y^2 \rangle$ has been neglected since it contains the compressional Alfvén resonance which was not observed in the thermal spectrum. Further evaluation of the magnetic field fluctuation spectrum reveals that

$$\frac{\langle B^2 \rangle_{\mathbf{k}, \omega}}{8\pi} = T \frac{k^2 c^2}{\omega_p^2 + k^2 c^2} \frac{\eta - \gamma}{\omega^2 + \gamma^2} \quad (2.87)$$

where

$$\gamma = \frac{\eta(k^2 c^2 + \omega_{pi}^2)}{k^2 c^2 + \omega_p^2}.$$

Noting that

$$\int \frac{d\omega}{\omega^2 + \gamma^2} = \frac{\pi}{\gamma},$$

the time averaged fluctuation spectrum is given by

$$\frac{\langle B^2 \rangle_{\mathbf{k}}}{8\pi} = \frac{T}{2} \frac{k^2 c^2 \omega_{pe}^2}{(k^2 c^2 + \omega_{pi}^2)} \frac{1}{(\omega_{pe}^2 + k^2 c^2 + \omega_{pi}^2)}. \quad (2.88)$$

If the ion response is ignored, Eq. (2.88) reduces to the more familiar form

$$\frac{\langle B^2 \rangle_{\mathbf{k}}}{8\pi} = \frac{T}{2} \frac{1}{1 + \frac{k^2 c^2}{\omega_{pe}^2}}.$$

Finite size particle effects and the periodicity of the simulation volume modify the above relation to

$$V \frac{\langle B^2 \rangle_{\mathbf{k}}}{4\pi T} = \frac{1}{1 + \frac{k^2 c^2 e k^2 a^2}{\omega_{pe}^2}}, \quad (2.89)$$

which agrees with the equation reported also by Dawson.⁴⁰ The contribution from the pole associated with the compressional Alfvén wave resonance is much smaller than the contribution from the zero frequency mode. These results are approximately the same as for a model with full dynamics electrons. Simulation results are depicted in Fig. 2.13 for the parameters: $L_x \times L_y = 128\Delta \times 32\Delta$, $a_x = a_y = 1.5\Delta$, $v_T = 1.0\omega_{pe}\Delta$, $M/m = 40.0$, $T_i/T_e = 1.0$, $\Omega_e/\omega_{pe} = 2.0$, and $\theta = 0^\circ$. The spectrum is averaged over approximately 16 ion cyclotron periods. The fluctuation spectrum is somewhat noisy but there is good corroboration between the simulation results and Eq. (2.90). Magnetic field fluctuations can take a longer time to equilibrate than electrostatic fluctuations, particularly when it is a zero frequency mode.

The general relations for the fluctuation spectra based on the fluctuation dissipation theorem have been presented in this section. The electrostatic spectrum agrees very well with the theoretical expectations. The magnetic field fluctuation spectrum has been explicitly calculated for propagation perpendicular and parallel to the magnetic field with good agreement with the simulation results.

2.8 Boundary Effects

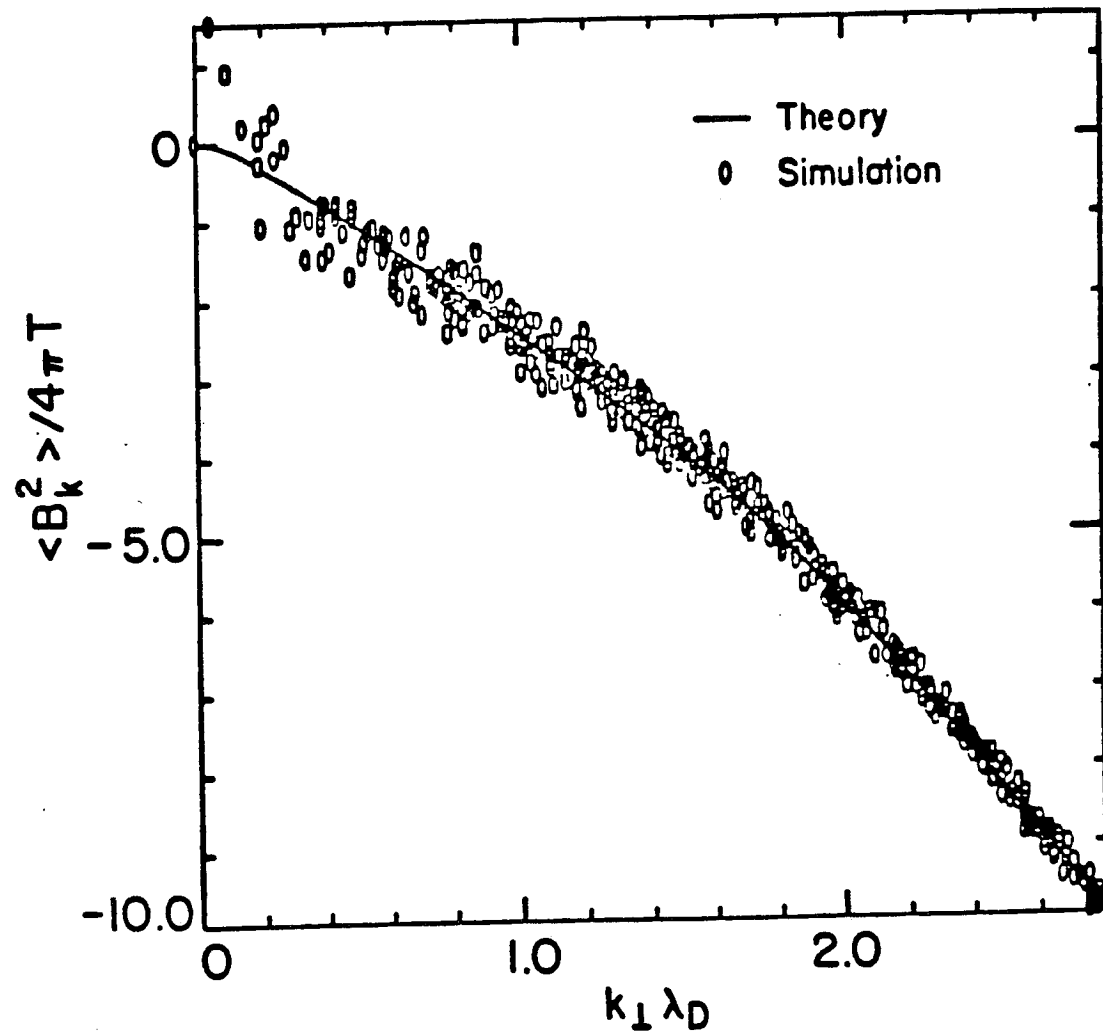


Figure 2.13. Time-averaged magnetic field fluctuation spectrum for propagation purely perpendicular to the magnetic field.

The modelling of driven Alfvén waves in an inhomogeneous system requires bounding the simulation system. This section discusses effects introduced by the presence of boundaries. A comprehensive treatment of boundary conditions and their effects on particle simulation models has not yet been published. However, boundary conditions imposed on a simulation plasma may have unintended consequences. The sources of unwanted effects for simulation codes generally belong in one of two categories: 1. particle reflection at the boundary generates surface currents (Naitou et al.⁵⁰), and 2. surface fields may couple to particles near the boundary to generate an instability (Swift and Ambrosiano⁶¹).

As an example of unexpected behavior arising from the presence of boundaries, we shall examine how this particle model reacts when the background magnetic field points in the z -direction perpendicular to the plane of particle motion. There were certain regions near the particle reflection boundaries where electrons tended to accumulate and other regions also near the particle boundaries that electrons vacated. As time progressed, these tendencies continued to grow. This behavior was also seen for purely electrostatic models with perpendicular guiding center electron motion when the boundary conditions $\Phi'(0) = \Phi'(L_x/2) = 0$ were applied at the edges. This behavior was not observed when the boundary conditions $\Phi(0) = \Phi(L_x/z) = 0$ were applied to the electrostatic code.

The $\Phi' = 0$ boundary condition allows E_y to have a nonzero value at the boundary. Initial thermal noise creates both positive and negative values at the edge. These fields drive electron $\mathbf{E} \times \mathbf{B}$ drifts in the x -direction. Once established, these fields continue to drive electrons either towards or away from the boundary. The resulting electrostatic fields generated by the electron $(\mathbf{E} \times \mathbf{B})_x$ motion do not act to restore the electrons

back to a uniform density. Electrostatic effects tend to drag the ions towards the electrons rather than electrons towards ions.

This behavior continues to grow because apparently the simulation model does not prevent it. This behavior is not observed for the $\Phi = 0$ boundary conditions since this requires $E_y = 0$ at the edge. Thus there is not any $(\mathbf{E} \times \mathbf{B})_x$ electron motion at the boundary to drive the electrons either towards or away from the edge. This behavior disappears when the magnetic field is tilted with respect to the z -axis. The electron parallel flow in the simulation plane appears sufficient to prevent the accumulation of electrons at the edge.

Electron parallel currents can develop at the reflection boundaries after a fairly long period of time ($\omega_{pe}t = 40,000$) when such a tilt in the magnetic field exists. These currents flow in opposite directions at the two different boundaries. This current drives a magnetic field in the y -direction opposing the applied field. The source of this current is unknown. The energy conservation is not significantly degraded by this behavior.

When the magnetic field points entirely in the y -direction, $\theta = 90^\circ$, an instability develops in the bounded plasma. The $X - V_x$ phase space scatter plots of the electrons exhibited structures that appear unstable which drive electrons either towards or away from the boundary. The only driving term for these structures is the $(\mathbf{E} \times \mathbf{B})_x$ drift caused by the z -component of the transverse electric field. The x -motion of the electrons evidently generates an E_x to drive an $(\mathbf{E} \times \mathbf{B})_z$ drift. This electron $(\mathbf{E} \times \mathbf{B})_z$ drift couples back to E_z to further drive an instability. This behavior grows as time increases until the run goes completely unstable. This instability doesn't appear in the $2\frac{1}{2} D$ electrostatic models. The exact physical mechanisms that generate these modes are however not completely known.

This chapter will be completed with a few remarks on energy conservation. Except for the parallel instability described previously, total energy was well conserved for this simulation model. If there were not any external sources of energy (such as an antenna), the variation of the total system energy was smaller than 1% for times extending to $\omega_{pe}t = 90,000$. The energy conservation was generally comparable to the electrostatic codes with guiding center motion.

ALGORITHM

Initialization



A

Time Step Cycle



Accumulate charge density

$$\rho^{n+1/2} \text{ from } \mathbf{x}^{n+1/2}$$



Calculate longitudinal electric field

$$\nabla \cdot \mathbf{E}_L^{n+1/2} = 4\pi\rho^{n+1/2}$$



Backstep particle positions 1/2 time step

$$\mathbf{x}^n = \mathbf{x}^{n+1/2} - \mathbf{v}^n \Delta t/2$$

Accumulate current, number, and 2nd order current densities

$$\mathbf{J}^n, n^n, \langle \mathbf{v}\mathbf{v} \rangle^n \text{ from } \mathbf{x}^n, \mathbf{v}^n$$



Calculate magnetic fields

$$\nabla \times \mathbf{B}^n = \frac{4\pi}{c} \mathbf{J}_T^n$$



Calculate transverse electric fields

Use iterative procedure

$$\nabla^2 \mathbf{E}_T^n = \frac{4\pi}{c^2} \frac{\partial \mathbf{J}_T^n}{\partial t} \left[\mathbf{J}_A^n, \mathbf{J}_i^n, \mathbf{B}^n, n_e^n, n_i^n, \langle \mathbf{v}\mathbf{v} \rangle^n, \frac{\mathbf{E}_L^{n+1/2} + \mathbf{E}_L^{n-1/2}}{2}, \mathbf{E}_T^n \right]$$



Calculate \mathbf{E} and \mathbf{B} at the $n + 1/2$ time step

$$\mathbf{E}^{n+1/2} = \mathbf{E}_L^{n+1/2} + 3/2\mathbf{E}_T^n - 1/2\mathbf{E}_T^{n-1}$$

$$\mathbf{B}^{n+1/2} = 3/2\mathbf{B}^n - 1/2\mathbf{B}^{n-1}$$



Leap-frog ion velocities and positions

$$\frac{\mathbf{v}_i^{n+1} - \mathbf{v}_i^n}{\Delta t} = -\frac{e}{M} \mathbf{E}^{n+1/2} - \frac{e}{Mc} \frac{(\mathbf{v}_i^{n+1} + \mathbf{v}_i^n)}{2} \times \mathbf{B}^{n+1/2}$$

$$\mathbf{x}_i^{n+3/2} = \mathbf{x}_i^{n+1/2} + \mathbf{v}_i^{n+1} \Delta t$$



Leap-frog parallel electron velocity

$$\mathbf{v}_{e\parallel}^{n+1} = \mathbf{v}_{e\parallel}^n + \frac{e}{m} \mathbf{E}_{\parallel}^{n+1/2} \Delta t$$

Calculate predictor electron position

$$\mathbf{x}_e^{n+3/2}(\text{pred}) = \mathbf{x}_e^{n+1/2} + \mathbf{v}_{e\parallel}^{n+1} \Delta t - \mathbf{v}_{e\perp}^n \Delta t + \frac{2c}{B_0^2} \mathbf{E}^{n+1/2} \times \mathbf{B}_0 \Delta t$$



Calculate predicted charge density

$$\rho_{\text{pred}}^{n+3/2} \text{ from } \mathbf{x}_i^{n+3/2}, \mathbf{x}_e^{n+3/2}(\text{pred})$$



Calculate predicted \mathbf{E}_L

$$\nabla \cdot \mathbf{E}_{L(\text{pred})} = 4\pi \rho_{(\text{pred})}^{n+3/2}$$



Calculated predicted electron perpendicular velocity

$$\mathbf{E}_{T(\text{pred})}^{n+1} = 2\mathbf{E}_T^n - \mathbf{E}_T^{n-1}$$

$$\mathbf{v}_{e\perp}^{n+1}(\text{pred}) = \frac{c}{B_0^2} \left\{ \mathbf{E}_{T(\text{pred})}^{n+1} + \frac{[\mathbf{E}_{L(\text{pred})}^{n+3/2} + \mathbf{E}_{L}^{n+1/2}]}{2} \right\} \times \mathbf{B}_0$$



Backstep positions 1/2 time step

$$\mathbf{x}_i^{n+1} = \mathbf{x}_i^{n+3/2} - \mathbf{v}_i^{n+1} \Delta t / 2$$

$$\mathbf{x}_{e(\text{pred})}^{n+1} = \mathbf{x}_e^{n+3/2} - (\mathbf{v}_{e\perp}^{n+1}(\text{pred}) + \mathbf{v}_{e\parallel}^{n+1}) \Delta t / 2$$

Accumulate predicted current, number and 2nd order current densities

$$\mathbf{J}_p^{n+1}, n_p^{n+1}, \langle \mathbf{v}\mathbf{v} \rangle^{n+1}$$



Calculate predicted magnetic fields

$$\nabla \times \mathbf{B}_{\text{pred}}^{n+1} = \frac{4\pi}{c} \mathbf{J}_{T(\text{pred})}^{n+1}$$



Calculate predicted transverse electric field

$$\nabla^2 \mathbf{E}_{T(\text{pred})}^{n+1} = \frac{4\pi}{c^2} \frac{\partial}{\partial t} \mathbf{J}_T^{n+1} \left\{ \mathbf{J}_A^{n+1}, \mathbf{J}_i^{n+1}, \mathbf{B}_{(\text{pred})}^{n+1}, \right. \\ \left. n_e^{n+1}, n_i^{n+1}, \langle \mathbf{v}\mathbf{v} \rangle_{\text{pred}}^{n+1}, \frac{(\mathbf{E}_{L(\text{pred})}^{n+3/2} + \mathbf{E}_L^{n+1/2})}{2}, \mathbf{E}_{T(\text{pred})}^{n+1} \right\}$$



Corrector step for electron perpendicular velocities and positions

$$\mathbf{v}_{e\perp}^{n+1} = \frac{c}{B_0^2} \left\{ \mathbf{E}_{T(\text{pred})}^{n+1} + \frac{[\mathbf{E}_{L(\text{pred})}^{n+3/2} + \mathbf{E}_L^{n+1/2}]}{2} \right\} \times \mathbf{B}_0$$

$$\mathbf{x}_e^{n+3/2} = \mathbf{x}_e^{n+1/2} + (\mathbf{v}_{e\perp}^{n+1} + \mathbf{v}_{e\parallel}^{n+1}) \Delta t$$



Back to A

CHAPTER 3. EXCITATION OF KINETIC ALFVÉN WAVES AND ASSOCIATED PLASMA HEATING

3.1 Introduction

In this chapter, the computer model developed in Chapter 2 is applied to a problem of current interest in plasma physics, the heating of plasmas with radio frequency waves oscillating near the shear Alfvén resonance frequency. The behavior of a simulation plasma is examined in a number of computer experiments. A comprehensive modelling of the complex geometry, time scales, and full physical complications found in a laboratory experiment is beyond the scope of this work. Our goal is to point out important effects and explain the results in terms of simple physical concepts. The computer results may be important in a sense that they indicate those areas that may require closer examination in future theoretical and experimental work. The most important theoretical concepts applicable to the simulation problem are summarized in Sec. 3.2. In Sec. 3.3, we examine the behavior of the simplest system, a homogeneous plasma with periodic boundaries. The plasma responses to resonant and nonresonant excitations are analyzed. Section 3.4 further discusses the reaction of a driven homogeneous plasma in a system bounded in the x -direction. In the final section, 3.5, the plasma behavior is investigated when a nonuniform magnetic field introduces inhomogeneity to the bounded system.

3.2 Theoretical Survey

A brief synopsis of the principles involved with Alfvén wave resonance heating is given here. It is not our intention to present a detailed review of the important theoretical analyses. Instead we concentrate on those elements which are relevant to the simulation results.

To illustrate the important concepts of Alfvén wave resonance heating, we begin with the ideal magnetohydrodynamic (MHD) equations, which are

$$\rho \frac{d\mathbf{v}}{dt} = -\nabla p - \frac{1}{4\pi} \mathbf{B} \times (\nabla \times \mathbf{B}) \quad (3.1)$$

$$\frac{\partial \mathbf{B}}{\partial t} = \nabla \times (\mathbf{v} \times \mathbf{B}) \quad (3.2)$$

$$\frac{\partial \rho}{\partial t} + \nabla \cdot (\rho \mathbf{v}) = 0 \quad (3.3)$$

where ρ is the mass density, p is the pressure, and \mathbf{v} is the fluid velocity. The ideal MHD equations treat the plasma as a nonviscous, uniform, perfectly conducting fluid immersed in an ambient magnetic field. To close the set of equations, the adiabatic equation of state is used

$$p = \kappa \rho^\gamma. \quad (3.4)$$

Equations (3.1)-(3.4) are solved by examining perturbations of the physical variables about their equilibrium values. If the system is spatially uniform, these perturbations vary sinusoidally in space and time leading to the expansions

$$\mathbf{B} = \mathbf{B}_0 + \mathbf{B}_1 e^{-i\omega t} e^{i\mathbf{k} \cdot \mathbf{x}}$$

$$\rho = \rho_0 + \rho_1 e^{-i\omega t} e^{-i\mathbf{k} \cdot \mathbf{x}}$$

$$\mathbf{v} = \mathbf{v}_1 e^{-i\omega t} e^{i\mathbf{k} \cdot \mathbf{x}}.$$

The MHD equations and the equations of state are linearized by keeping only the first-order terms of the perturbed variables from which straightforward algebraic manipulation yields

$$\begin{aligned} (\omega^2 - k_{\parallel}^2 v_A^2) \mathbf{v} + [k_{\parallel} v_A^2 v_{\parallel} - (c_s^2 + v_A^2) (\mathbf{k} \cdot \mathbf{v})] \mathbf{k} \\ + (\mathbf{k} \cdot \mathbf{v}) k_{\parallel} v_A^2 \hat{\mathbf{b}} = 0 \end{aligned} \quad (3.5)$$

where $\hat{b} = \mathbf{B}_0/B_0$, $k_{\parallel} = \hat{b} \cdot \mathbf{k}$, $c_s = \gamma_p P_0/\rho_0$ is the plasma sound speed, and $v_A = B_0(4\pi\rho_0)^{-1/2}$ is the Alfvén velocity. There are three solutions to Eq. (3.5),

$$\omega_M^2(\pm) = \frac{k^2(v_A^2 + c_s^2)}{2} \pm \frac{1}{2} \left[k^4(c_s^2 + v_A^2)^2 - 4k_{\parallel}^2 k^2 v_A^2 c_s^2 \right]^{1/2} \quad (3.6)$$

$$\omega^2 = k_{\parallel}^2 v_A^2. \quad (3.7)$$

The plus sign in Eq. (3.6) yields the fast magnetosonic wave and the minus sign yields the slow magnetosonic wave. The solution in Eq. (3.7) is the shear Alfvén wave. The velocity perturbation and magnetic field perturbation of the shear Alfvén wave are both perpendicular to \mathbf{B}_0 . A central feature of the shear Alfvén wave is that it can only propagate along the magnetic field lines and does not involve a compression of the magnetic field.

In a nonuniform plasma, there exists a singularity in the MHD equations associated with the shear Alfvén wave. It was independently pointed out by Hasegawa and Chen⁴ and by Tataronis and Grossman⁵ that this singularity could be utilized to heat the plasma. Consider a slab model that is nonuniform in the x -direction. Let us assume solutions of the form

$$\mathbf{v} = \mathbf{v}(x)e^{-i\omega t} e^{i(k_y y + k_z z)}$$

where \mathbf{B}_0 lies in the z -direction. From Eqs. (3.1)-(3.4) the wave equation can be written⁴

$$\frac{d}{dx} \left[\frac{\varepsilon \alpha B^2}{\alpha B^2 k_{\perp}(x) - \varepsilon} \frac{dv_x}{dx} \right] - \varepsilon v_x = 0 \quad (3.8)$$

where

$$\varepsilon(x) = \omega^2 4\pi\rho(x) - k_{\parallel}^2(x) B^2(x)$$

$$\alpha(x) = 1 + \frac{\omega^2 c_s^2(x)}{v_A^2(x) [\omega^2 - k_{\parallel}^2 c_s^2(x)]}.$$

The singularity in the differential equation (3.8) occurs when $\varepsilon(x) = 0$. An electromagnetic wave with frequency ω will satisfy the resonance condition of a point x_s when $\omega = k_{\parallel}(x_s)v_A(x_s)$. There exists a continuous range of frequencies that satisfy the resonance condition bounded by $(k_{\parallel}v_A)_{\min}^2 < \omega^2 < (k_{\parallel}v_A)_{\max}^2$. If an external source of RF energy can excite a resonant wave at the singular point $x = x_s$, the singular property of the shear Alfvén wave permits the wave to propagate only along the magnetic field lines. Thus the wave energy accumulates at the resonance layer. Because of the existence of a continuous spectrum due to the singularity of the differential equation (3.8) at $\varepsilon(x) = 0$, the wave energy may be dissipated by “phase mixing” at the resonance layer. Moreover, as long as the plasma is not significantly perturbed from its equilibrium, the rate of energy transfer is independent of the actual dissipative processes (Grad⁶²).

The physical absorption mechanisms were studied by Hasegawa and Chen.^{10,11} Their work included electron inertia, finite ion gyroradius effects, collisions, Landau damping, and parametric processes for nonlinear absorption. The inclusion of kinetic effects changes the properties of the shear Alfvén wave, often termed the kinetic Alfvén wave, from the MHD solutions. The ions maintain their finite Larmor radius. A charge separation between the electrons and ions develop which generates significant longitudinal (electrostatic) electric fields. These longitudinal electric fields can be much larger than the transverse (inductive) electric fields associated with the kinetic Alfvén wave. For linear damping of the kinetic Alfvén wave, Hasegawa and Chen¹¹ examined the collisional mechanisms, ion viscous heating and electron Joule heating, and the collisionless mechanisms, ion and electron Landau damping.

In the particle simulation, we are interested in the behavior of

essentially collisionless plasmas. We therefore examine heating by Landau damping. The change in kinetic energy U in a volume V is given by

$$\frac{dU}{dt} = \frac{1}{2} \text{Re} \left[\int_v \mathbf{J}_e^* \cdot \mathbf{E} + \mathbf{J}_i^* \cdot \mathbf{E} dx \right]. \quad (3.9)$$

The first term on the right side of Eq. (3.8) is the electron absorption and the second term is the ion absorption. For our particle code model, only the motion parallel to the magnetic field can change energy for electrons. Thus finding the change in electron heating is given by

$$\frac{dU_e}{dt} = \frac{1}{2} \text{Re} \left[\int_v J_{e\parallel}^* E_{\parallel} dx \right], \quad (3.10)$$

which is the Landau damping term in the collisionless case. Assuming all variables have the dependence $\exp[i(\mathbf{k} \cdot \mathbf{x} - \omega t)]$, the linear solution to the electron drift kinetic equation, Eq. (2.40), is

$$f_{e1} = \frac{ie}{m(\omega - k_{\parallel} v_{\parallel})} E_{\parallel} \frac{\partial f_{e0}}{\partial v_{\parallel}}.$$

The parallel electron current is determined to be

$$J_{e\parallel} = -i \frac{n_0 e^2}{m} E_{\parallel} \int_v \frac{v_{\parallel}}{\omega - k_{\parallel} v_{\parallel}} \frac{df_{e0}}{dv_{\parallel}} dv_{\parallel} \quad (3.11)$$

where the integral is evaluated over the Landau contour. The integration of Eq. (3.11) for a Maxwellian distribution function yields

$$J_{e\parallel} = -i \frac{\omega_{pe}^2}{4\pi} z^2 E_{\parallel} \omega \left[1 - z e^{-z^2/2} \int_0^z e^{-\gamma^2/2} d\gamma + i \sqrt{\frac{\pi}{2}} z e^{-z^2/2} \right] \quad (3.12)$$

where

$$z = \frac{\omega}{k_{\parallel}} \sqrt{\frac{m}{T_e}} = \frac{\omega}{k_{\parallel} v_{Te}}.$$

The combination of Eq. (3.12) with Eq. (3.10) produces the following expression for the electron heating rate

$$\frac{dU_e}{dt} = \delta_e \frac{\omega_{pe}^2}{\omega} \int_v \frac{|E_{\parallel}|^2}{8\pi} dx \quad (3.13)$$

where

$$\delta_e = \sqrt{\frac{\pi}{2}} z^3 e^{-z^2/2}.$$

For comparison with the simulation results, a more convenient form is

$$\frac{d(\ln U_e)}{dt} = \frac{d(\ln T_e)}{dt} = \frac{\delta_e}{U_e} \frac{\omega_{pe}^2}{\omega} \int_v \frac{|E_{\parallel}|^2}{8\pi} dx. \quad (3.14)$$

The heating rate from Eq. (3.10) achieves its maximum value when $z = 1$. In the resonance region where $\omega = k_{\parallel} v_A$, this is equivalent to $v_{Te} = \omega/k_{\parallel} = v_A$. A calculation for the ion Landau damping rate¹¹ contains a similar exponential dependence with a term $e^{-v_A^2/2v_{Te}^2}$. The ion heating by Landau damping is therefore negligibly small for a low- β plasma. If the plasma β is smaller than 0.1, electron Landau damping is expected to dominate collisionless absorption processes.⁶

In an experimental device, such as a tokamak, an antenna located at the plasma edge launches an electromagnetic wave. The shear component of this wave is strongly damped at the edge. It is expected that the coupling to the Alfvén wave resonance region occurs through the weakly evanescent compressional component. The antenna configuration should be approximately the same shape as the resonance mode for maximum coupling. It has been pointed out by Stix⁶³ that for the wave to propagate across the density gradient from the antenna to the resonance region, either $\beta_e > 1$ or $\beta_i > 1$. If neither condition is satisfied, the kinetic Alfvén wave is better described by cold plasma equations and is reflected from the resonance region forming a surface mode. This result has been confirmed by the numerical results of Ross, Chen, and Mahajan.¹²

3.3 Driven Alfvén Waves in a Periodic, Uniform Plasma

Whenever investigating a complex problem, it is often instructive to begin with the simplest case in order to observe how additional com-

plexity affects the important features of the problem. Therefore we start with a homogeneous magnetized plasma slab in an unbounded system. The plasma behavior for an example when the wave generated by the antenna does not resonate with the plasma and for three examples when the antenna driven wave satisfies the Alfvén wave resonance conditions is investigated in this section. The nonresonant case displays weak coupling between the plasma and the antenna, while the resonant cases show strong coupling between the plasma and the excited wave. For the remainder of this work, the words longitudinal and transverse will always refer respectively to the curl-free and divergence-free components of the wave vector. The terms perpendicular and parallel will normally be with respect to the ambient magnetic field vector.

The simulation model is $2\frac{1}{2}$ dimensional (2 spatial and 3 velocity coordinates) and is periodic in both the x -direction and the y -direction. The z -direction is assumed to be ignorable. The external source in the shape of a short antenna is located at approximately the centerline of the x -direction. The antenna current flows in the z -direction preserving the charge neutrality of the antenna. A sinusoidal travelling wave is launched by an antenna current of the form

$$\mathbf{J}_A(\mathbf{x}) = J_A S(x - x_A) \sin(\omega_A t - k_A y) \hat{k} \quad (3.15)$$

where J_A , ω_A and k_A are the amplitude, frequency, and wavenumber of the antenna and where x_A is the x -coordinate of the antenna current sheet. Because of the periodicity of the y -direction, the antenna wavenumber k_A is restricted to be an integer multiple of the fundamental wavenumber of the grid in the y -direction. Finite size particle effects act to broaden the current sheet such that it effectively has a finite spatial structure in the x -direction.

The strength of the antenna is normalized in terms of a pa-

parameter W , the energy of the source integrated over the simulation volume divided by the initial thermal energy of all the particles in the simulation,

$$W = \frac{\int_v \frac{B_A^2 + E_A^2}{8\pi} dx}{\sum_{\substack{\text{all} \\ \text{particles}}} \frac{1}{2} m_{pj} v_j^2}. \quad (3.16)$$

The antenna fields \mathbf{B}_A and \mathbf{E}_a are calculated including the presence of the plasma assuming that the particles in the plasma have an effectively zero temperature. The antenna couples directly to the transverse electric field and the magnetic field. The pump strength W is less than 1% for the results presented in this section. The ambient magnetic field direction is constrained to lie in the $y - z$ plane. With θ is defined by $\theta = \tan^{-1}(B_y/B_z)$, the parallel wavenumber is given by $k_{\parallel} = k_y \sin \theta$. Thus the antenna launches a single coherent mode propagating obliquely to the magnetic field. For the results presented in this chapter, the condition $B_{0z} \gg B_{0y}$ will apply such that the angle θ is small. All of the results presented in this section were extracted from a system size $L_x \times L_y = 64\Delta \times 320\Delta$. The finite particle size is held fixed at $a_x \times a_y = 1.5\Delta \times 15\Delta$. The results are obtained from plasmas with equal ion and electron temperatures, $T_i = T_e$. There are an average of four electrons and four ions within one grid cell. The frequencies of the kinetic Alfvén wave spectrum are less than the ion cyclotron frequency in laboratory magnetic confinement experiments. To clearly separate the Alfvén wave resonance effects from ion cyclotron resonance effects, it is desirable to place the kinetic Alfvén wave resonance frequency well below the ion gyrofrequency. This places strict demands on the range of parameters in the present computer model. It should also be mentioned that without the present guiding-center electron algorithm, it would have been much more difficult to fulfill these constraints.

CASE 1 — Nonresonant

The first situation we examine does not match the frequency and wavenumber with any plasma resonance. For this nonresonant run, the plasma β is low, $\beta = 2.7 \times 10^{-4}$. An ion-to-electron mass ratio of $M/m = 1600$ is used with a time step of $\omega_{pe}\Delta t = 15.0$. The angle θ has the value $\theta = 3.1^\circ$. The oscillator frequency, $\omega_A = 2.9 \times 10^{-3}\omega_{pe}$, is below the ion cyclotron frequency, $\Omega_i = 8.3 \times 10^{-3}\omega_{pe}$, such that ion cyclotron resonance effects are not expected. The electron thermal velocity has the value $v_{Te} = 0.4\omega_{pe}\Delta$ and the $v_A = 1.0\omega_{pe}\Delta$. The ion Larmor radius has the value $\rho_i = 1.2\Delta$. The antenna wavenumber is given the fundamental value of the system, $k_A\Delta = 2\pi\Delta/L_y = 1.96 \times 10^{-2}$ and the antenna strength is $W = 8.6 \times 10^{-3}$. The parallel phase velocity of the wave is $(v_{ph})_{\parallel} \equiv \omega_A/(k_A \sin \theta) = 2.79\omega_{pe}\Delta$ which is significantly larger than the Alfvén speed. The plasma parameters chosen for this run are closest to the values near the edge of present toroidal experiments.

The contours of the magnetic and electric fields, B_x , B_y , and E_{Tz} directly generated by the antenna at time $\omega_{pe} = 0$ are shown in Fig. 3.1. The plasma temperature was effectively reduced to zero for these plots. The contour lines of an electric or magnetic field component shown in the figure represent constant values for that field component. The dominant wave patterns driven by the antenna are characterized by the antenna wavenumber in the y -direction and the grid fundamental wavenumber in the x -direction. The same field contours depicted in Fig. 3.1 from a thermal plasma with the parameters previously described are shown in Fig. 3.2 again at time $\omega_{pet} = 0$. Comparison of Figs. 3.1 and 3.2 show that the antenna wave is strongly represented in the thermal plasma. As the simulation progresses forward in time, the electric and magnetic fields directly driven by the antenna maintain

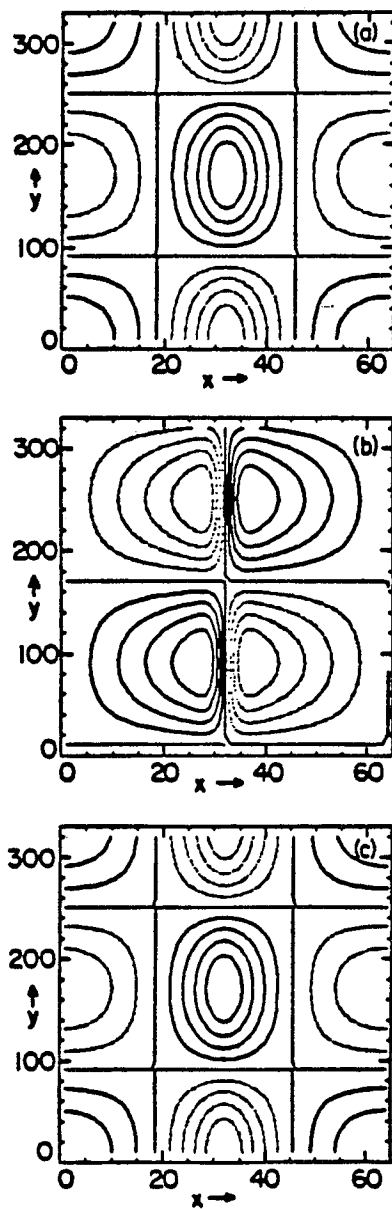


Figure 3.1. Contour plots of the fields a) B_z , b) B_y , and c) E_{Tz} generated by the antenna at $\omega_{pe}t = 0$ for a zero-temperature plasma in a doubly periodic system of size $L_x \times L_y = 64\Delta \times 320\Delta$.

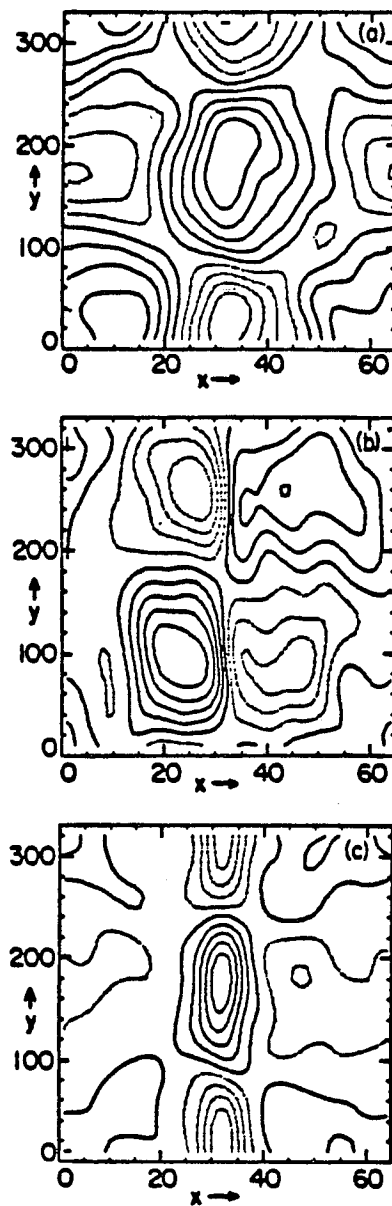


Figure 3.2. Contour plots of the fields a) B_z , b) B_y , and c) E_{Tx} for Case 1 of Sec. 3.3 at $\omega_{pe}t = 0$.

a standing wave pattern in the x -direction while propagating forward in the y -direction. Contour plots of the same electromagnetic field components shown earlier in Figs. 3.1 and 3.2 are depicted in Fig. 3.3 from a later time $\omega_{pet} = 13,000$ after having evolved six periods of the antenna wave. The wave fields driven by the antenna do not show any enhancement at a later time from their initial values in the plasma. Similar contours of the electrostatic fields E_{Lx} and E_{Ly} at the time $\omega_{pet} = 13,000$ shown in Fig. 3.4 do not show any significant influence from the antenna. Comparison of Figs. 3.2-3.4 indicate that the wave driven by the antenna couples weakly to the plasma. This view is further confirmed by the time evolution of the total electromagnetic field energy and the ion and electron kinetic energies portrayed in Fig. 3.5. The electromagnetic field energy and the total ion kinetic energy do not show an appreciable time averaged increase in value. However, both of these energies oscillate out of phase with each other suggesting that there is an energy exchange occurring between the ions and the electromagnetic fields. These oscillations have a frequency that is approximately twice the shear Alfvén resonance frequency for the antenna wavenumber. The electrons do not appear to participate in this energy exchange. The electrons have an average gain in kinetic energy of 2.5% which we will see is a small value.

CASE 2 — Resonant; $v_A > v_{Te}$

The first of the resonant cases we examine has the parallel phase velocity of the wave larger than the electron thermal velocity. The plasma β is again very low for this example with the value $\beta = 2.3 \times 10^{-4}$. According to the Stix criterion,⁶³ the kinetic Alfvén wave would not penetrate to the resonance region in a toroidal device for this parameter range. We nevertheless include this case for completeness. Other plasma parameters have the values: $M/m = 900$, $v_{Te} = 0.75\omega_{pe}\Delta$, $\Omega_i = 9.9 \times 10^{-3}\omega_{pe}$,

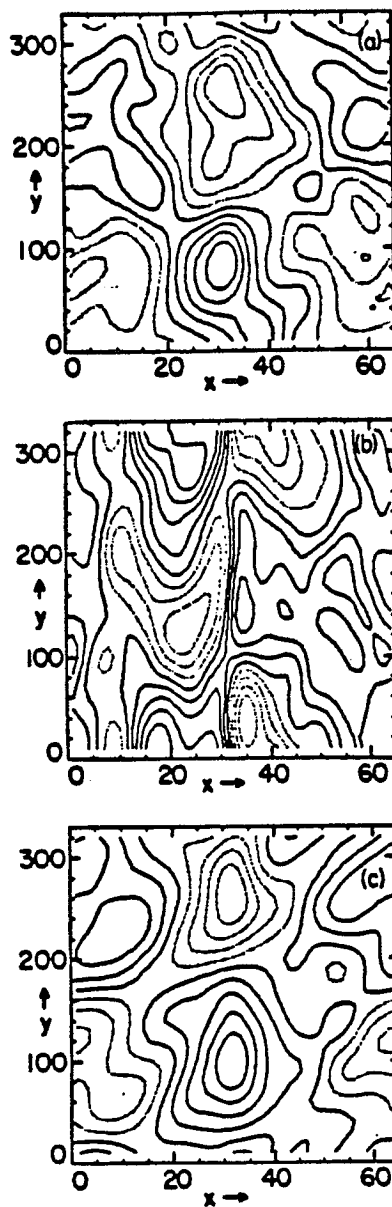


Figure 3.3. Contour plots of the fields a) B_x , b) B_y , and c) E_{Tx} for Case 1 of Sec. 3.3 at $\omega_{pe}t = 13000$.

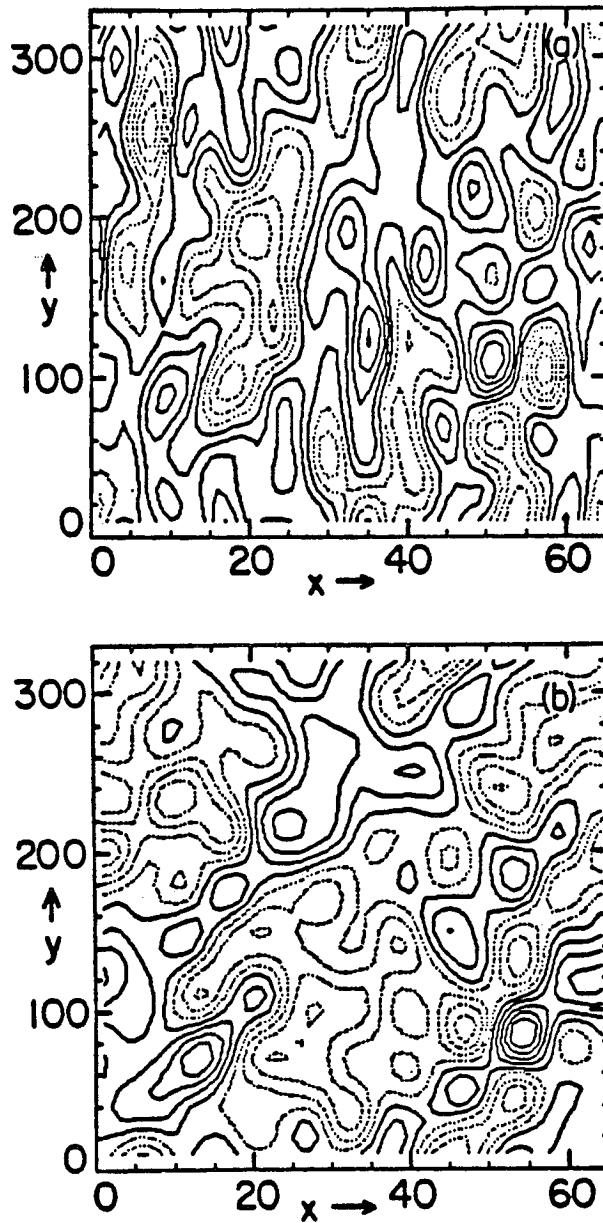


Figure 3.4. Contour plots of the fields a) E_{Lx} and b) E_{Ly} for Case 1 of Sec. 3.3 at $\omega_{pet} = 13000$.

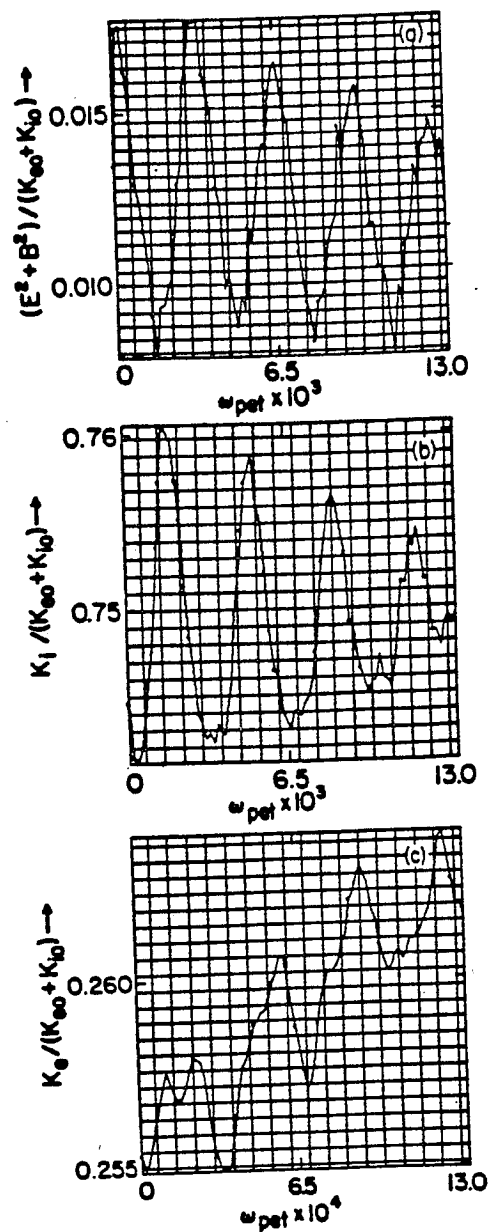


Figure 3.5. Time evolution of a) total electromagnetic field energies, b) total ion kinetic energies, and c) total electron kinetic energies ending at $\omega_{pet} = 13000$ for Case 1 of Sec. 3.3.

$\rho_i = 2.5\Delta$, $v_A = 2.67\omega_{pe}\Delta$, $\theta = 3.1^\circ$ and $\omega_{pe}\Delta t = 10$. The antenna parameters have the values: $\omega_A = 2.46 \times 10^{-3}\omega_{pe}$, $k_A\Delta = 1.96 \times 10^{-2}$, and $W = 6.8 \times 10^{-3}$. The antenna frequency is one-fourth of the ion cyclotron frequency so we do not expect any ion cyclotron resonance effects. The system is evolved to $\omega_{pe}t = 16,000$ which is 6.3 periods.

For this case, the initial electromagnetic field components, B_x , B_y and E_{Tz} , appear approximately the same as Fig. 3.2. These same fields at time $\omega_{pe}t = 6,000$, about 2.4 wave periods, have their contour lines displayed in Fig. 3.6. The dominant wave patterns remain the system fundamental in the x -direction and the antenna wavenumber in the y -direction. These contours indicate that the wave form a standing wave structure in the x -direction and propagate with the antenna current in the y -direction. The fields have an enhancement of a factor of two in amplitude above their initial values. The contours of the longitudinal electric fields at the same time are shown in Fig. 3.7 and they exhibit a coherent wave structure. The magnetic fields B_x and B_y are derivable from a single vector potential component A_z (since $\partial/\partial z = 0$) and the electrostatic fields are derivable from an electrostatic potential Φ . The wave propagating in Figs. 3.6 and 3.7 has the property that the electrostatic potential Φ has the same phase as the vector potential A_z . This wave has properties consistent with what is expected of the kinetic Alfvén wave.

The kinetic Alfvén wave that has been excited accelerates electrons in the parallel direction generating substantial currents in the plasma. These currents in turn significantly modify the wave fields. These currents appear to shift the wave to the left in the x -direction. As is shown in Fig. 3.8, by the completion of the ion, $\omega_{pe}t = 16,000$, the wave has moved to the left approximately 10Δ which is 16% of the system length. The wave is acting

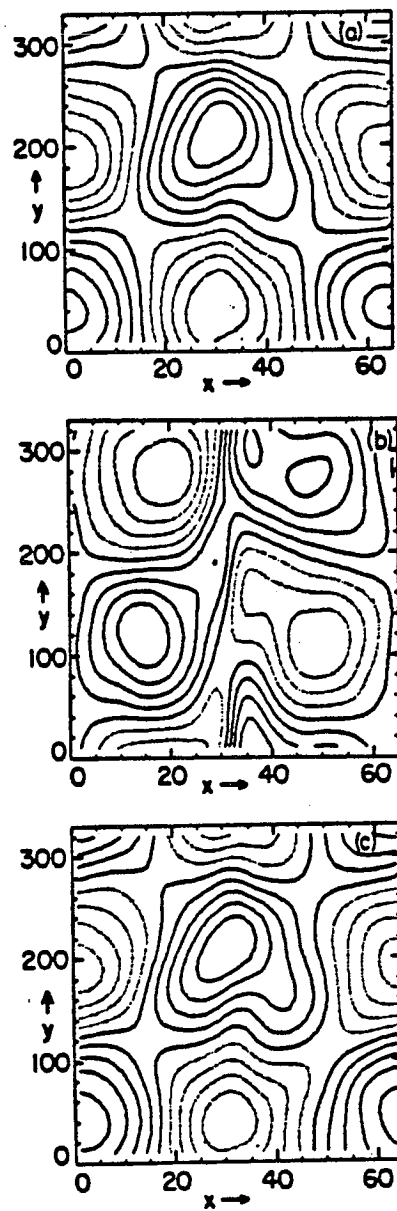


Figure 3.6. Contour plots of the fields a) B_x , b) B_y , and c) E_{Tz} for Case 2 of Sec. 3.3 at $\omega_{pet} = 6000$.

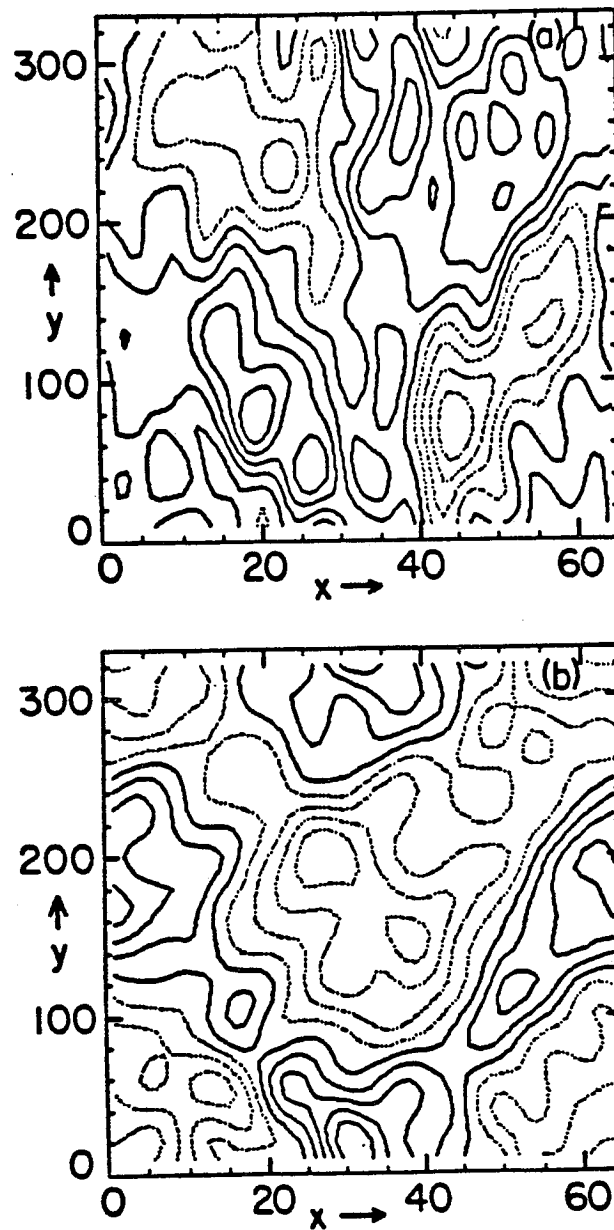


Figure 3.7. Contour plots of the fields a) E_{Lx} and b) E_{Ly} for Case 2 of Sec. 3.3 at $\omega_{pe}t = 6000$.

to trap electrons and accelerate them. The trapping creates an energetic tail on the electron velocity distribution function parallel to the magnetic fields, as is shown in Fig. 3.9. The spatial structure can be inferred from the $x - v_{\parallel}$ phase space scatter plots of the electrons in Fig. 3.10. The maximum trapping occurs near the antenna but is not symmetric about the antenna. It is stronger to the left of the antenna than to the right, probably explaining the shift of the wave fields. As is expected in trapping phenomena, the maximum velocity achieved by the electrons is almost exactly twice the parallel phase velocity of the wave, which is $2(v_{ph})_{\parallel} = 6.1v_{Te}$. As is seen from Fig. 3.11, there are large increases in the electron temperature. The heating is strongest near the antenna and appears spatially symmetric about the antenna position. There is a secondary maximum in the electron temperature at $L_x/2$ away from the x -coordinate of the antenna. The maximum electron temperature increase is about 640% above initial values. Noticeable levels of ion heating are observed but this will be discussed in the next resonant case.

The electromagnetic field energy reaches a maximum after approximately 3 periods as can be recognized from Fig. 3.12, eventually declining in magnitude. The initial field energy contains contributions from the thermal motion of the particles and directly from the antenna. The electromagnetic field energy increases as the plasma reacts to the antenna driven fields. The maximum increase in field energy is over 500% above the initial antenna contribution. There are again oscillations in the field energy whose frequency is approximately twice the antenna frequency. There are corresponding oscillations in the ion kinetic energy that are out of phase with the field energy oscillations indicating that energy is being exchanged between the electromagnetic fields and the ions. The kinetic energy gain of the electrons is about 160% while the kinetic energy gain of the ions is about

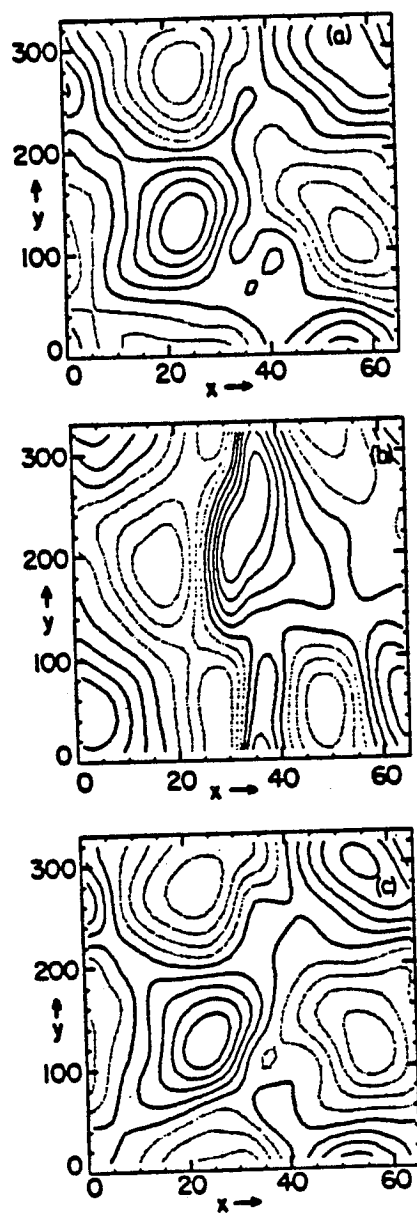


Figure 3.8. Contour plots of the fields a) B_z , b) B_y , and c) E_{Tz} for Case 2 of Sec. 3.3 at $\omega_{pe}t = 16000$.

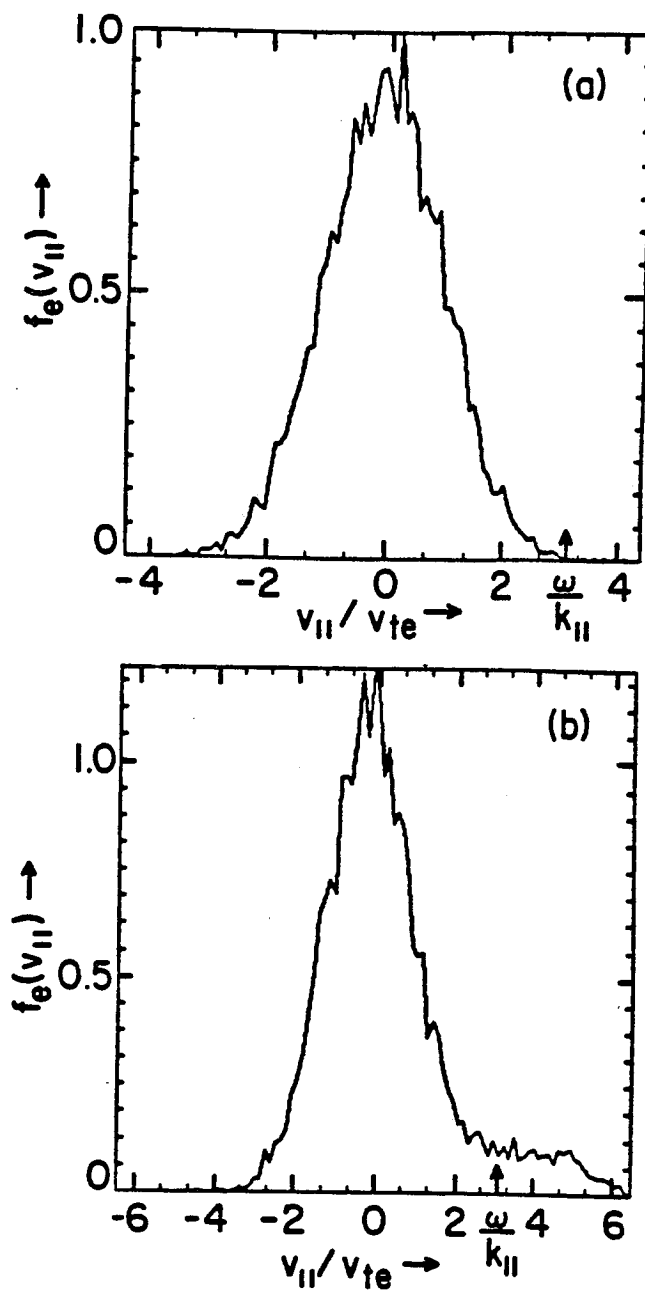


Figure 3.9. Electron velocity distribution function parallel to the magnetic field at a) $\omega_{pet} = 0$ and b) $\omega_{pet} = 16000$ for Case 2 of Sec. 3.3.

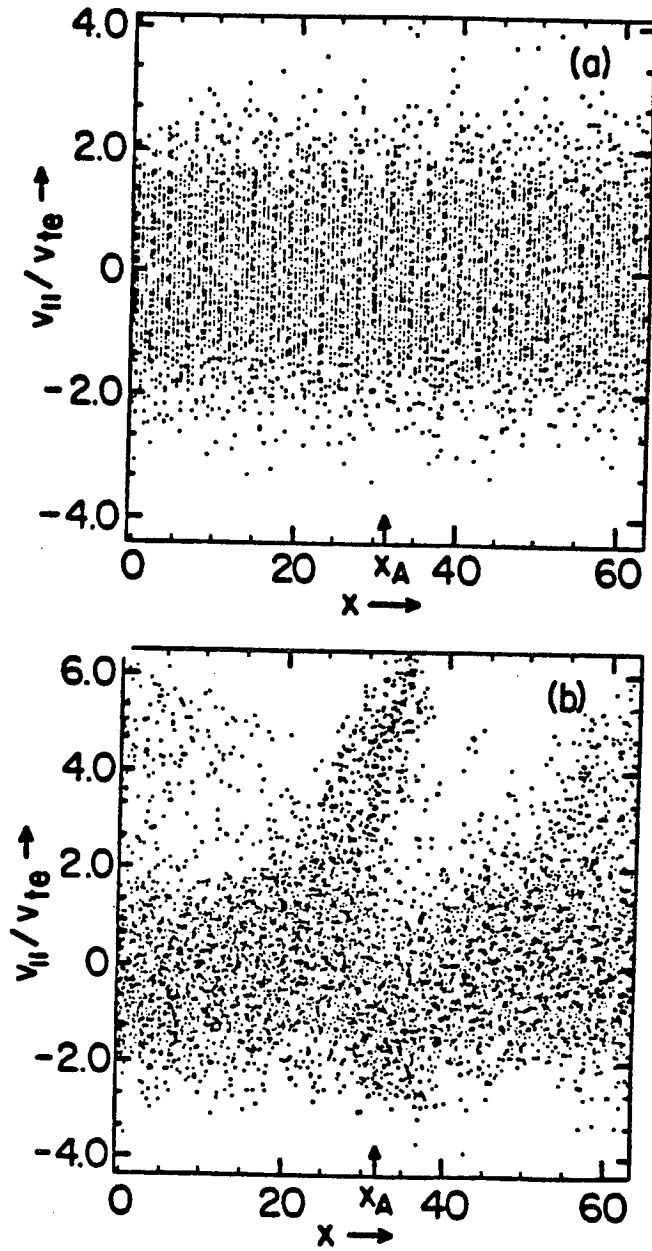


Figure 3.10. Phase space scatter plots, $x - v_{e||}$, of electrons at a) $\omega_{pe}t = 0$ and b) $\omega_{pe}t = 16000$ for Case 2 of Sec. 3.3.

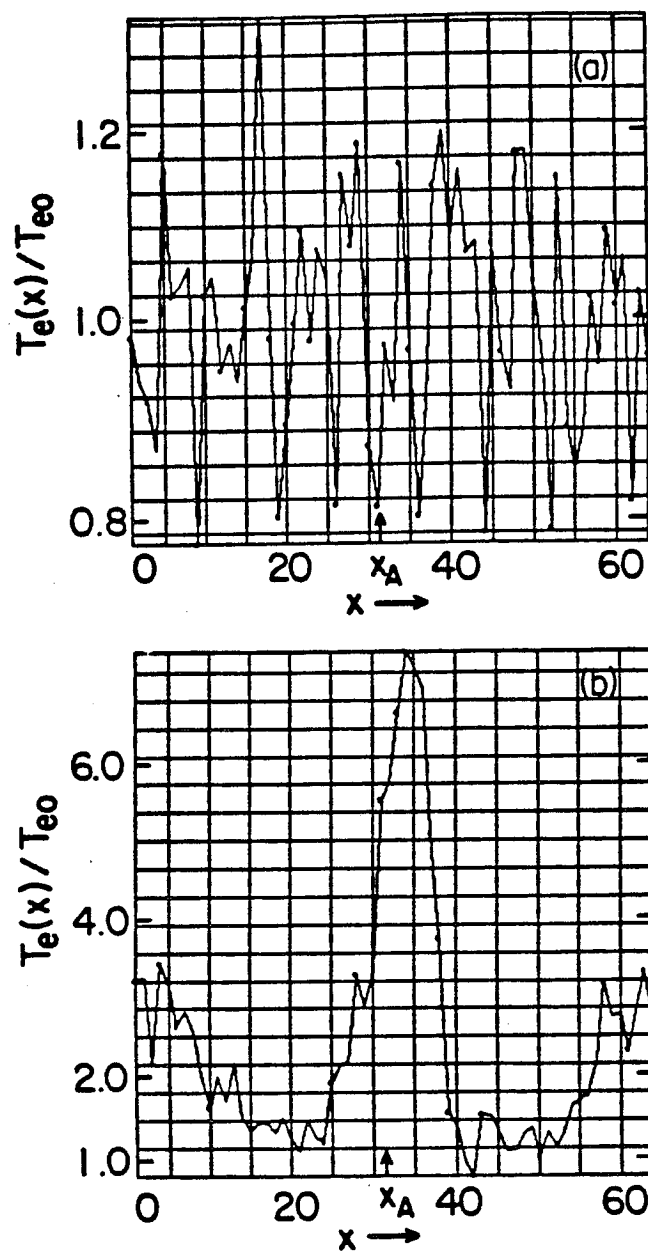


Figure 3.11. Spatial dependence of the electron temperature at a) $\omega_{pe}t = 0$ and b) $\omega_{pe}t = 16000$ for Case 2 of Sec. 3.3.

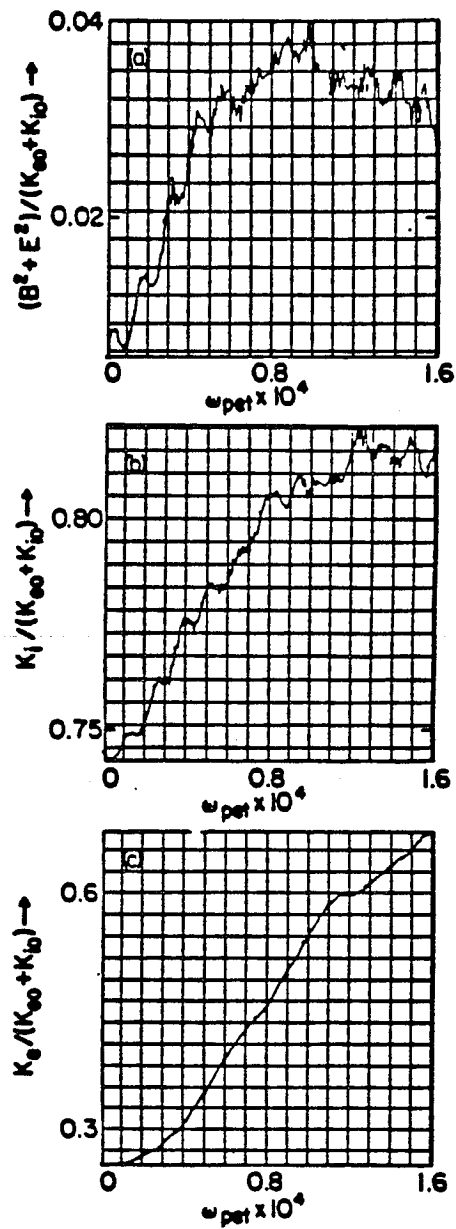


Figure 3.12. Time evolution of a) total electromagnetic field energies, b) total ion kinetic energies, and c) total electron kinetic energies ending at $\omega_{pe}t = 16000$ for Case 2 of Sec. 3.3.

10%. The wave interaction affects the electrons far more intensely than the ions. The trapping and acceleration of electrons leaves them with an average drift velocity $\langle v_D \rangle_e = 0.22\omega_{pe}\Delta$, which is approximately 30% of the initial electron thermal velocity. There is also a net parallel drift of the ions but its value is only 2% of the initial ion thermal velocity.

CASE 3 — Resonant; $v_A = v_{Te}$

For the next resonant case we shall examine the parallel phase velocity of the wave is equal to the electron thermal velocity. It is expected that this parameter range will maximize the collisionless electron heating. The plasma β for this case is higher than the two previous cases but is still fairly low with $\beta = 1.7 \times 10^{-3}$. This is a marginal case for wave penetration to the resonance region from the arguments presented by Stix.⁶³ The plasma parameters for this case are: $M/m = 1600$, $v_{Te} = 1.0\omega_{pe}\Delta$, $\Omega_i = 8.3 \times 10^{-3}\omega_{pe}$, $\rho_i = 3.0\Delta$, $v_A = 1.0\omega_{pe}\Delta$, $\theta = 3.1^\circ$ and $\omega_{pe}\Delta t = 15$. The antenna parameters have the values: $\omega_A = 1.08 \times 10^{-3}\omega_{pe}$, $k_A\Delta = 1.96 \times 10^{-2}$, and $W = 3.1 \times 10^{-3}$. The parallel phase velocity of the antenna driven wave is therefore $(v_{ph})_{\parallel} = 1.0\omega_{pe}\Delta$. The excitation frequency is almost a factor of 8 below the ion cyclotron frequency. The simulation ran to time $\omega_{pe}t = 36000$ which is approximately 6.2 periods of the antenna wave.

The contours of the initial magnetic fields at time $\omega_{pe}t = 0$ look approximately the same as Fig. 3.2. The initial E_{Tz} driven by the wave is obscured by the thermal plasma contribution. At a later time $\omega_{pe}t = 24000$, the kinetic Alfvén wave strongly establishes itself from the initial input wave as can be seen in Figs. 3.13 and 3.14. The amplitude of these fields components are at least a factor of four above their initial values. Particularly indicative of the kinetic Alfvén wave are the mode structures seen in the longitudinal electric fields, which are entirely due to the plasma

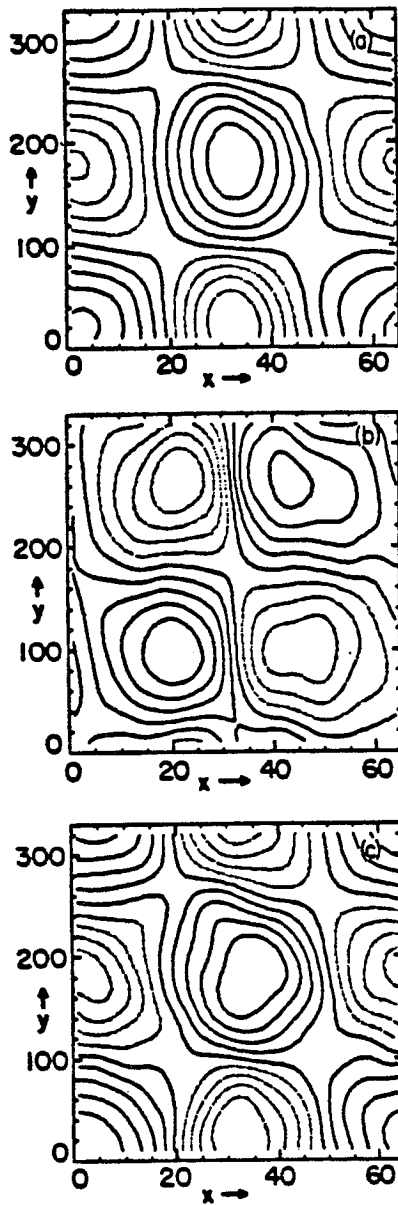


Figure 3.13. Contour plots of the fields a) B_x , b) B_y , and c) E_{Tx} for Case 3 of Sec. 3.3 at $\omega_{pe}t = 24000$.

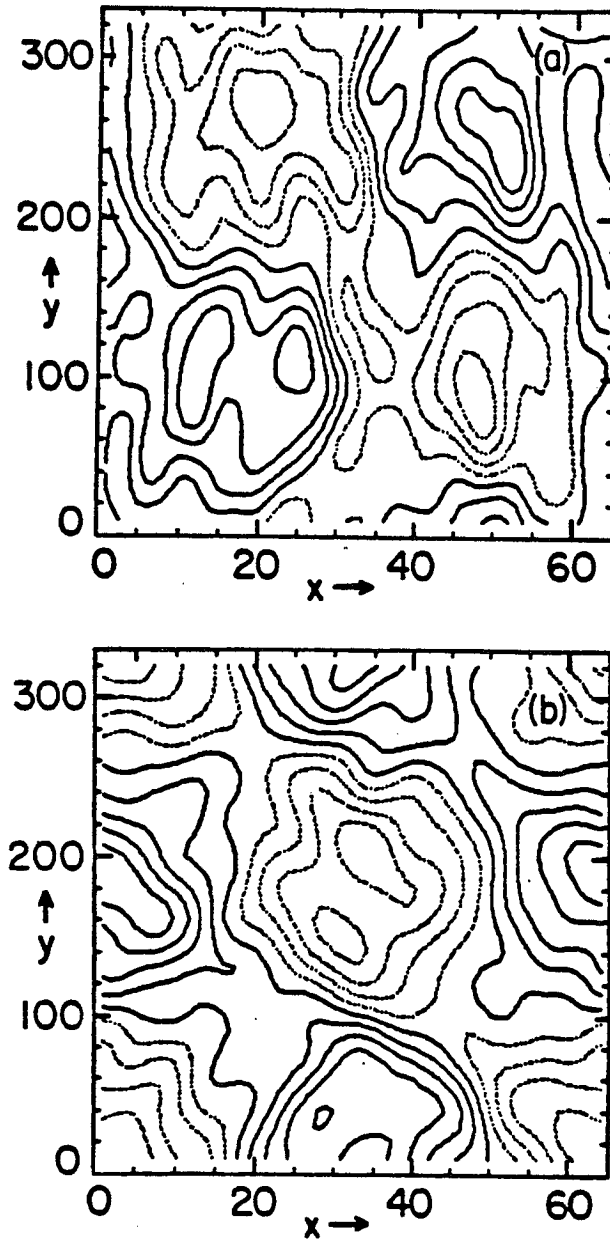


Figure 3.14. Contour plots of the fields a) E_{Lz} and b) E_{Ly} at $\omega_{pe}t = 24000$ for Case 3 of Sec. 3.3.

response, in Fig. 3.14. The wave patterns exhibit the same form as before, a standing wave in the x -direction and a travelling wave with the antenna in the y -direction. Again the wave mode structure is such that the electrostatic potential Φ is in phase with the vector potential A_z .

The wave significantly modifies the electron velocity distribution function parallel to the magnetic field as shown in Fig. 3.15. The velocity distribution function is flattened at the parallel phase velocity of the wave. The effect is so strong in this case, that in contrast to the initial Maxwellian shape peaked about $v_e = 0$, the distribution function at later times does not exhibit a peak in the range $-0.5 < v_e/(v_{Te}) < 1.5$. As expected, significant electron heating is observed. From Fig. 3.16, we see that the heating is spatially peaked near the antenna position with a secondary peak occurring approximately one-half of the system's length away. The peaks occur where the strongest electron fields, with parallel components, E_{Ly} and E_{Tz} are maximum. This information supports the conclusion that Landau damping is the mechanism heating electrons. The flattening of the electron distribution function localized to the neighborhood of the antenna is probably enhanced over that seen in Fig. 3.15 where the spatially (x, y) averaged distribution function is displayed. The maximum of the spatially localized electron temperature is 250% above its initial value at $\omega_{pe}t = 36000$.

There is also a substantial increase in the measured ion temperature. We introduce the terminology of separate ion temperatures associated with different ion velocity components. For example, the ion x -temperature T_{ix} is defined as

$$\frac{1}{2}T_{ix} = \frac{1}{2}M \sum_j^{\text{ions}} (v_{jx}^2 - \langle v_x \rangle^2)$$

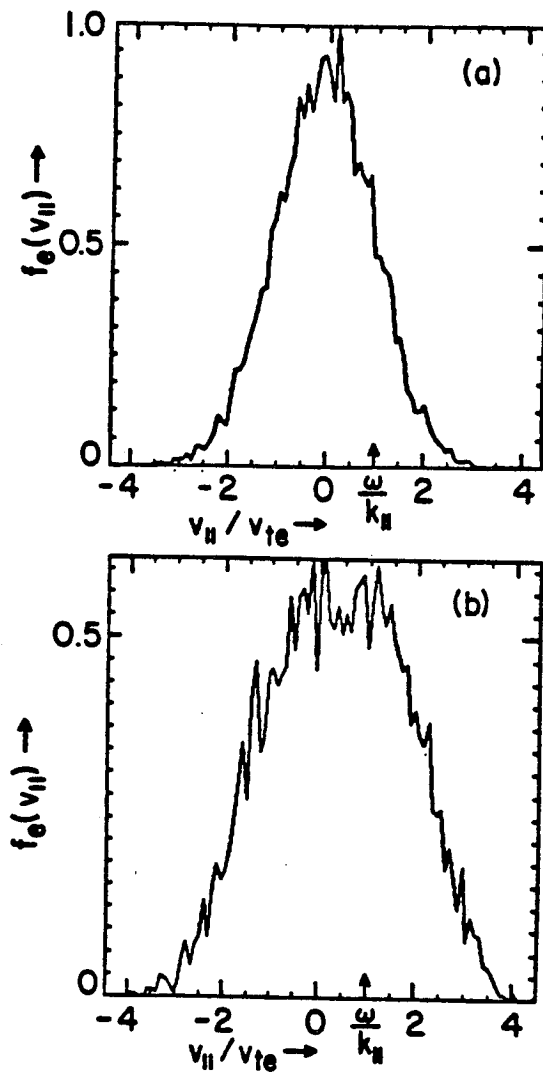


Figure 3.15. Electron velocity distribution function parallel to the magnetic field at a) $\omega_{pe}t = 0$ and b) $\omega_{pe}t = 36000$ for Case 3 of Sec. 3.3.

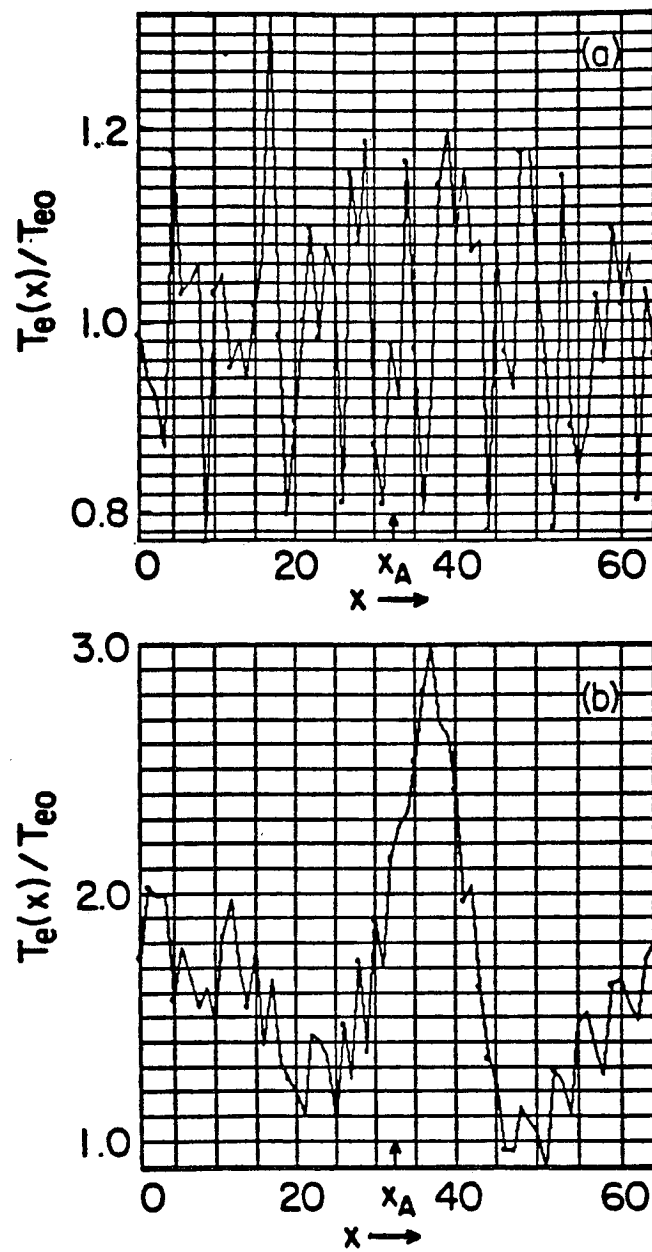


Figure 3.16. Spatial dependence of the electron temperature at a) $\omega_{pe}t = 0$ and b) $\omega_{pe}t = 24000$ for Case 3 of Sec. 3.3.

where

$$\langle v_x \rangle = \sum_j^{\text{ions}} v_{jx}.$$

Similar definitions apply to the temperatures T_{iy} and T_{iz} . We further define a perpendicular and parallel ion temperature based on those ion velocity components in the $y - z$ plane. Defining v_{\perp} and v_{\parallel} such that

$$v_{\perp} = v_y \cos \theta - v_z \sin \theta$$

$$v_{\parallel} = v_y \sin \theta + v_z \cos \theta.$$

We thereby define the ion temperatures $T_{i\perp}$ and $T_{i\parallel}$ as

$$\frac{1}{2}T_{i\perp} = \frac{1}{2}M \sum_j^{\text{ions}} (v_{j\perp}^2 - \langle v_{\perp} \rangle^2)$$

$$\frac{1}{2}T_{i\parallel} = \frac{1}{2}M \sum_j^{\text{ions}} (v_{j\parallel}^2 - \langle v_{\parallel} \rangle^2).$$

The spatial profiles of the ion y -temperature T_{iy} exhibit two peaks of roughly equal magnitude in Fig. 3.17 that are located on both sides of the antenna. These peaks occur approximately where the electron heating is at a minimum. The spatial profiles of the ion temperatures T_{ix} and T_{iz} do not display noticeable changes from their initial shapes. The recorded temperature increase is adequately explained as ion oscillation motion produced by the electric fields of the kinetic Alfvén wave. The wave electric fields couple to the ions via $\mathbf{E} \times \mathbf{B}$ motion. This agrees with the observation that the maxima of T_{iy} coincide with the biggest contour values of E_{Lx} , which is the largest of the wave electric fields. The values of the y -component of the electron $\mathbf{E} \times \mathbf{B}$ velocities are the same order of magnitude as the ion thermal velocity as shown in Fig. 3.18. The maximum of the $\mathbf{E} \times \mathbf{B}$ velocity is approximately $4 \times 10^{-2} \omega_{pe} \Delta$ compared with an ion thermal velocity of $2.5 \times 10^{-2} \omega_{pe} \Delta$.

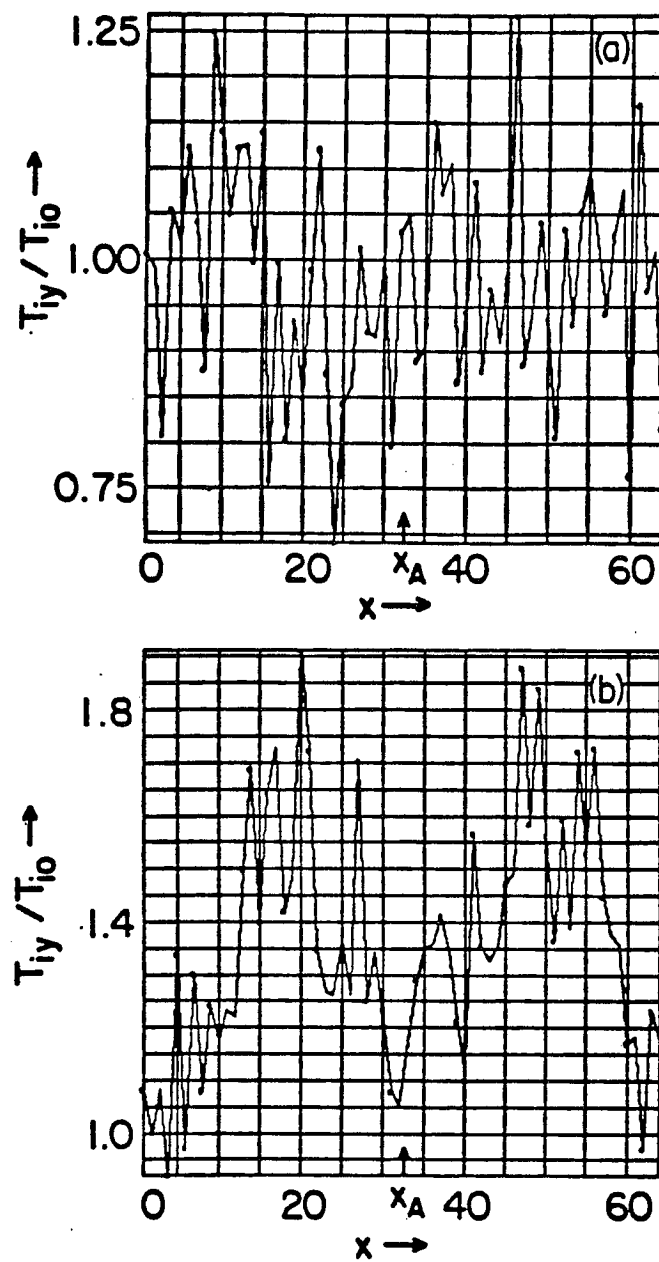


Figure 3.17. Spatial dependence of the ion y -temperature T_{iy} at a) $\omega_{pet} = 0$ and b) $\omega_{pet} = 24000$ for Case 3 of Sec. 3.3.

The temperature increase recorded by the simulation diagnostics does not represent a true increase in the thermalization of the ion motion. To get a true thermalization, some mechanism, such as collisionality, would have to interrupt the regularity of the motion effectively mixing the phase of the ion oscillation with respect to the wave oscillation.

The time evolution of the electromagnetic field energy depicted in Fig. 3.19 is enhanced over its initial values. The field energy increases by over a factor of seventy above the initial wave energy. The field energy increases over the first five periods before reaching a saturation level. There are again oscillations in the field energy which are out-of-phase with oscillations of the total ion kinetic energy. The frequency is double the frequency of the pump. The ions increase in kinetic energy by 21% over the length of the run appearing to saturate by the end of the run. In dimensionless units, the total field energy increases by 0.22 while the ions increase 0.15 indicating there is roughly an equal division of wave energy between the ions and the electromagnetic fields. The electron kinetic energy keeps increasing over the full length of the run. The electron energy increase is 0.26 which is 112% above the initial thermal value. The greatest share of the ion energy increase is seen in the ion temperature $T_{i\perp}$ and the remainder goes to T_{ix} . The ion parallel temperature does not appear to be affected by the kinetic Alfvén wave changing only 0.2% in value over the length of the run. The collisionless electron damping also generates an electron current. The net drift velocity of the electrons by the end of the run is $\langle v_{De} \rangle = .39$ which is 39% of the initial thermal velocity.

CASE 4 — Resonant; $v_A < v_{Te}$

The last resonant case examined in this section is characterized by an electron thermal velocity larger than the parallel phase velocity of the

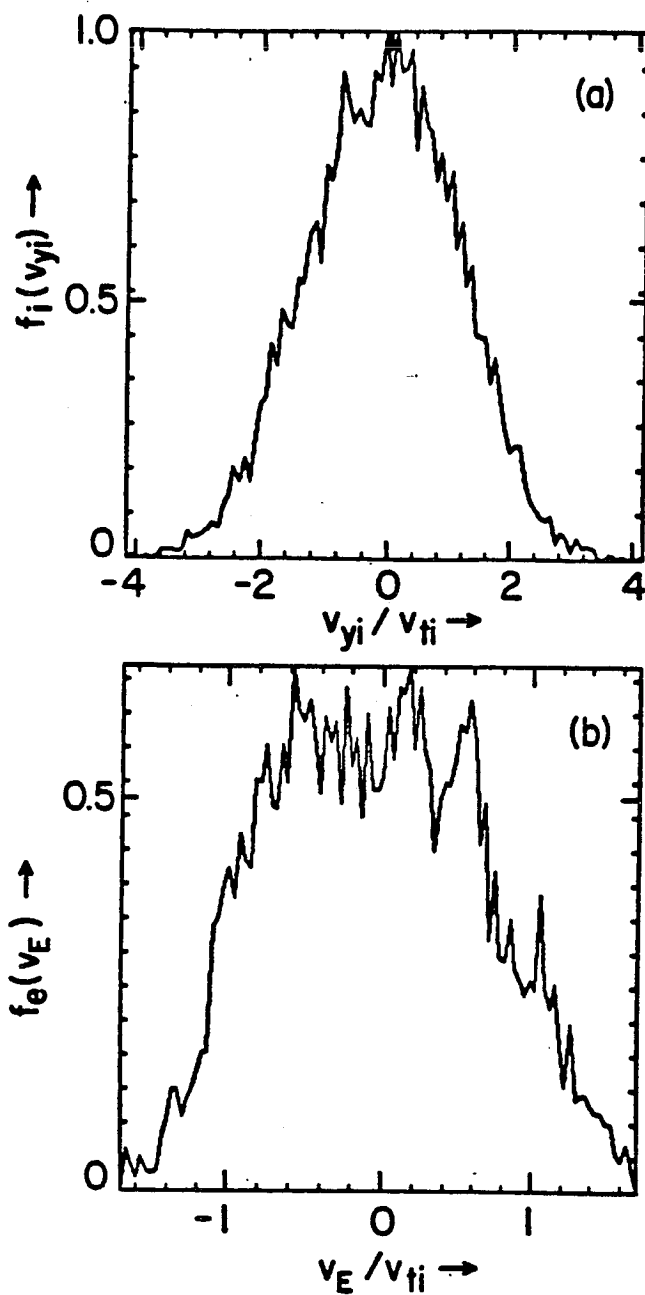


Figure 3.18. Distribution functions of a) y -component of the ion velocity and b) y -component of the electron $\mathbf{E} \times \mathbf{b}$ velocity at $\omega_{pe}t = 24000$ for Case 3 of Sec. 3.3.

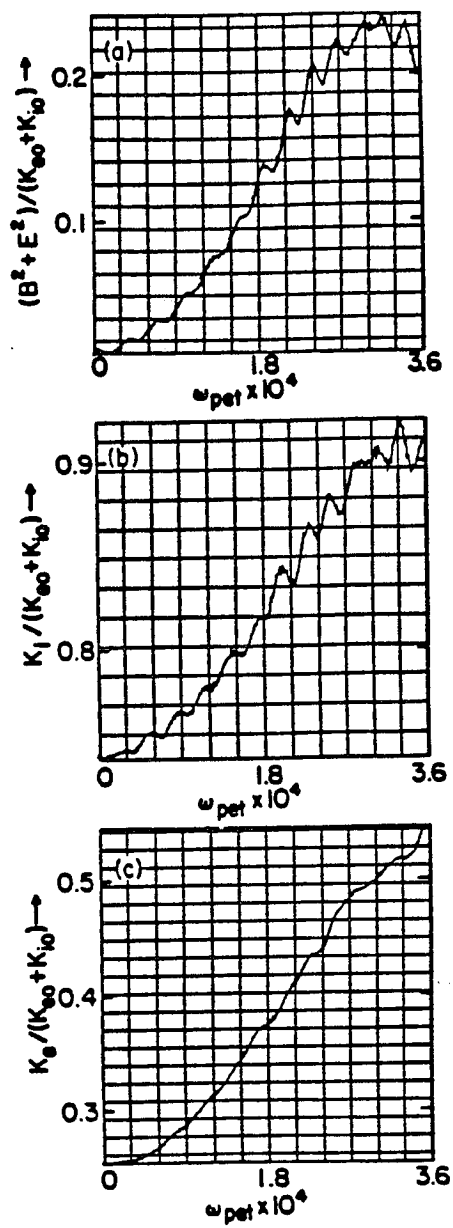


Figure 3.19. Time evolution of a) total electromagnetic field energies, b) total ion kinetic energies, and c) total electron kinetic energies ending at $\omega_{pet} = 36000$ for Case 3 of Sec. 3.3.

wave. This is the largest β case presented in this section with the value $\beta = 9.5 \times 10^{-3}$. This case satisfies the Stix criterion for wave penetration with $\beta M/m \simeq 9$. These parameters are probably closest to a toroidal device such as the PRETEXT or TCA tokamaks of the results presented here. The other plasma parameters for this run are: $M/m = 900$, $v_{Te} = 1.2\omega_{pe}\Delta$, $\Omega_i = 7.5 \times 10^{-3}\omega_{pe}$, $\rho_i = 5.4\Delta$, $\theta = 6.3^\circ$, and $\omega_{pe}\Delta t = 8.0$. The antenna parameters have the values $\omega_A = 1.44 \times 10^{-3}\omega_{pe}$, $k_A\Delta = 1.96 \times 10^{-2}$ and $W = 8.6 \times 10^{-3}$. The system is followed to time $\omega_{pet} = 24000$ which is 5.5 periods of the antenna. The parallel phase velocity of the wave is $(v_{ph})_{\parallel} = 0.67\omega_{pe}\Delta$ or $(v_{ph})_{\parallel}/v_{Te} = 0.56$. The heating efficiency of the electrons from Landau damping is expected to be somewhat less than the last case.

The wave structures of the electric and magnetic fields at time $\omega_{pe} = 12000$ in Figs. 3.20 and 3.21 form the familiar patterns of the kinetic Alfvén wave propagating in the y -direction and with a standing wave structure in the x -direction. At a later time however, $\omega_{pet} = 19200$, the contours of the wave fields have changed, as seen from Fig. 3.22. The phase fronts are at an oblique angle with respect to the y -axis rather than perpendicular to it. At this point in the simulation, both the particles and the electromagnetic fields are losing energy. This is the wave pattern that is formed when the system is giving energy back to the antenna rather than absorbing energy. By the end of the run of $\omega_{pet} = 24000$, the wave structure recovers its previous shape.

The electron energy loss can also be observed from the spatial profiles of the electron temperature depicted in Fig. 3.23. The temperature decline from $\omega_{pet} = 12000$ to $\omega_{pet} = 19200$ is most evident near the antenna position where the decrease is approximately 35% of the initial elec-

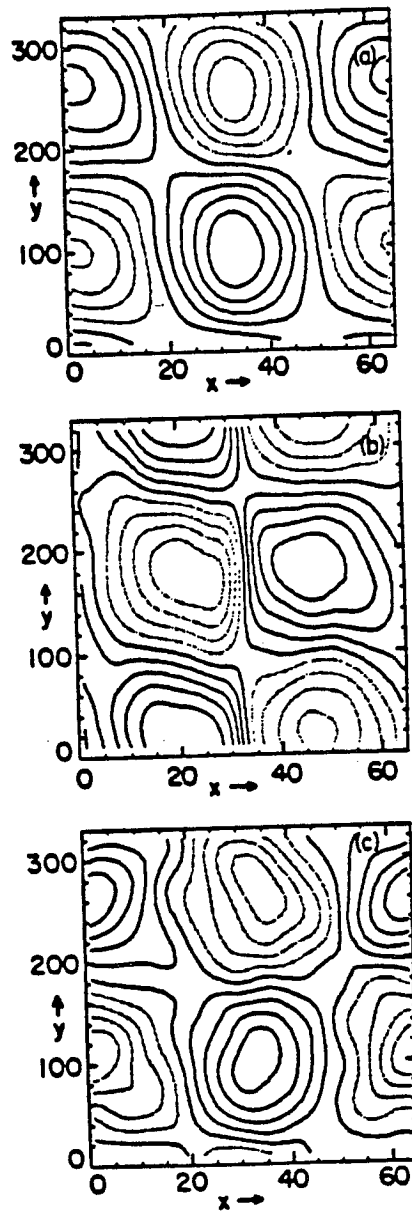


Figure 3.20. Contour plots of the fields a) B_x , b) B_y , and c) E_{Tz} at $\omega_{pe}t = 12000$ for Case 4 of Sec. 3.3.

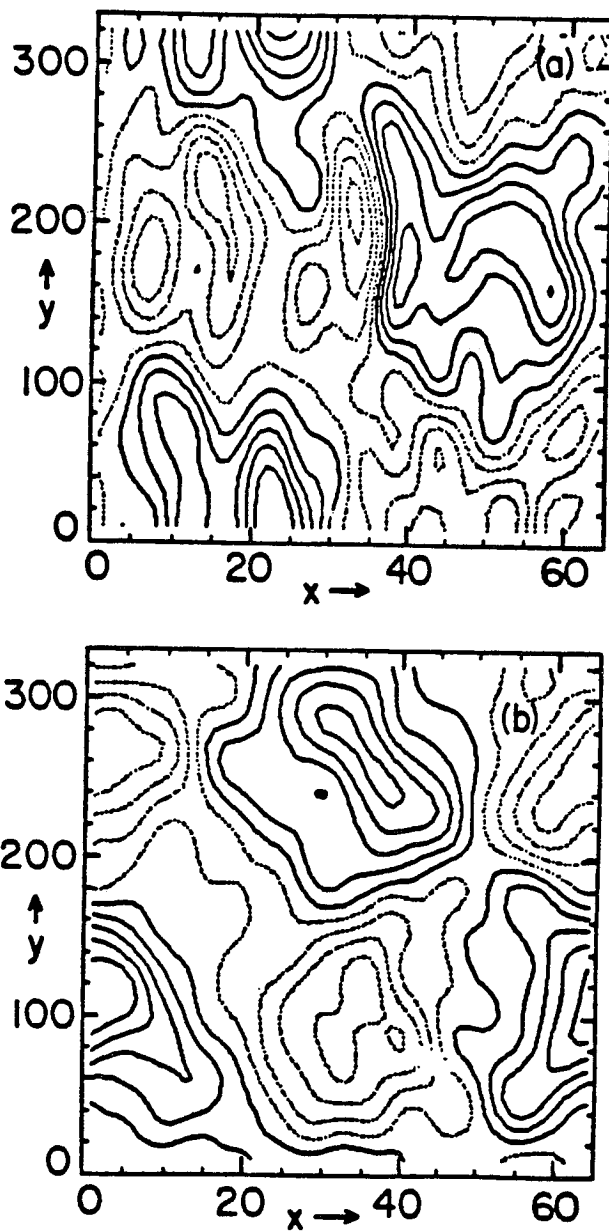


Figure 3.21. Contour plots of the fields a) E_{Lz} and b) E_{Ly} at $\omega_{pet} = 12000$ for Case 4 of Sec. 3.3.

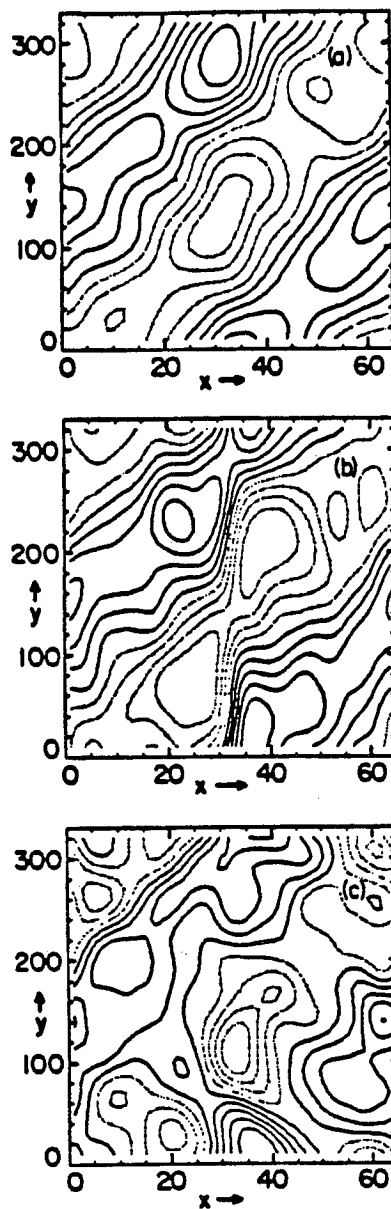


Figure 3.22. Contour plots of the fields a) B_z , b) B_y , and c) E_{Tz} at $\omega_{pet} = 19200$ for Case 4 of Sec. 3.3.

tron temperature. The whole electron temperature profile is flattened at the later time compared to its peak shape. The electron absorption again appears consistent with expectations from Landau damping. As can be observed from Fig. 3.24, the electron distribution is flattened at the parallel phase velocity of the wave at time $\omega_{pe}t = 12000$. By the end of the run, $\omega_{pe}t = 24000$, the peak of the distribution function has shifted towards that value. The ion temperature increases have the same qualitative behavior as seen in Case 3 and seem to be explained by $\mathbf{E} \times \mathbf{B}$ sloshing driven by the wave electric fields.

The total electromagnetic field energy reaches a saturation level quickly at $\omega_{pe}t = 10400$ after 2.3 wave periods, as seen from Fig. 3.28. The field energy then undergoes a subsequent decline to a minimum level approximately at $\omega_{pe}t = 19000$ and subsequently is increasing again by the completion of the run. The maximum gain of the field energy is about 12.5 times the initial antenna value. As seen in the previous cases, the field energy and the ion kinetic energies both oscillate out of phase with each other at twice the antenna frequency. The ion and electron kinetic energies increase or decrease when the total field energy increases or decreases. The maximum gain of the ion kinetic energy is about 10% above its initial value and the maximum gain of the electron kinetic energy is 31% above its initial value. The electrons are also driven in the direction of wave propagation. The strongest average drift speed the electrons achieve is $\langle v_{De} \rangle = .26\omega_{pe}\Delta$ which is about 18% of the initial thermal speed.

The qualitative behavior of Cases 3 and 4 indicate that the same basic physical processes account for the reaction of the plasma pump wave. The ion behavior is consistent with the explanation that the ion energy

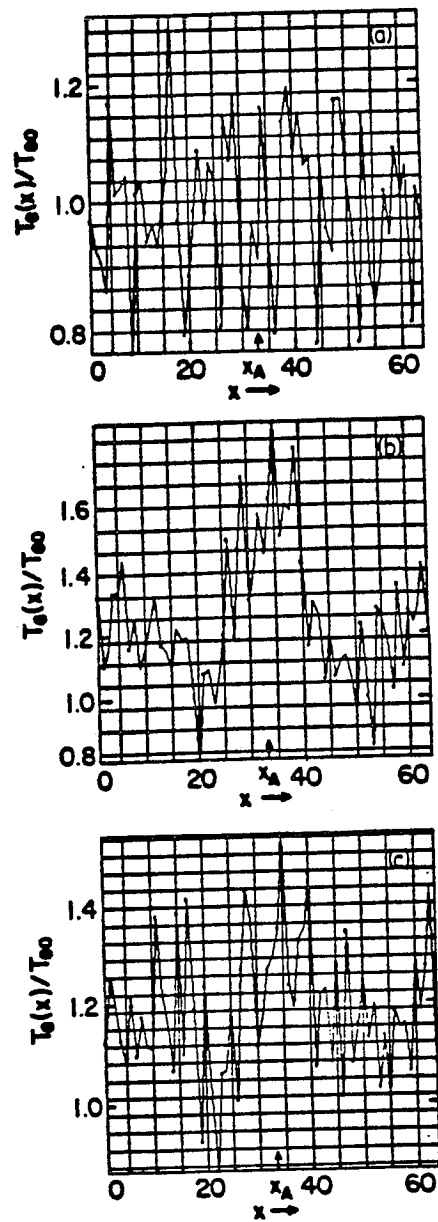


Figure 3.23. Spatial dependence of the electron temperature at a) $\omega_{pe}t = 0.0$, b) $\omega_{pe}t = 12000$ and c) $\omega_{pe}t = 19200$ for Case 4 of Sec. 3.3.

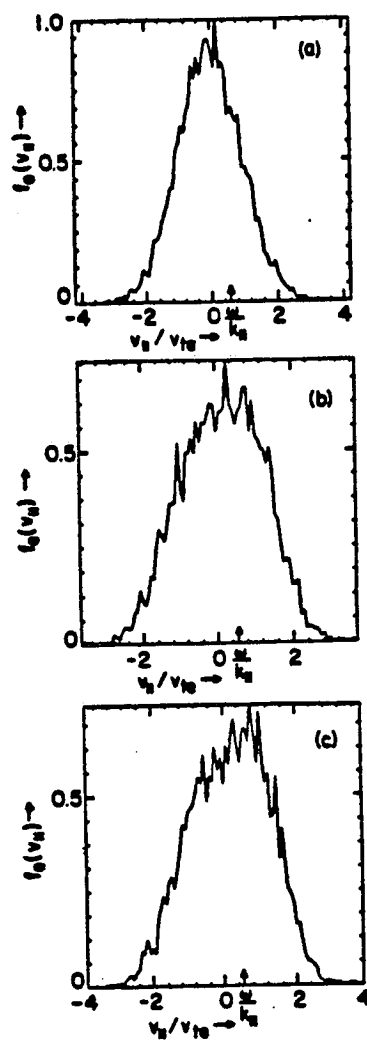


Figure 3.24. Electron velocity distribution function at times a) $\omega_{pe}t = 0.0$, b) $\omega_{pe}t = 12000$, and c) $\omega_{pe}t = 24000$ for Case 4 of Sec. 3.3.

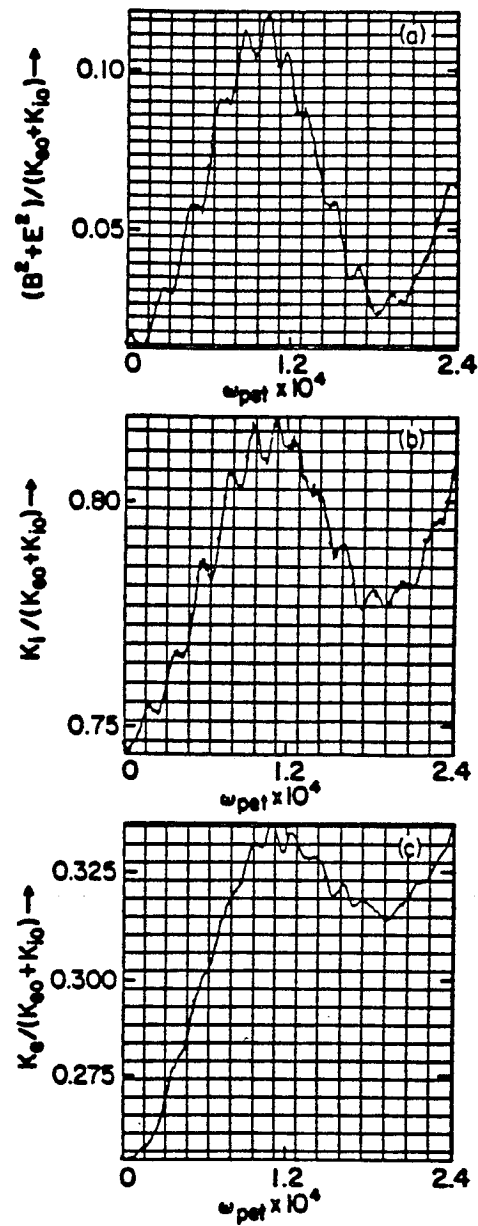


Figure 3.25. Time evolution of a) total electromagnetic field energies, b) total ion kinetic energies, and c) total electron kinetic energies ending at $\omega_{pet} = 24000$ for Case 4 of Sec. 3.3.

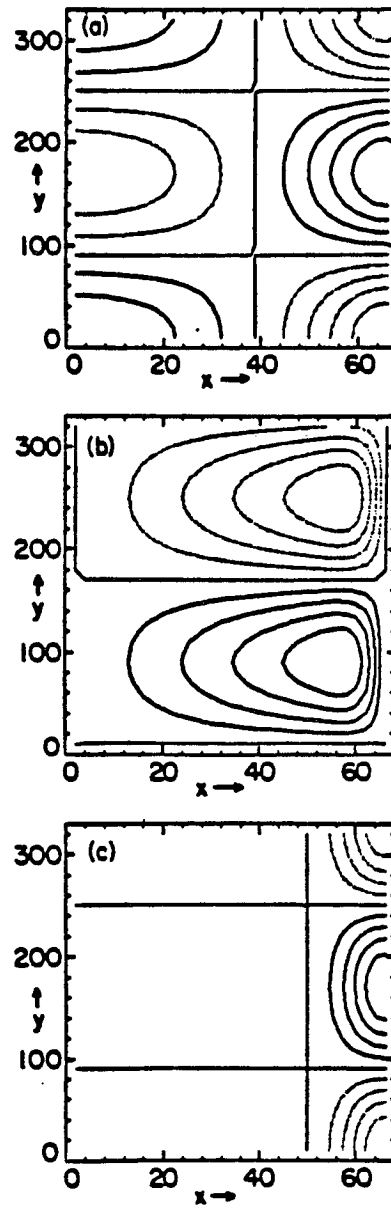


Figure 3.26. Contour plots of the fields a) B_z , b) B_y , and c) E_{Tz} generated by the antenna at $\omega_{pe}t = 0$ for a zero-temperature plasma in a system bounded in the x -direction of size $L_x \times L_y = 32\Delta \times 320\Delta$.

increase is caused by an $\mathbf{E} \times \mathbf{B}$ oscillation from the kinetic Alfvén wave electric fields. The electrons gain energy by collisionless damping of the wave. However, even though the normalized pump amplitude is larger in Case 4 than in Case 3, the plasma interaction is larger in Case 3. That is, the total and percentage gains of the electromagnetic field energy, total electron kinetic energy, total ion kinetic energy, and the net electron current are larger for Case 3 than for Case 4. This implies that the plasma resonates more forcefully if the parallel phase velocity of the kinetic Alfvén wave matches the electron thermal velocity compared with being smaller than the electron thermal velocity.

Simulation results of a plasma driven by an external source are presented from four different parameter regimes. In the first case, the antenna wavenumber and frequency do not match a plasma resonance. The simulation plasma exhibited weak coupling to the driven wave as a consequence. The antenna wavenumber and frequency matched the shear Alfvén resonance values for the three remaining cases. These three examples are primarily distinguished by differing values of the Alfvén speed with respect to the electron thermal speed. All three cases displayed strong interaction between the antenna driven wave and the plasma with the electromagnetic field energy increasing at least several times above the initial pump amplitude. Strong electrostatic electric fields characteristic of the kinetic Alfvén wave develop to accompany the inductive fields driven by the antenna. For Case 2 when $v_A \simeq 3v_{Te}$, electron trapping is the dominant process in the system. The electron distribution function develops a large nonthermal tail with a maximum speed equal to twice the parallel phase velocity of the driven wave. The last two cases exhibit flattening whose width is the order of the phase velocity of the electron distribution function about the parallel phase velocity

of the wave. The electron heating and currents are produced by collisionless absorption of the wave. An increase in the ion temperature is observed but may be true thermalization of the wave. This increase represents the portion of the total wave energy that resides in the ion motion.

3.4 Driven Alfvén Waves in a Bounded, Uniform Plasma

The changes introduced when boundaries in the x -direction are imposed on the simulation system are investigated for a homogeneous plasma in this section. The boundaries are placed at $x = 0$ and $x = L_x/2$, which is one-half the length of the periodic system. We are thereby transforming the left half of the periodic simulation into the bounded active region and consequently the right half into the bounded image region. The antenna is placed at the right boundary of the bounded system. The simulation plasma field patterns of the previous section, the appropriate boundary conditions require that B_y , B_z , and E_x have an odd symmetry about the boundaries and are thus zero at the boundaries. Similarly, B_x , E_y , and E_z have an even symmetry with respect the active and image systems. The particle reflection boundaries are placed 1.5 grid points inward from the symmetry boundaries and are reflected using the scheme mentioned in Sec. 2.5. For identical parameters, the bounded version requires approximately one-half the computer time used by the doubly periodic systems. Parameters appropriate to Cases 3 and 4 from the previous section are re-examined in this section. The input RF power is varied over a wide range to see how the wave absorption scales with power for the parameters from Case 3. The number of finite size particles per grid cell is also varied.

The ambient magnetic field and antenna configurations are the same as was presented in the previous section. The results presented in this section were obtained in a system whose size is $L_x \times L_y = 32\Delta \times 320\Delta$,

where L_x is now defined as the length of the active system in x -direction. One feature different from the previous section is that the antenna current is gradually increased from zero to full strength over one wave period. The antenna current given previously by Eq. (3.15) is replaced by

$$\mathbf{J}_A(t) = \alpha(t) J_A S(x - x_A) \sin(\omega_A t - k_{Ay}) \hat{k} \quad (3.16)$$

where

$$\alpha(t) = \begin{cases} \sin\left(\frac{\omega_A t}{4}\right) & t < \frac{2\pi}{\omega_A} \\ 0 & t > \frac{2\pi}{\omega_A} \end{cases}$$

The finite particle size is fixed at $a_x \times a_y = 1.5\Delta \times 15\Delta$, and the temperatures are equal, $T_i = T_e$.

CASE 1 — Resonant; $v_A = v_{Te}$

This is the same plasma parameter regime as Case 3 in the previous section. One example from the bounded system will be compared in detail with the corresponding ion from the doubly periodic simulation discussed in the previous section. The dependence of the plasma behavior on the collisionality of the simulation system is investigated by varying the number of finite size particles in a Debye cell. The increases in the ion and electron kinetic energies will be scaled with the input power. The examples used in these scalings have these common values for the plasma and antenna parameters: $\beta = 1.7 \times 10^{-3}$, $M/m = 1600$, $v_{Te} = 1.0\omega_{pe}\Delta$, $\Omega_i = 8.3 \times 10^{-3}\omega_{pe}$, $\rho_i = 3.0\Delta$, $\theta = 3.1^\circ$, $\omega_{pe}\Delta t = 15.0$, $\omega_A = 1.08 \times 10^{-3}\omega_{pe}$, and $k_A\Delta = 1.96 \times 10^{-2}$.

The particular example that will be compared with the doubly periodic case has an antenna strength given by $W = 3.9 \times 10^{-3}$. The run is followed to $\omega_{pe}t = 72000$, which is 12.4 periods. The contour plots of the

initial magnetic and transverse electric fields, B_x , B_y , and E_{Tz} , driven by the antenna in a plasma with a zero temperature are shown in Fig. 3.26. The dominant wave patterns are very similar to the left half of the doubly periodic system in Fig. 3.15. The pump electric field energy is concentrated in the region near the boundary with the antenna. At a later time, $\omega_{pe}t = 18000$, the wave electric and magnetic fields in Figs. 3.27 and 3.28 form a standing wave in the x -direction that is dominated by the wavenumber $k_x = \pi/L_x$ and a travelling wave in the y -direction with the antenna wavenumber and frequency. The wave fields seem to stay at approximately the same levels when the antenna current reaches its maximum strength after one antenna period. The parallel currents driven by the wave are weaker in the periodic system. Toward the end of the run, the net drift of the electrons actually becomes negative near the antenna edge opposing the travelling wave direction. The current spike of this nature has been previously noted in Sec. 2.8.

The electron distribution function for velocities parallel to \mathbf{B}_0 exhibits flattening around $v_e = (v_{ph})_{\parallel}$ in Fig. 3.29. However, the effects are far less dramatic than in Fig. 3.15 for the doubly periodic system. In the previous example, the electron velocity distribution function is level from $v_e = 0.0$ to $v_e = (v_{ph})_{\parallel}$ at time $\omega_{pe}t = 36000$ compared with the far weaker modification seen in Fig. 3.29 at $\omega_{pe}t = 72000$ for the bounded plasma. The spatial profiles of the electron temperature shown in Fig. 3.30 similarly display much weaker increases than were observed in the periodic case. The increases in the ion temperature are not even evident from the spatial profiles at this power level. When ion temperature profiles are examined at higher pump strengths, the heating is entirely perpendicular to the magnetic field and is largest near the boundaries. The ion x -temperature T_{ix} is larger

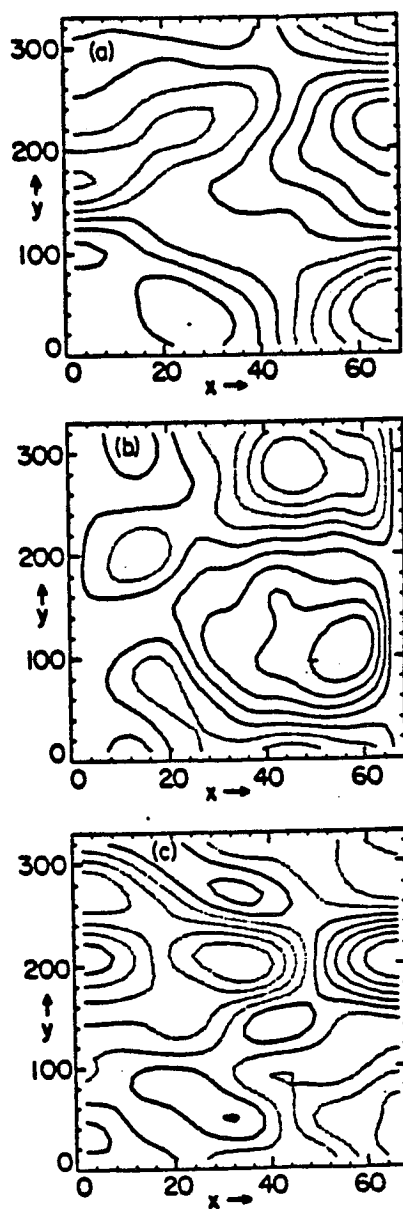


Figure 3.27. Contour plots of the fields a) B_x , b) B_y , and c) E_{Tz} at $\omega_{pe}t = 18000$ for Case 1 of Sec. 3.4.

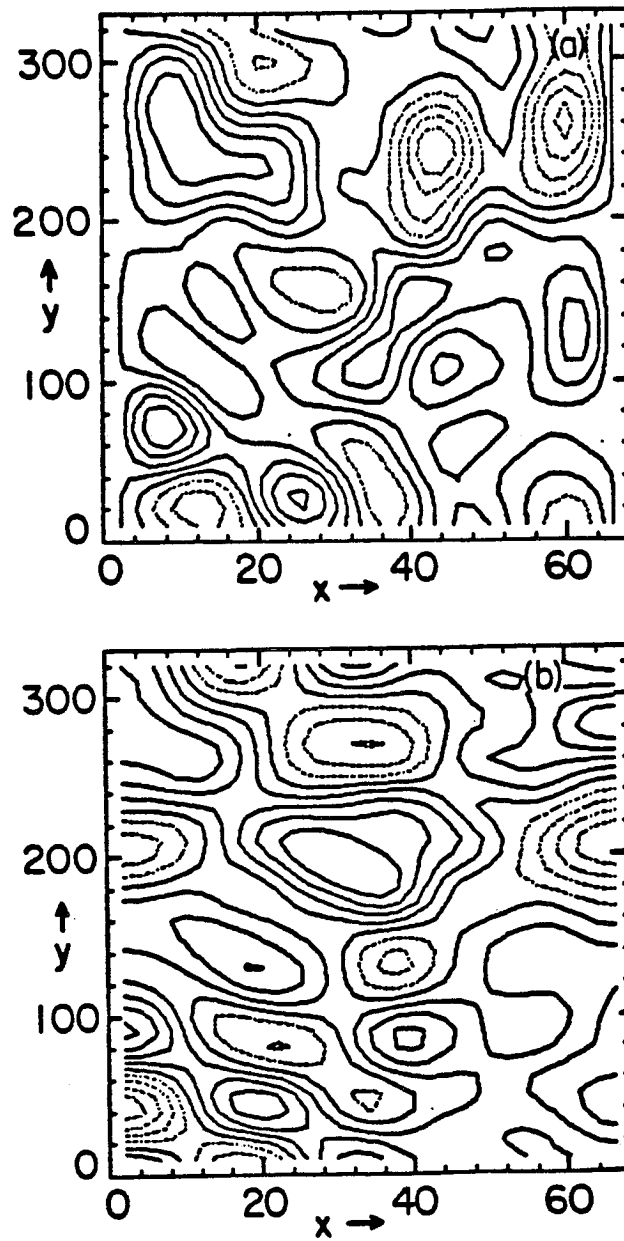


Figure 3.28. Contour plots of the fields a) E_{Lz} and b) E_{Ly} at $\omega_{pet} = 18000$ for Case 1 of Sec. 3.4.

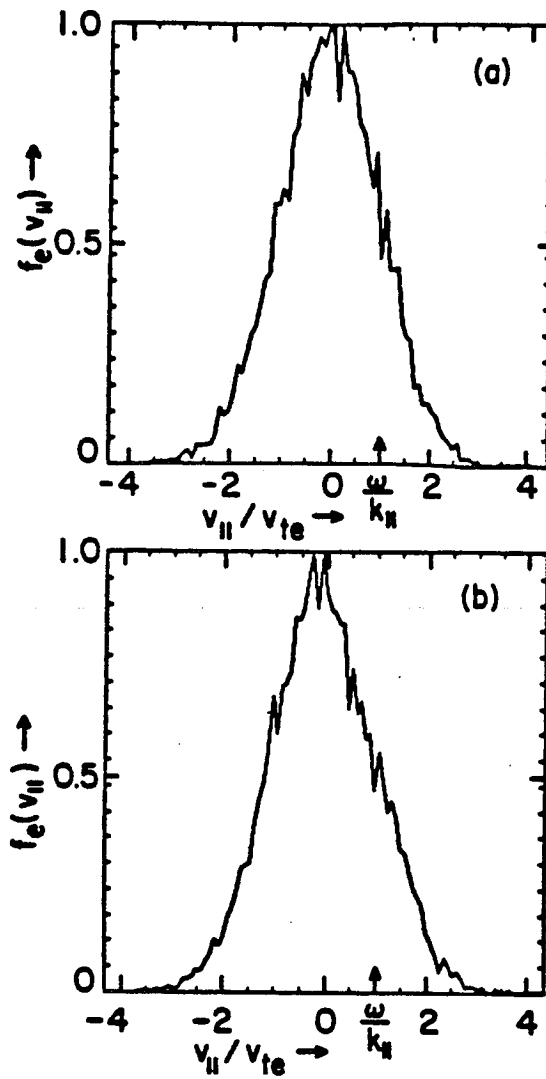


Figure 3.29. Electron velocity distribution function to the magnetic field at
 a) $\omega_{pe} = 0$ and b) $\omega_{pe} = 72000$ for Case 1 of Sec. 3.4.

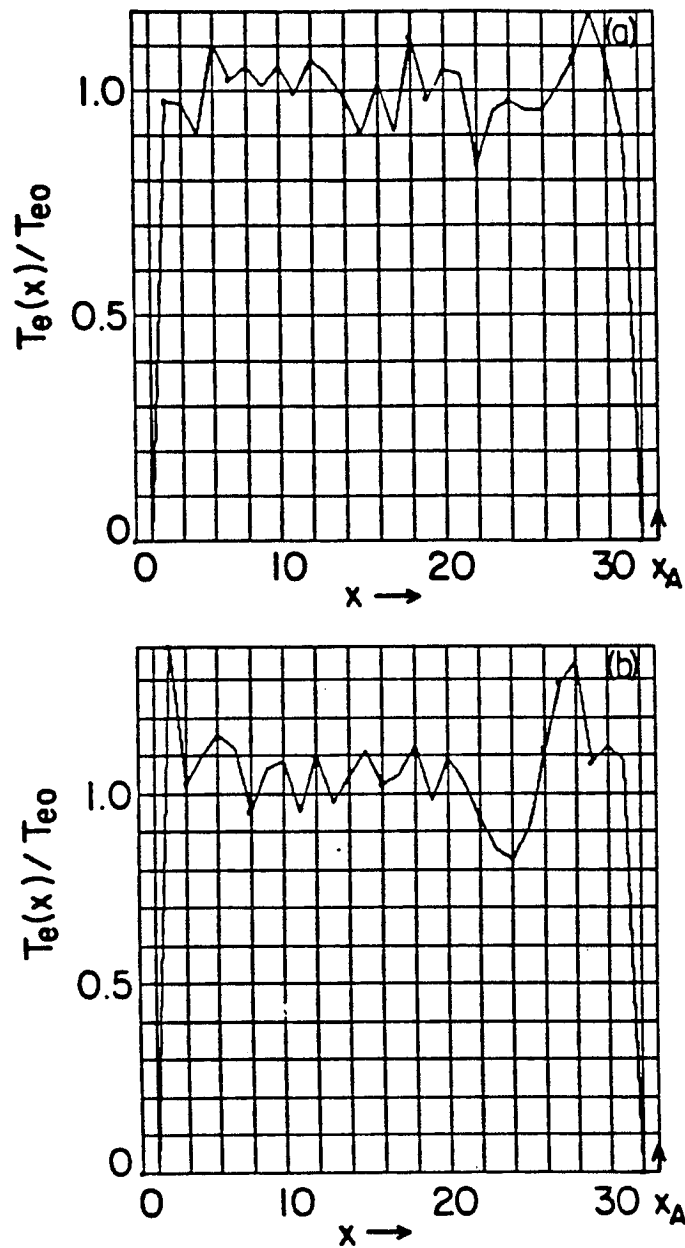


Figure 3.30. Spatial dependence of the electron temperature at a) $\omega_{pe}t = 0$ and b) $\omega_{pe}t = 72000$ for Case 1 of Sec. 3.4.

relative to T_{iy} than what occurred in the doubly-periodic system.

The time evolution of the electromagnetic field energies, total ion kinetic energy, and total electron kinetic energy is profiled in Fig. 3.31. The development of these energies is quite different from what was produced by the doubly periodic simulation plasma from Eq. 3.19. After the initial adiabatic increase of the pump strength, the electromagnetic field energy grows very little if at all. The ion kinetic energies and field energy no longer clearly evidence oscillations at twice the antenna frequency. The ions do not exchange energy with the wave fields in the same manner as described in the previous section. The ion kinetic energy increases linearly through the length of the run with the total increase being 2% above the initial thermal level. The electron kinetic energy sustains its largest increase from the end of the first period to the end of the second period whereupon it still increases but at a much less rapid rate. The total increase in the electron kinetic energy is 6.5% above the initial thermal levels. The total kinetic energy increase of each species is approximately the same. As before, the parallel temperature changes very little through the course of the run. However, T_{ix} and $T_{i\perp}$ increase by approximately the same amount, 3%, rather than $T_{i\perp}$ increasing more rapidly than T_{ix} did in the previous section.

The differences between the bounded and periodic systems indicate that there is some mechanism which impedes the growth of wave energy in the bounded plasma that is not present in the doubly periodic simulations. In the doubly periodic case, the wave field energy grew up to two orders of magnitude above its initial value. There are three effects that could inhibit the wave growth. The first is that the mode structure is more rigidly fixed by the boundary conditions. Requiring the wave fields to have either an odd or even symmetry about the antenna may remove some flexi-

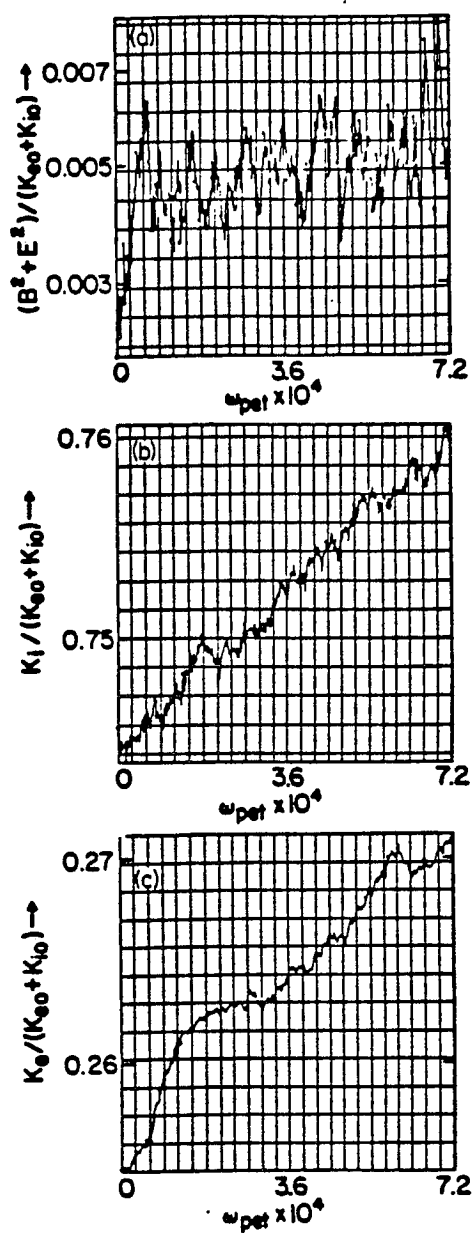


Figure 3.31. Time evolution of a) total electromagnetic field energies, b) total ion kinetic energies, and c) total electron kinetic energies ending at $\omega_{pet} = 72000$ for Case 1 of Sec. 3.4.

bility necessary for the enhancement of the wave electromagnetic fields above the levels directly produced by the antenna. Another factor that would slow wave growth is that particles are not allowed to move in the 1.5 grid points next to the boundaries in the x -direction, although it is probably not the primary reason wave growth is effectively stopped. The plots of the electromagnetic fields indicate however, that the particle interaction with the wave would be expected to be strongest there.

The last factor that may influence the kinetic Alfvén wave development is the particle reflection at the boundaries in the present bounded plasma model. The results from the doubly periodic example demonstrate that particle motion is influenced by the wave, particularly as seen by the increase of the ion energy from the $\mathbf{E} \times \mathbf{B}$ oscillations. When a particle is reflected from the boundaries, its new position and velocity will have a different phase with respect to the wave than what the particle had just prior to crossing the boundary. The particle reflections thus act to phase mix the particle motion with the wave. Since the wave fields are strong near the boundaries, this could prove to be a significant effect in inhibiting wave growth. This also provides an explanation why the ion perpendicular temperatures, T_{ix} and $T_{i\perp}$, are much closer in value than is recorded by the doubly periodic simulations. The phase mixing property of the ion reflections at the boundaries act as a thermalization mechanism in which the ion cyclotron motion equalizes T_{ix} and $T_{i\perp}$. The slowdown of the electron heating rate is probably due to the flattening of the electron velocity distribution function parallel to the magnetic field. This effect was overpowered by the continuing growth of wave energy in the doubly-periodic simulations. For the bounded simulation system, the wave energy remains at a fairly static level allowing the flattening of the electron velocity distribution function at

the parallel phase velocity of the wave to significantly slow the collisionless heating rate.

Several simulation runs were executed in this parameter regime varying the pump strength and quasi-particle number per cell. The bounded simulations have the advantages of being more economical and of reaching a saturation level more quickly than the doubly periodic simulations. Before the mechanism for the increase in ion energy was established, we endeavored to see how the wave interaction and particle dynamics are affected by collisions. The collisionality was varied by changing the average number of finite size particles per grid cell. The pump strength was varied from $W = 2.2 \times 10^{-3}$ to $W = 3.5 \times 10^{-2}$ covering a range of a factor of 16. The simulations were conducted with an average of either 4, 9, or 16 finite size particles per grid cells. From collisionless electron Landau damping and the ion wave oscillations, it is expected that the results do not depend on collisions and that increases in particle energies scale linearly with input power. This behavior is confirmed in Fig. 3.32, where the total electron and ion kinetic energy increases above initial thermal levels is scaled versus the pump strength W , also expressed as a percentage, after each simulation has evolved to $\omega_{pet} = 27000$, which is 4.6 wave periods. The electron energy increase remains linear through the power range. The ion energy increases somewhat faster than power at the strongest pump strengths. At the higher power levels, the wave electromagnetic field energy increases above the initial antenna values rather than remaining static as is seen at lower power. The nonlinear increase in the field energy for the higher pump strengths results in a corresponding nonlinear increase in the ion energy. For the electrons, the higher field energy is offset by the increased levelling of the electron velocity distribution function about the parallel wave phase velocity. As expected,

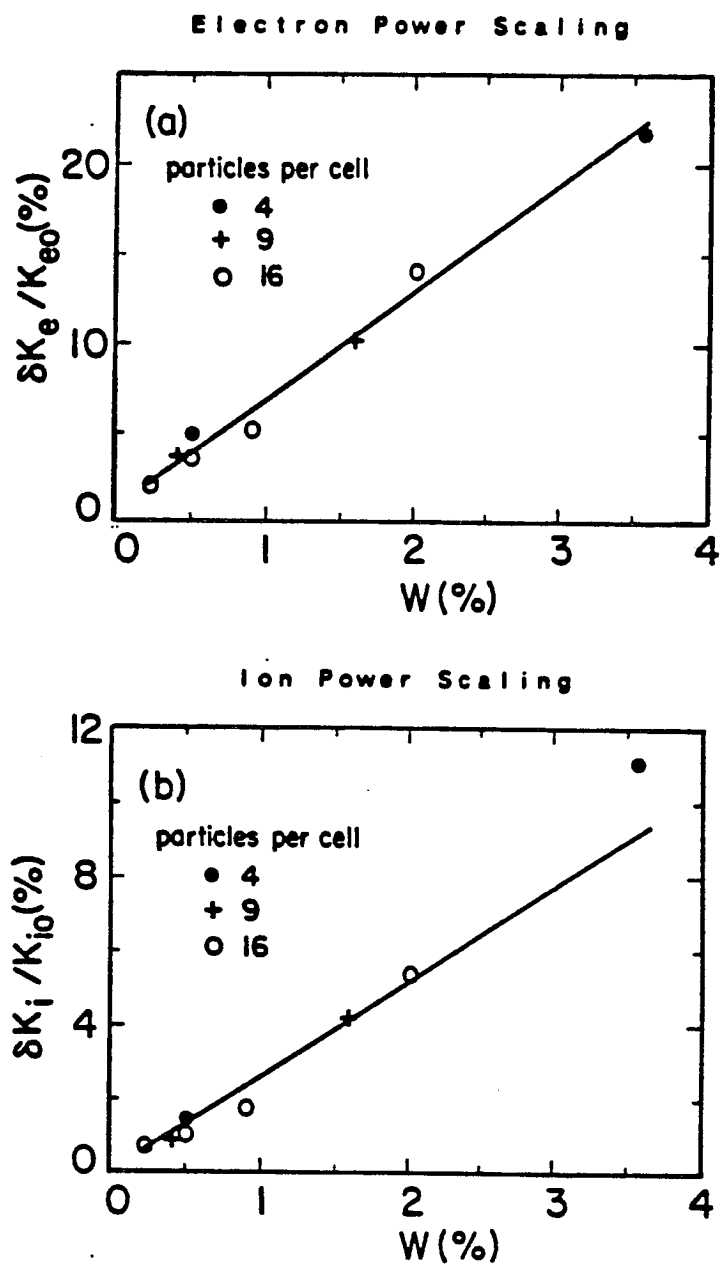


Figure 3.32. Dependence in the increase of the a) total electron kinetic energies and b) total ion kinetic energies on the antenna strength W at $\omega_{pet} = 27000$ for Case 1 of Sec. 3.4.

the collisionality does not appear to significantly affect the particle interaction with the excited kinetic Alfvén wave. The scalings of electron and ion kinetic energies with power are not changed when the number of particles per cell are changed. This view is reinforced when other features exhibit essentially the same behavior independent of the quasi-particle density.

CASE 2 — Resonant; $v_A < v_{Te}$

For the final examples in this section, the plasma behavior with boundaries is examined for the plasma parameters of Case 4 in the previous section. The plasma and antenna parameters for this simulation run are: $\beta = 9.5 \times 10^{-3}$, $M/m = 900$, $v_{Te} = 1.2\omega_{pe}\Delta$, $\Omega_i = 7.5 \times 10^{-3}\omega_{pe}$, $\rho_i = 5.4\Delta$, $\theta = 6.3^\circ$, $\omega_{pet} = 8.0$, $\omega_A = 1.44 \times 10^{-3}\omega_{pe}$, $k_A\Delta = 1.96 \times 10^{-2}$, and $W = 1.1 \times 10^{-2}$. The parallel phase velocity of the antenna driven wave has the value $(v_{ph})_{\parallel} = 0.56v_{Te}$. The antenna current was adiabatically increased over one pump period. The plasma was followed to $\omega_{pet} = 26,400$ which is 6 pump periods. The contours of the wave electromagnetic fields assume their expected shape, however, the electromagnetic field energy does not significantly increase after the first period when the antenna current reaches its maximum value. As seen from Fig. 3.33, the electron heating increases most rapidly during the first two periods after which it increases more slowly. The electron temperature increases 3.3% through the length of the run. The electron velocity distribution function displays modification about the parallel phase velocity of the wave at a level far weaker than is seen in the doubly periodic case. The ion energy increases 1.17% above thermal levels with the increase equally split between T_{ix} and $T_{i\perp}$. In the previous section the increase is concentrated in $T_{i\perp}$. The effects of the boundaries under these conditions are approximately the same as for Case 1. The boundary conditions inhibit wave growth above the levels directly generated by the

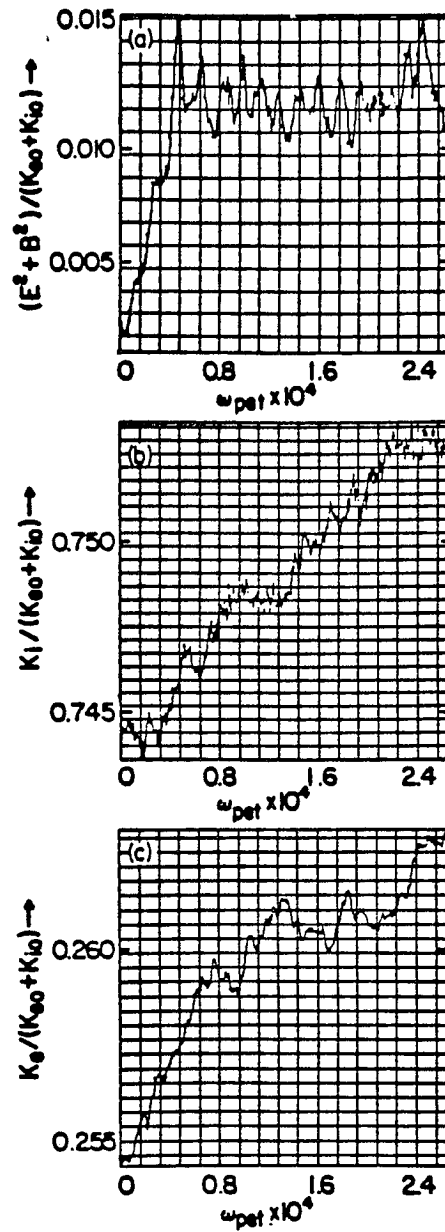


Figure 3.33. Time evolution of a) total electromagnetic field energies, b) total ion kinetic energies, and c) total electron kinetic energies ending at $\omega_{pe}t = 26400$ for Case 2 of Sec. 3.4.

antenna which in turn significantly reduces the heating levels.

For both cases, the wave energy is enhanced very little above the antenna excitation levels due to the boundaries. The ion reflections the walls serve to dephase the ions with respect to the wave acting as a thermalization agent for those ions near the boundaries. The electron and ion kinetic energies increase linearly with power consistent with electron Landau damping and ion $\mathbf{E} \times \mathbf{B}$ sloshing with the wave.

3.5 Driven Alfvén Waves in a Bounded, Nonuniform Plasma

Thus far, the excitation of kinetic Alfvén waves and associated heating processes have been examined in homogeneous plasmas. For the Alfvén wave resonance heating scheme, the variation of the plasma parameters plays an essential role. Nonuniformity presents much richer phenomena than is observed in the uniform cases previously presented. We are particularly interested in the situation in which the plasma contains a shear Alfvén resonance layer. The results in this section are therefore a step closer to experimentally relevant situations. The bounded model is used for the nonuniform cases presented here. All of the cases considered in this section contain an Alfvén wave resonance layer. There are two examples where the condition $v_A = v_{Te}$ is satisfied at the resonance layer and one example where $v_A < v_{Te}$ at the resonance layer.

The variation of the density is an important nonuniformity present in the laboratory experiments. In our numerical model the algorithm scheme of renormalization used to solve the transverse electric field involves an iteration about the perturbed density. A density gradient is likely to worsen the convergence properties of this iterative field solver. Instead, in the present model, the nonuniformity in the Alfvén velocity is introduced through the variation of the externally imposed magnetic field. This is accomplished

in a manner that does not degrade the solution for the transverse electric field. The ambient magnetic field is varied by the relation

$$B_y(x) \propto B_z(x) \propto B_0(x) = \frac{B_0(x = x_{\text{res}})}{[a(x - x_{\text{res}}) + 1.0]^{1/2}}$$

where the variable a is related to the shear length L_{res} at the resonance layer by $a = -2/L_{\text{res}}$. The angle θ between the y - and z -components of the ambient magnetic field maintains a constant value throughout the plasma for this type of variation. The center of the resonance layer is chosen to coincide with the center of the active system, i.e., $L_{\text{res}} = L_x/2$. For the cases presented in this section, the ions and electrons have initially equal temperatures, $T_i = T_e$. The antenna excites a single mode travelling wave given by either Eq. (3.15) or (3.16). There is an average of 9 particles per grid cell with each particle having the size $a_x \times a_y = 1.5\Delta \times 15\Delta$. It is necessary to include more particles to adequately model the nonuniform system. Results from three examples are presented in this section.

CASE 1 — $v_a(x_{\text{res}}) = v_{Te}$: Smaller System

The first nonuniform case we examine has the Alfvén speed at the resonance layer equal to the electron thermal velocity, i.e., $v_A(x_{\text{res}}) = v_{Te}$. It is expected that electron heating will be efficient for this example, because the phase velocity of the kinetic Alfvén wave falls on the portion of the electron velocity distribution function where the gradient is substantial. We will discuss in detail the mode structure of the wave electromagnetic fields and the wave absorption processes. We will further discuss the time evolution of the system and its implications.

Results for this example were obtained from a simulation system of size $L_x \times L_y = 64\Delta \times 320\Delta$. The ion-to-electron mass ratio is $M/m = 1600$. Quantities that depend on the magnetic field will be quoted

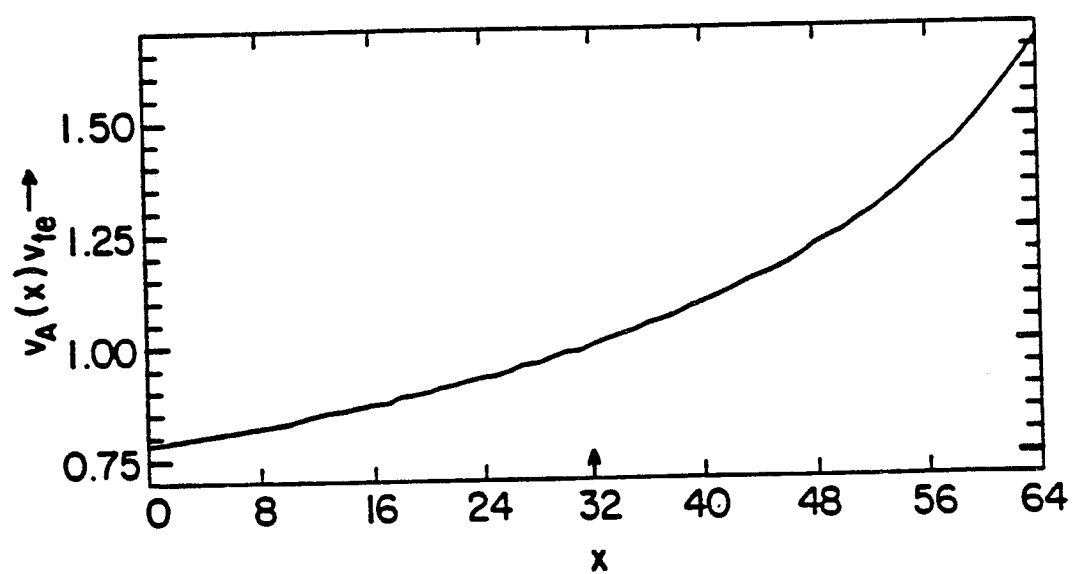


Figure 3.34. Spatial variation of the Alfvén speed v_A for Case 1 of Sec. 3.5.

by their values at the resonance layer. Various other plasma parameters have the values: $\beta(x_{\text{res}}) = 1.7 \times 10^{-3}$, $v_{Te} = 1.0\omega_{pe}\Delta$, $\Omega_i(x_{\text{res}}) = 8.3 \times 10^{-3}\omega_{pe}$, $\rho_i(x_{\text{res}}) = 3.0\Delta$, $x_{\text{res}} = 32\Delta$, $\omega_{pe}\Delta t = 15.0$, $\theta = 3.1^\circ$, $L_{\text{res}} = 100\Delta$, and $v_A(x_{\text{res}}) = 1.0\omega_{pe}\Delta$. The antenna parameters are assigned the values: $\omega_A = 1.08 \times 10^{-3}$, $k_A\Delta = 1.96 \times 10^{-2}$, and $W = 6.5 \times 10^{-3}$. The variation of the Alfvén speed with x is graphically depicted in Fig. 3.34. The magnetic field has its maximum value at the boundary where the antenna is placed. This simulation evolved to time $\omega_{pe}t = 54000$ which corresponds to 9.3 wave periods.

The initial electric and magnetic fields generated by the antenna are shown in Fig. 3.35 when the plasma temperature is essentially zero. The antenna electric field has most of its energy within the immediate vicinity of the antenna. The magnetic fields from the antenna are strongest near the antenna but penetrate further into the plasma. Contour plots of the x -component of the magnetic field depicted in Fig. 3.36 indicate the development of the kinetic Alfvén wave in the vicinity of the resonance layer that is not present at $t = 0$. Comparison of Figs. 3.36b and 3.36c demonstrate the wave in the resonance region propagates in the y -direction with the antenna. The strength of the wave is still stronger in the region adjacent to the antenna.

The Fourier transformed values of the electric and magnetic fields, $\mathbf{E}_L(\mathbf{k}, t)$, $\mathbf{E}_T(\mathbf{k}, t)$, and $\mathbf{B}(\mathbf{k}, t)$, at each time step are stored on disk for subsequent analysis. A three-dimensional representation showing the time evolution of a particular electric or magnetic field component can be processed from the data. The particular formulations that best display the information are plots of the field energy density spectrum $|E(x, k_y, t)|^2$ where x and t are varied and k_y is held fixed. The energy density spectra for the field

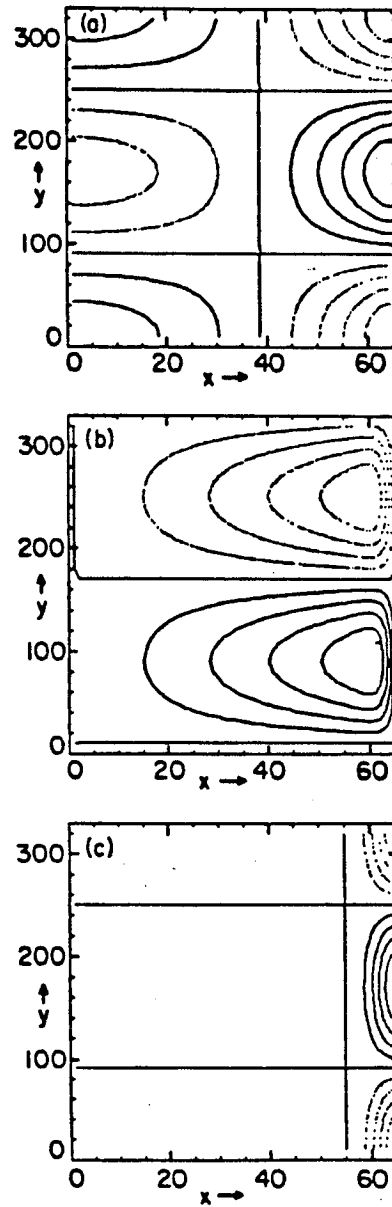


Figure 3.35. Contour plots of the fields a) B_z , b) B_y , and c) E_{Tz} generated by the antenna at $\omega_{pe}t = 0$ for a zero-temperature plasma in a system bounded in x of size $L_x \times L_y = 64\Delta \times 320\Delta$.

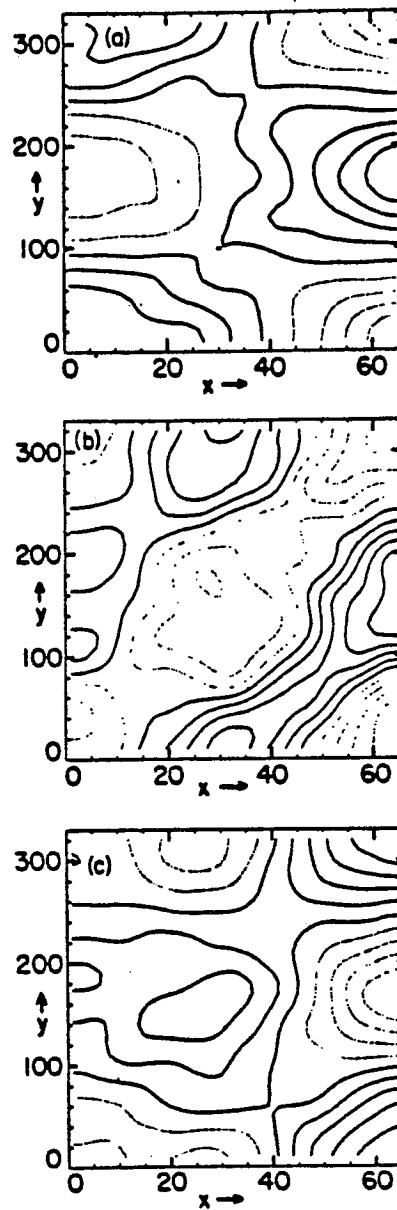


Figure 3.36. Contour plots of the magnetic field component B_x at a) $\omega_{pe}t = 0$, b) $\omega_{pe}t = 6000$, and c) $\omega_{pe}t = 9000$ for Case 1 of Sec. 3.5.

components $|E_{Tz}(x, k_A, t)|^2$, $|B_x(x, k_A, t)|^2$, and $|E_{Ly}(x, k_A, t)|^2$ are shown in Fig. 3.37 from different perspectives. The E_{Ly} spectrum is not directly generated by the antenna but is directly due to the plasma response. In the plots in Fig. 3.37, the lines running parallel to the time axis show the temporal variation at a particular spatial position with each line representing an average over three grid points. The lines running parallel to the x -axis similarly show the spatial variation at a given time interval with each line representing an average over one-fourth of an antenna period. The perspectives in Fig. 3.37a-c highlight the different spatial and temporal views.

Inspection of Fig. 3.37 demonstrates the development of Alfvén wave near the resonance indicating that mode conversion has occurred. The mode converted kinetic Alfvén wave grows during the initial 1.5 wave periods of the simulation. The amplitude of the wave energy in the resonance region is fairly constant for the following two periods. A decline in amplitude then occurs after $\omega_{pet} = 20000$. The peak of the mode converted wave is shifted towards smaller x than what is expected. The resonance layer is expected to be centered at $x_{res} = 32\Delta$ but the maximum value of the time averaged wave energy occurs at $x = 27\Delta$. The boundaries may influence the location of the mode conversion region since the system length in the x -direction is about 20 ion Larmor radii. As was seen in the uniform cases, the electrostatic potential Φ of the kinetic Alfvén wave propagates in phase with the vector potential a_z .

The electric and magnetic fields in the region adjacent to the antenna are larger in magnitude than the wave fields generated in the resonance layer. The wave at the edge has the same features as the resonant wave. Both propagate in the y -direction with the antenna current with the same phase structure between the components of the electric and magnetic

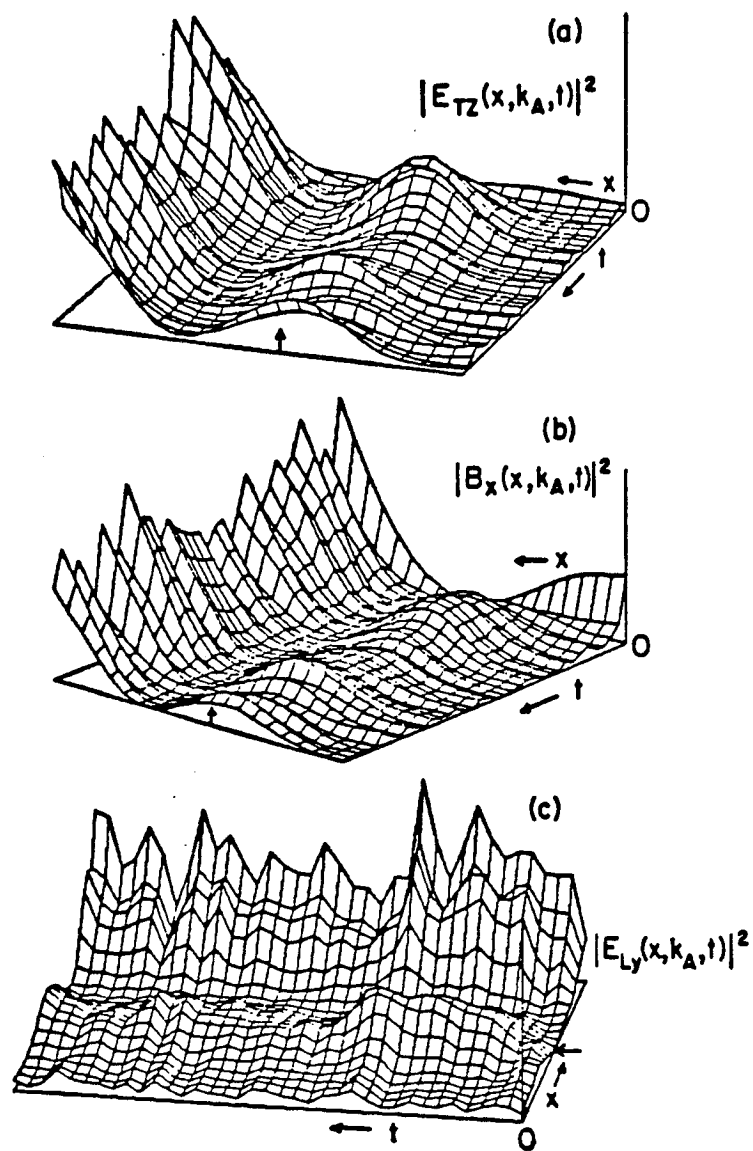


Figure 3.37. Spatial dependence and temporal evolution of the field energy densities a) $|E_{Tz}(x, k_A, t)|^2$, b) $|B_x(x, k_A, t)|^2$ and c) $|E_{Ly}(x, k_A, t)|^2$ from different perspectives ending at $\omega_{pe}t = 54000$ for Case 1 of Sec. 3.5.

fields. This wave that forms adjacent to the antenna might be an electromagnetic sheath developed by the plasma. The formation of electrostatic sheaths around an antenna for the lower hybrid frequencies has been investigated by Decyk and Dawson^{30,31} using a $2\frac{1}{2}D$ electrostatic particle simulation code. It is also possible that the nonuniformity does not sufficiently move the plasma parameters away from the resonance regime for nonresonant behavior to occur. The analysis is complicated by the particle reflections that occur at the boundaries.

The spatially averaged distribution function for the parallel electron velocity shown at different times in Fig. 3.38 exhibit flattening near the parallel wave phase velocity at the later times. The alteration of the local electron velocity function within the mode conversion region should undoubtedly be greater than what is seen in Fig. 3.38. We believe that the decline of the wave fields after $3\frac{1}{2}$ wave periods is related to the change in the electron velocity distribution function. This modification from its initial state changes the plasma properties from what can be expected in the linear regime.

As we expected, the kinetic Alfvén wave generated by the antenna also heats electrons. Examination of the variation in the electron temperature as a function of x is a particularly relevant diagnostic for the nonuniform case. These temperature profiles are shown in Fig. 3.39. A broad maximum of the electron temperature develops within the mode conversion region. The largest increase occurs in the region immediately adjacent to the antenna with a smaller increase seen near the opposite (left) boundary. The rate of heating in the resonance region slows from $\omega_{pet} = 24000$ to $\omega_{pet} = 36000$ compared to times prior to $\omega_{pet} = 24000$. This coincides with the decrease of the mode converted wave fields. The temperature peak in the

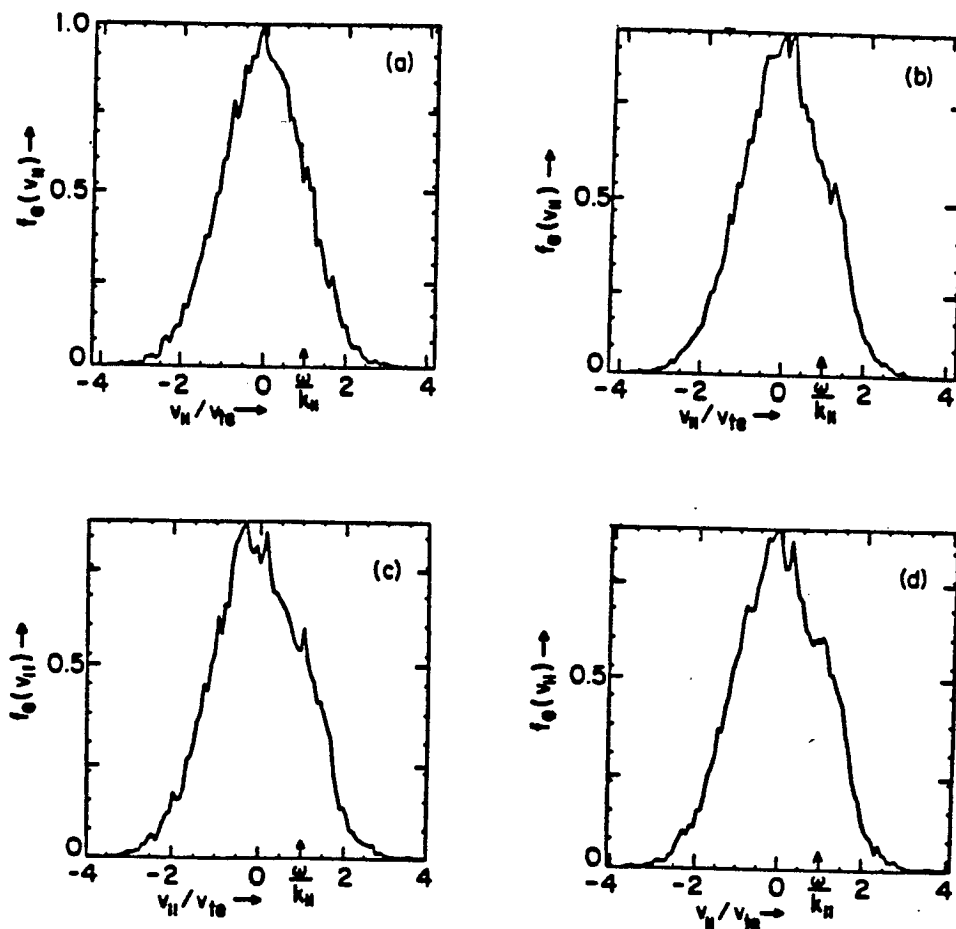


Figure 3.38. Electron velocity distribution function parallel to the magnetic field at a) $\omega_{pet} = 0$, b) $\omega_{pet} = 12000$, c) $\omega_{pet} = 24000$, and d) $\omega_{pet} = 36000$ for Case 1 of Sec. 3.5.

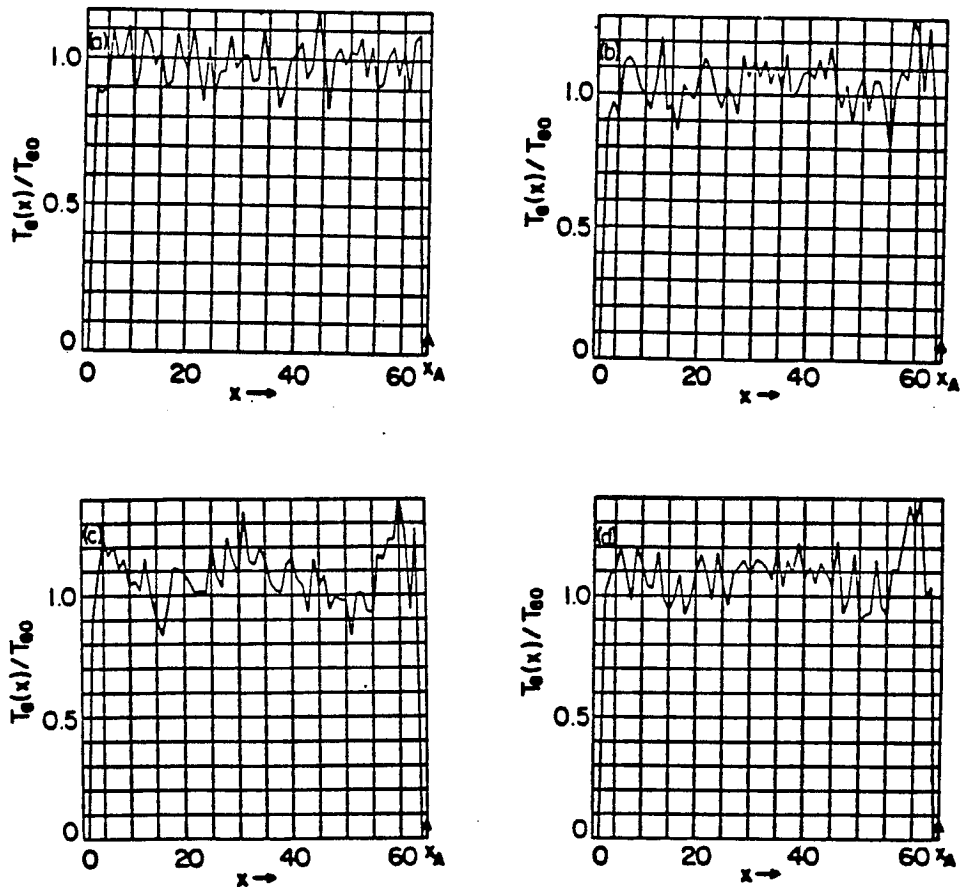


Figure 3.39. Spatial dependence of the electron temperature at a) $\omega_{pet} = 0$, b) $\omega_{pet} = 12000$ c) $\omega_{pet} = 24000$, and d) $\omega_{pet} = 36000$ for Case 1 of Sec. 3.4.

center of the simulation at $\omega_{pe}t = 24000$ broadens in the x -direction as time progresses, probably due to $\mathbf{E} \times \mathbf{B}$ diffusion of particles.

The temperature increase in the mode conversion region will be compared with the theoretical formula Eq. 3.14. This must be carefully done because the calculation of the heating rate from Landau damping assumes that a single coherent wave interacts linearly with the plasma. We shall evaluate the expression

$$\frac{1}{T_e} \frac{dT_e}{dt} = \frac{\delta_e \omega_{pe}^2}{U_e \omega} \int_{x_1}^{x_2} \int_0^{L_y} \frac{|E_{\parallel}(x, y)|^2}{8\pi} dx dy \quad (3.17)$$

over the range $24\Delta \leq x \leq 35\Delta$ until time $\omega_{pe}t = 24000$. From the stored data of the electric fields, the parallel electric field at the grid points through the length of the run can be reconstructed. The integral in the above expression can be approximated by a sum over the grid points within the volume of integration. Using

$$\int_{x_1}^{x_2} \int_0^{L_y} f(x, y) dx dy \simeq \sum_{\text{all } y_g} \sum_{x_1 < x_g < x_2} f(x_g, y_g) \Delta x \Delta y$$

where it is presumed that the points x_1 and x_2 lie halfway between adjacent grid points, Eq. (3.17) becomes

$$\frac{1}{T_e} \frac{dT_e}{dt} = \frac{\delta_e \omega_{pe}^2}{U_e \omega} \sum_{\text{all } y_g} \sum_{x_1 < x_g < x_2} |E_{\parallel}(x_g, y_g, t)|^2. \quad (3.18)$$

The integration over time of Eq. 3.18 is also performed numerically. A time-centered finite differencing yields

$$\frac{1}{T_{e0}} \frac{T_e(t + \Delta t) - T_e(t)}{\Delta t} = \frac{\delta_e \omega_{pe}^2}{U_{e0} \omega} \sum_{\text{all } y_g} \sum_{x_1 < x_g < x_2} \left| E_{\parallel} \left(x_g, y_g, t + \frac{\Delta t}{2} \right) \right|^2 \quad (3.19)$$

where the total temperature increase is assumed to be small enough such that initial values can be used for T_e and U_e in the denominations of Eq. (3.19). If Eq. (3.19) is summed over N time steps, we find that

$$\frac{T_e(N\Delta t) - T_{e0}}{T_{e0}} \simeq \frac{\delta e \omega_{pe}^2}{U_{e0} \omega} \Delta t \sum_{n=1}^N \sum_{\text{all } y_g} \sum_{x_1 < x_g < x_2} \left| E_{\parallel} [x_g, y_g, (n - 1/2)\Delta t] \right|^2. \quad (3.20)$$

The electric field values stored in the correlation data include the thermal fluctuations as well as the coherent wave. The inclusion of these fields in Eq. (3.20) yields an increase far in excess of the actual temperature increase since these fields do not on average contribute to electron heating. To minimize these contributions, the parallel electric field is Fourier transformed to \mathbf{k} -space. All of the \mathbf{k} -components of the parallel electric field are set to zero except the $(k_x, k_y = k_A)$ modes. The parallel electric field is subsequently inverse Fourier transformed back to configuration space. For the grid points located in the area between $24.5\Delta < x < 35.5\Delta$, the average increase of the electron temperature from $\omega_{pe}t = 0$ to $\omega_{pe}t = 24000$ is 19%. The predicted increase from a summation over all the grid points within that region using the parallel electric field that has been \mathbf{k} -filtered is 28% agreeing reasonably well with the simulation. One reason that the computed estimate is larger than the simulation value is that the modification of the electron velocity distribution function may already slow the heating from what is expected from a linear calculation. Another reason is that the \mathbf{k} -space filtering may not remove all of the thermal contribution to the parallel electric field. In any case, to our best knowledge, this is the first identification of a heating method in a particle simulation where a temperature increase is directly compared with theoretical values.

The time evolution of the total electromagnetic field energy displayed in Fig. 3.40 verifies the decline in field energy after $\omega_{pet} = 20000$ indicated in Fig. 3.37. The field energy does not show any dramatic increases above initial values. The ion kinetic energy undergoes a rapid increase during the first wave period as the kinetic Alfvén wave establishes itself and increases linearly afterwards. The kinetic energy growth is split between the two ion temperatures T_{ix} and $T_{i\perp}$ with $T_{i\perp}$ growing 4.4% and T_{ix} growing 3.5%. These increases are too small to pick out any definite features in the spatial dependence above the fluctuation level. There is an energy exchange again between the ions and the field energy clearly seen towards the completion of the run. This energy exchange has a frequency that is 1.5 times the pump frequency in contrast to twice the value observed in the periodic simulations. The increase of the ion temperatures are reasonably explained by $\mathbf{E} \times \mathbf{B}$ oscillations primarily driven by the electrostatic electric fields. Some true thermalization occurs from the phase mixing caused by ion reflections at the boundaries.

The total electron kinetic energy increases most rapidly from times $\omega_{pet} = 9000$ to $\omega_{pet} = 15000$. The heating rate then undergoes a subsequent decline until $\omega_{pet} = 22000$, after which it increases more slowly. The rate of electron heating slows as the electron velocity distribution function flattens. The decline in the electromagnetic field energy also correlates well with the decrease in the electron heating rate. The total electron kinetic energy increases 13% above its initial thermal value. This value is smaller than what would be experimentally measured since our measurement does not include electron thermal motion perpendicular to the magnetic field. Through the length of the run, the electrons acquire a net drift velocity that is approximately 5% of the electron thermal velocity. Current profiles indicate

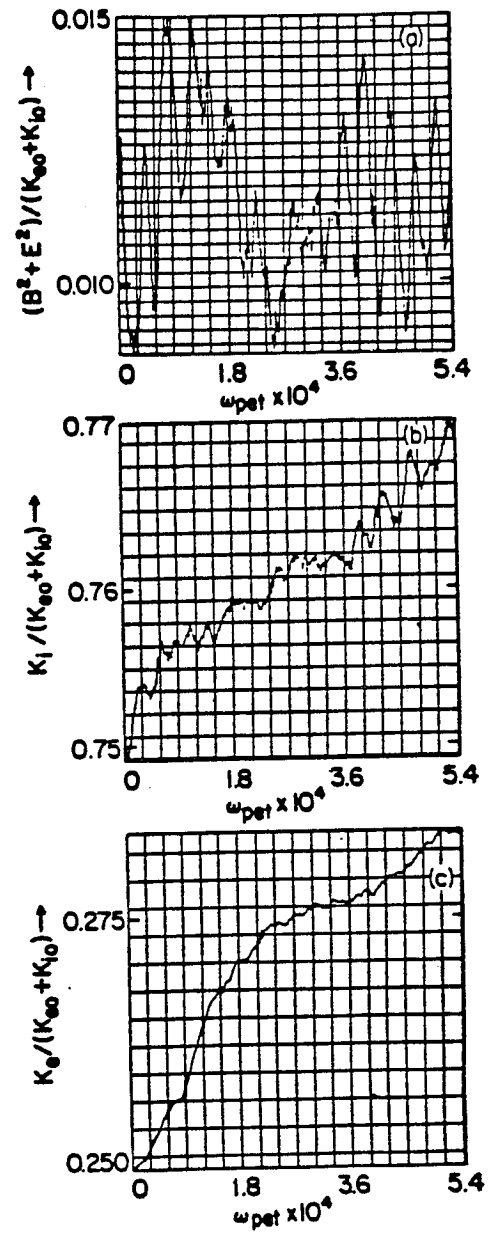


Figure 3.40. Time evolution of the a) total electromagnetic field energies, b) total ion kinetic energies, and c) total electron kinetic energies ending at $\omega_{pet} = 54000$ for Case 1 of Sec. 3.5.

there are negative electron drift current spikes located right at both particle reflection boundaries. A little further towards the interior of the right (antenna-side) boundary, a positive electron current develops that is broader in spatial extent than the current spikes at the edges. The current spikes appear to be caused by nonphysical coupling with the particle reflections.

CASE 2 — $v_A(x_{\text{res}}) = v_{Te}$: Larger System

We have examined another example with parameters very similar to Case 1 in a system twice as long in the x -direction. Our hope was that the larger system size would lead to a larger separation between the resonance region and the wave phenomena adjacent to the antenna. The antenna strength is increased adiabatically from zero to its full strength over one period as described by Eq. (3.16). The simulation parameters that are different from Case 1 are $L_x \times L_y = 128\Delta \times 320\Delta$, $L_{\text{res}} = 200\Delta$, and $W = 2.2 \times 10^{-2}$. Since a larger system is more expensive to simulate, the pump strength is increased over Case 1 in order to accelerate the pace of events.

The contours of the initial electromagnetic fields directly driven by the antenna in a zero temperature plasma seen in Fig. 3.41 show that the wave energy is relatively more localized to the antenna. Comparison of the contours of B_x at times $\omega_{pe}t = 6000$ and $\omega_{pe}t = 9000$ in Fig. 3.42 indicates that mode conversion has occurred from the development of a wave in the resonance region. The three-dimensional pictures of the energy density spectra $|B_x(x, k_A, t)|^2$, $|E_{Ly}(x, k_A, t)|^2$, and $|E_{Tz}(x, k_A, t)|^2$ in Fig. 3.43 demonstrate the development of kinetic Alfvén wave in the vicinity of the resonance layer. The lines running parallel to the x -axis are averaged over one-quarter of a wave period and the lines running parallel to the time axis are averaged over three adjacent grid points. The center of the resonance layer is expected to be at $x_{\text{res}} = 64\Delta$ and the peak of simulation occurs

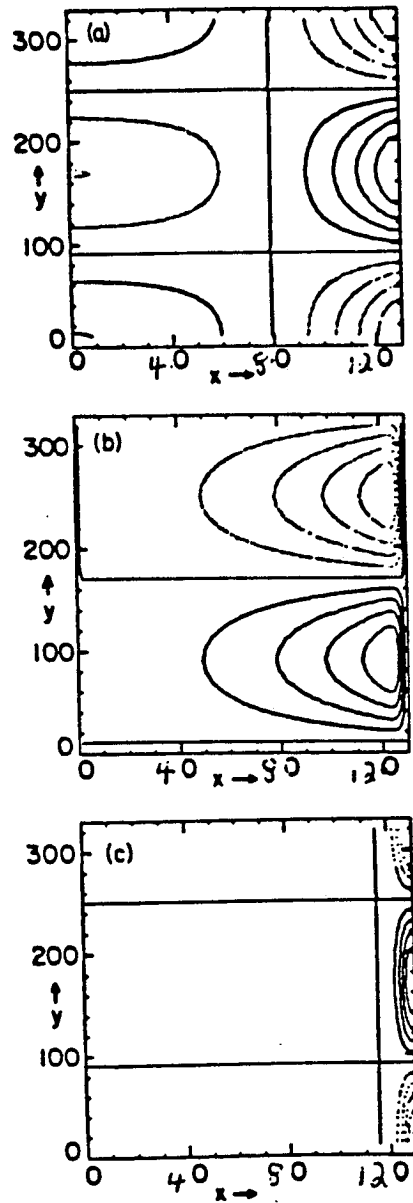


Figure 3.41. Contour plots of the fields a) B_z , b) B_y , and c) E_{Tz} generated by the antenna at $\omega_{pe}t = 0$ for a zero-temperature plasma in a system bounded in the x -direction of size $L_x \times L_y = 128\Delta \times 320\Delta$.

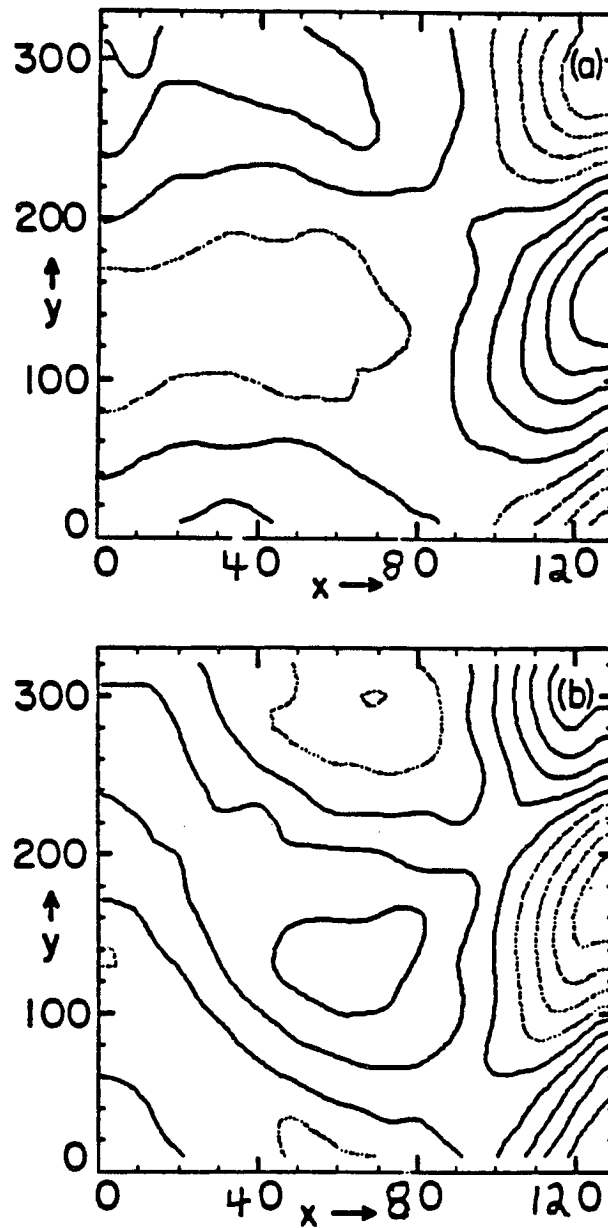


Figure 3.42. Contour plots of the magnetic field component B_z at a) $\omega_{pe}t = 6000$ and b) $\omega_{pe}t = 9000$ for Case 2 of Sec. 3.5.

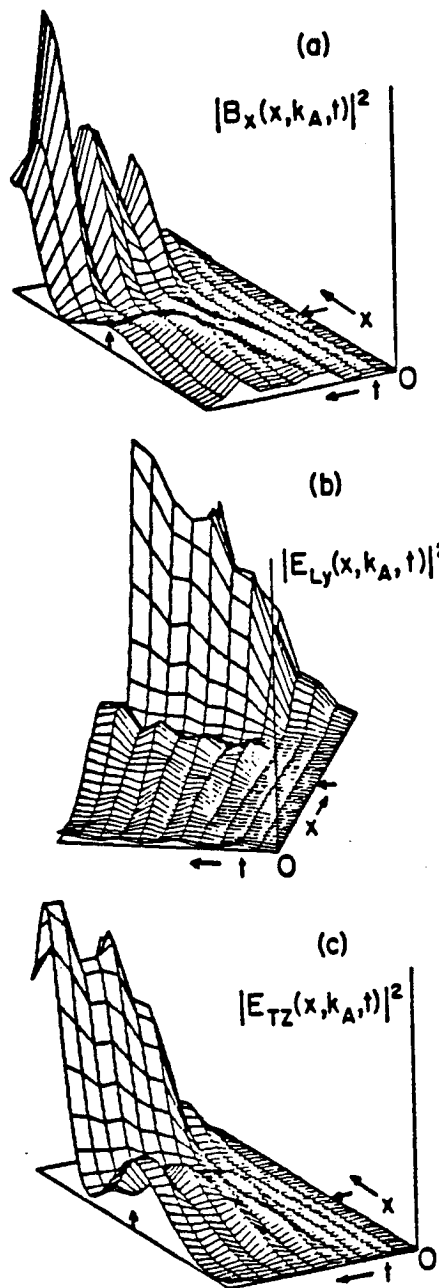


Figure 3.43. Spatial dependence and temporal evolution of the field energy densities a) $|B_x(x, k_A, t)|^2$, b) $|E_{Ly}(x, k_A, t)|^2$, and c) $|E_{Tz}(x, k_A, t)|^2$ from different perspectives ending at $\omega_{pe}t = 18000$ for Case 2 of Sec. 3.5.

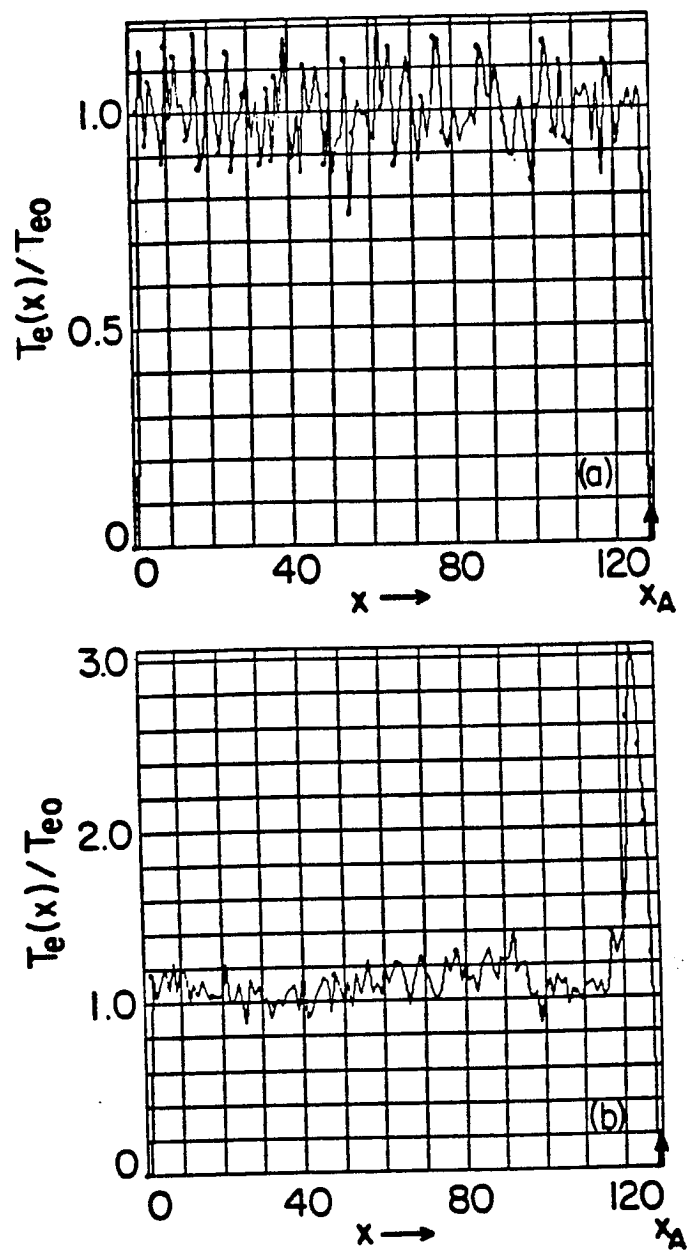


Figure 3.44. Spatial dependence of the electron temperature at a) $\omega_{pet} = 0$ and b) $\omega_{pet} = 18000$ for Case 2 of Sec. 3.5.

at $x = 57\Delta$ for the B_x energy density spectra and $x = 62\Delta$ for the E_{Ly} and E_{iz} energy density spectra. For the larger system the shift of the peak in the resonance region is less than for the smaller system of Case 1. The wave fields from near the antenna produce much larger effects on the plasma near the antenna. After only three periods, the local electron temperature has increased as much as 200% as can be seen from Fig. 3.44. This very large increase close to the antenna masks the particle interactions with the mode converted wave on the interior of the plasma and makes it difficult to draw useful information from this run other than the existence of the kinetic Alfvén wave in the resonance region.

CASE 3 — $v_A(x_{\text{res}}) < v_{Te}$

As the conclusion of this section, the results from a nonuniform example where the plasma β in the resonance region is well above the electron-to-ion mass ratio, $\beta(x_{\text{res}})M/m = 8.6$. The parameters for the plasma at the resonance layer and the antenna are: $L_x \times L_y = 64\Delta \times 320\Delta$, $\beta = 9.4 \times 10^{-3}$, $M/m = 900$, $v_{Te} = 1.2\omega_{pe}\Delta$, $\Omega_i = 7.5 \times 10^{-3}\omega_{pe}$, $\rho_i = 5.4\Delta$, $\theta = 6.3^\circ$, $\omega_{pe}\Delta t = 8.0$, $\omega_A = 1.44 \times 10^{-3}\omega_{pe}$, $k_A\Delta = 1.96 \times 10^{-2}$ and $W = 4.5 \times 10^{-3}$. The system is followed to $\omega_{pe}t = 19200$ which is 4.4 wave periods. The amplitude of the antenna current is maintained at a constant value through the length of the run. From the results of the homogeneous runs, it is expected that the reaction of the plasma for this example will be weaker than seen in Cases 1 and 2 of this section.

The electric and magnetic fields generated by the antenna are the same as in Fig. 3.36. The contour plots of B_x in Fig. 3.45 show the development of some wave structure peaked to the left of the resonance layer. As is found in the earlier examples in this section, the wave electric and magnetic fields have their largest amplitudes in the region adjacent to

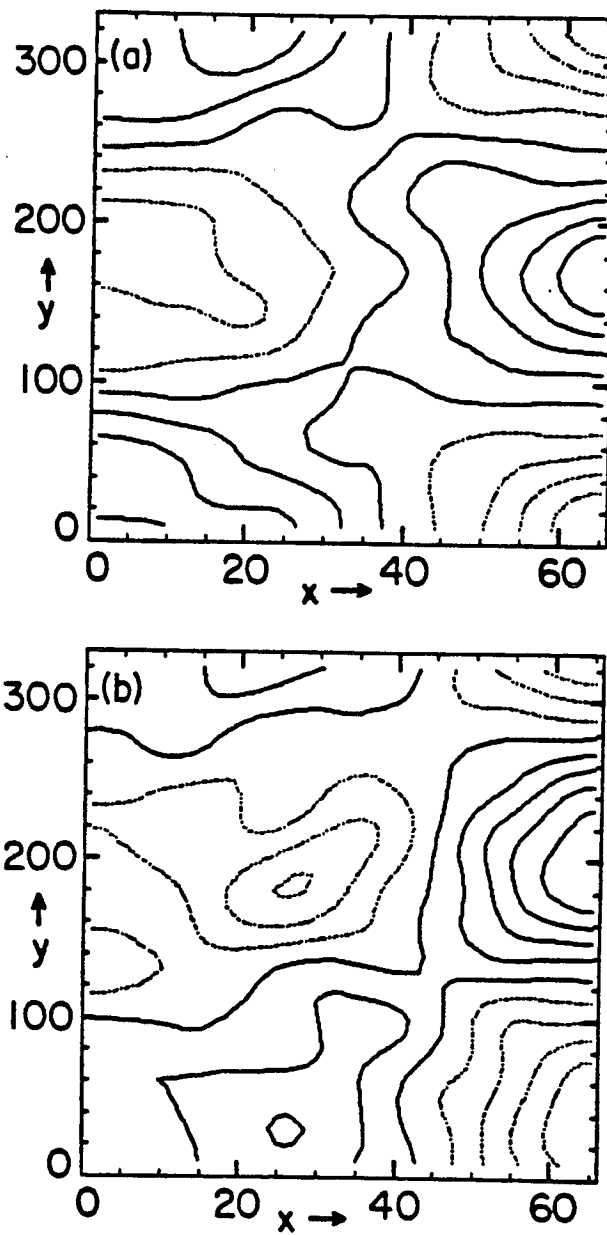


Figure 3.45. Contour plots of the magnetic field component B_z at a) $\omega_{pe}t = 0$ and b) $\omega_{pe}t = 4800$ for Case 3 of Sec. 3.5.

the antenna as can be seen from the three-dimensional graphs of field energy densities in Fig. 3.46. Lines running parallel to the time axis represent a spatial averaging over three grid points and lines running parallel to the x -axis are averaged over 0.25 wave periods. At initial times, there is a secondary maximum of the field energy at the left edge opposite of the antenna. As time progresses, the field energy densities, displayed in Fig. 3.46 decline at the left edge near $x = 0$ with a corresponding increase in amplitude near the resonance layer, which we interpret as the mode conversion of the kinetic Alfvén wave. The amplitude of this resonant wave is comparatively smaller than for Case 1 of this section. The evidence supporting the occurrence of the kinetic Alfvén wave mode conversion is weaker than in the previous examples but is nevertheless still convincing.

The electron velocity distribution function parallel to the magnetic field displays a weak level of flattening about the parallel phase velocity of the wave in Fig. 3.47. The time evolution of the electromagnetic field energy depicted in Fig. 3.48a does not have a net increase. The oscillations of the field energy seen in Fig. 3.48 are at approximately 1.5 times the pump frequency as is seen in Case 1. The ions participate very weakly if at all in these oscillations. The total ion kinetic energy increases only about 1% above its initial thermal value. The ion energy gain is almost evenly divided between the ion temperatures T_{ix} and $T_{i\perp}$. The electrons gain energy most rapidly during the first wave period as the kinetic Alfvén wave in the resonance region establishes itself. The net trend of the total electron kinetic energy after this is still increasing but at a much slower rate. There is a small decrease of energy beginning at 2.6 periods that is reminiscent of the decline in the homogeneous system discussed in Case 4 of Sec. 3.3. The increases in the temperatures are too small to detect spatial dependencies. The electron

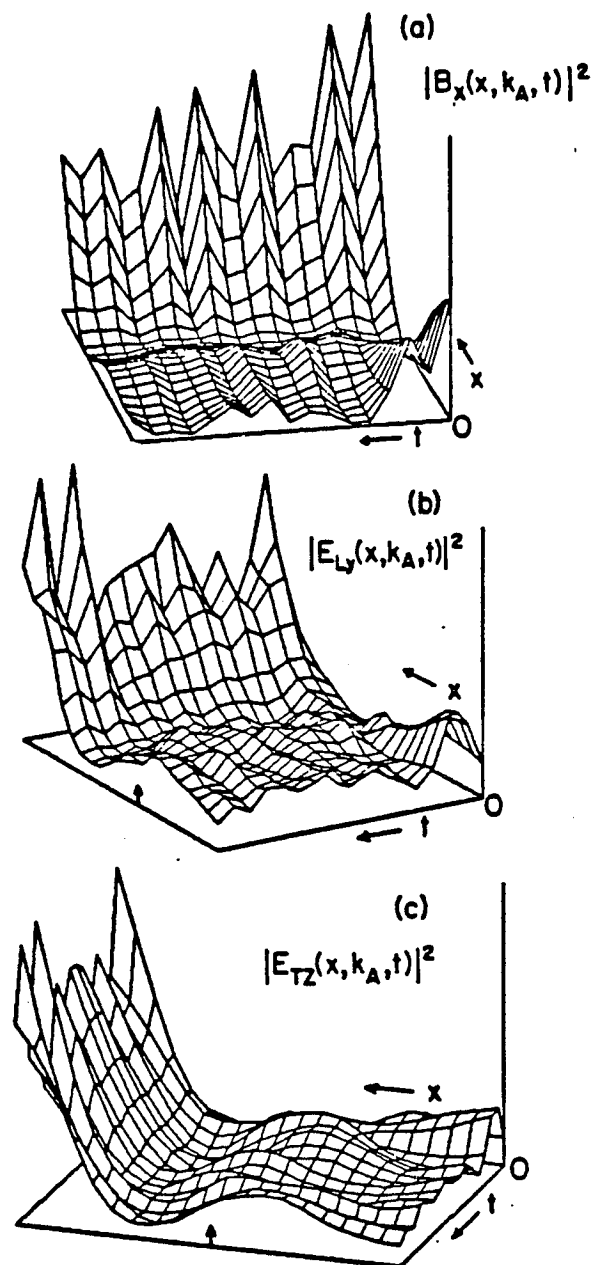


Figure 3.46. Spatial dependence and temporal evolution of the field energy densities a) $|B_x(x, k_A, t)|^2$, b) $|E_{Ly}(x, k_A, t)|^2$, and c) $|E_{Tz}(x, k_A, t)|^2$ from different perspectives ending at $\omega_{pe}t = 19200$ for Case 3 of Sec. 3.5.

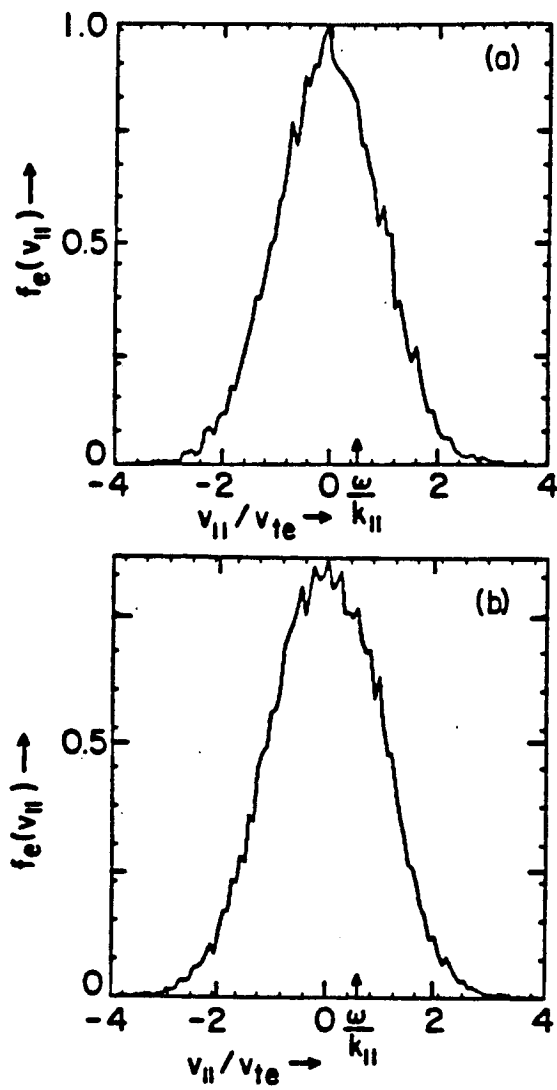


Figure 3.47. Electron velocity distribution function parallel to the magnetic field at a) $\omega_{pe}t = 0$ and b) $\omega_{pe}t = 19200$ for Case 3 of Sec. 3.5.

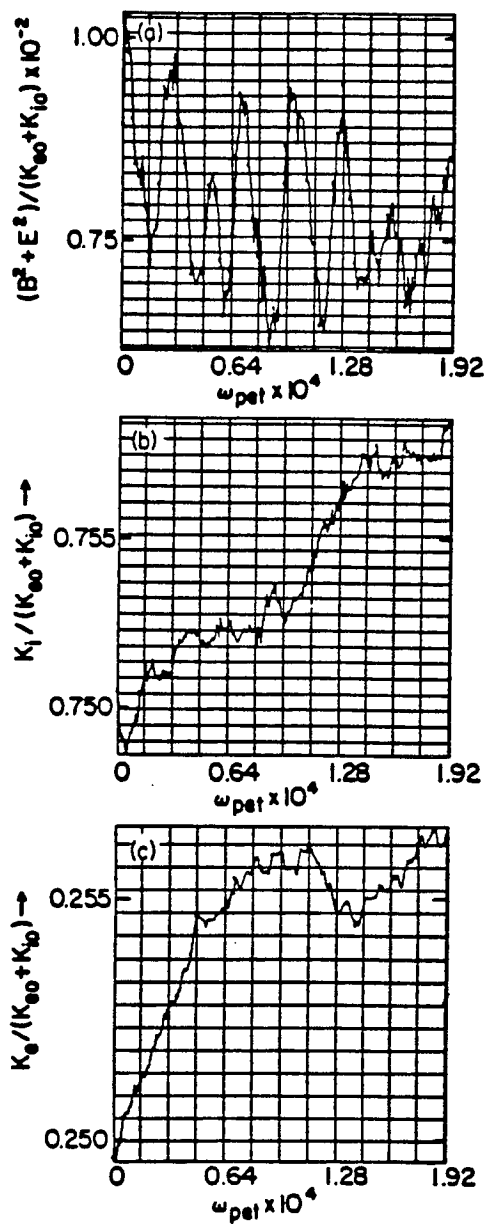


Figure 3.48. Time evolution of a) total electromagnetic field energies, b) total ion kinetic energies, and c) total electron kinetic energies ending at $\omega_{pet} = 19200$ for Case 3 of Sec. 3.5.

acquire a net drift velocity of $\langle v_D \rangle_{\parallel} = 0.01 v_{Te}$.

Two different parameter regimes have been examined in nonuniform systems. Mode conversion of the kinetic Alfvén wave is observed near the resonance layer for all three examples. However, the amplitude of the mode converted wave is smaller than the wave fields adjacent to the antenna. The time evolution of the resonant kinetic Alfvén wave suggests that its structure is sensitive to the shape of the electron velocity distribution function. The electron temperature increase in the mode conversion region agrees fairly well with the expectation of Landau damping. The resonance interaction for the lower β case where $v_A(x_{\text{res}}) = v_{Te}$ is stronger than for the higher β case where $v_A(x_{\text{res}}) = .56v_{Te}$.

In conclusion, we have clearly observed the mode conversion of the kinetic Alfvén wave and subsequent electron heating at the shear Alfvén resonance layer in a particle simulation for the first time to our best knowledge.

CHAPTER 4. SUMMARY AND CONCLUSIONS

The computational model presented here represents an attempt to extend the application of particle simulation to the low frequency regime of radio frequency heating in plasmas. We are specifically considering kinetic Alfvén wave resonance heating. This model incorporates two approximations from a complete classical treatment. The first approximation is Darwin's radiationless formulation of the electromagnetic field equations and the second is assuming that the electrons execute only $\mathbf{E} \times \mathbf{B}$ motion perpendicular to the magnetic field. The particle code model and algorithm are developed and explained in Part A of Chapter 2. In Part B of Chapter 2, the thermal properties of the model are found to agree very well with the predictions from linear Vlasov theory and equilibrium statistical mechanics. These tests give us evidence that the simulation behaves consistently with our expectations.

After having tested the simulation code, it is applied to investigate the kinetic processes associated with Alfvén wave resonance heating. This frequency range is an order of magnitude lower than what has been previously attempted with particle simulation of radio-frequency heating. Different parameter regimes were investigated in simulations that were 1) uniform systems with both the x - and y -direction periodic, 2) uniform systems with the x -direction bounded and the y -direction periodic, and 3) nonuniform systems with the x -direction bounded and the y -direction periodic.

When the resonance layer is not adjacent to a boundary, the kinetic Alfvén wave is seen to grow well above initial levels. Electron heating is produced by the kinetic Alfvén wave. The mechanism has been identified as Landau damping. The observed increase in the ion kinetic energy is caused by $\mathbf{E} \times \mathbf{B}$ drifts driven by the wave electrostatic fields. A large portion of

the total wave energy resides in the ion sloshing motion. If some mechanism exists to disrupt the phase (i.e., stochasticize) of the ion motion with respect to the wave fields, a net thermalization of the ions results. This seems to occur in the simulation from particle reflections at the boundaries over a long simulation run.

The Landau damping of the electrons progressed to a nonlinear stage where the electron velocity distribution function parallel to the magnetic field flattened about the parallel phase velocity of the wave. This alteration of the electron velocity distribution function has been correlated with a decline in the magnitude of the kinetic Alfvén wave in the resonance region and with a slowdown in the rate of electron heating. This slow-down of the electron heating has been predicted from quasilinear theory. It is known that the heating rate of the electrons will depend upon the thermalization rate of the electrons. However, the modification of the electron distribution can affect other basic plasma properties. Much of the theoretical investigation in radio-frequency heating has been concerned with the propagation of the wave launched by an edge antenna to the resonance region with the presumption that the wave energy will be effectively absorbed once it reaches the resonance region. Most of those works are based on the assumption that the absorption of wave energy does not significantly change the plasma behavior. However, our simulation results demonstrate that the plasma heating can alter the properties of the Alfvén wave when the local electron heating increases 5-10%. In contrast, the TCA tokamak reports gains of 25% in the bulk electron temperature. A wide band resonance might be able to prevent the original distribution function from severely distorting. One must be aware that the simulation with operates much higher power densities than currently exist in present experimental devices. Thermalization processes

would guide the electron velocity distribution function back to a Maxwellian more effectively in the experiments. There does exist experimental evidence of nonlinear behavior associated with the Alfvén wave heating scheme. For example, it has been observed on PRETEXT tokamak by T. Evans⁶⁴ that the electron density fluctuations reach a saturation level, $\tilde{n}_e/n_{e0} \sim 0.6\%$, in power scaling measurements. We therefore conjecture that nonlinear effects from the absorption of wave energy can modify the mode structures and wave propagation as well as heating rates and suggest this as an area for further theoretical and experimental investigation.

There are a number of directions that further work on this topic could take. Several of these involve adding more physically authentic features to the computational model. One important addition for the Alfvén wave heating problem is the inclusion of temperature and density profiles. The numerical method for solving the equation for the transverse electron field may have to be improved for this. It is also possible to extend the applicability of the model to high- β regimes by using the full magnetic field for the electron guiding center motion instead of the background magnetic field. Other elements that might be added are other guiding center drifts such as the curvature or ∇B drift and equilibrium current profiles. As the speed and memory of computers continue to increase, it may prove feasible to include a third spatial dimension. It will then be possible to examine more complex geometries that include the existence of the Global Alfvén Eigenmodes. The antennae used in an experiment launches a spectrum of modes rather than the single mode studied in this work. It would be relatively simple to include more modes in the simulation antenna current.

This simulation model can be utilized for other phenomena besides radio frequency heating. It has applications to problems where there

is a strong coupling between kinetic particle motion and low frequency electromagnetic modes. One of these areas that this simulation model is being used to examine is the destabilization of Alfvén waves by hot alpha particles. The deuterium-tritium fusion reaction produces alpha particles at 3.5 MeV in energy. The hot alpha particles produced in a magnetic confinement reactor will probably be largely concentrated at the center of the plasma. The expansion-free energy associated with the alpha particle pressure gradient is capable of driving various kinds of instabilities including coupling to Alfvén waves (Li, Mahajan and Chen⁶⁵). The destabilization of these modes can have deleterious effects on particle confinement: the Alfvén wave destabilization by alpha pressure gradient should flatten the alpha pressure profile. There are several issues that are not readily amenable to a linear analysis. One particularly important question is what is the saturation level of the destabilized modes and what kind of the alpha pressure profile result.

Particle simulation can help answer questions related to the nonlinear evolution of this problem. We again begin with a simpler system as is described below. An incompressible version of the code (neglects compressional Alfvén wave propagation) with a second ion species representing the alpha particles is being utilized on this problem. The alpha particles are placed nonuniformly through the system creating a density gradient. The effects of magnetic shear on stabilizing or destabilizing the mode are also included. We have only preliminary results so far but the effort on this problem is ongoing.

Appendix A - Solution for the Transverse Electric Field

The details of the solution for the transverse electric field are presented in this Appendix. The method of solution shown here follows the same procedure as outlined in Busnardo-Neto et al.⁴⁸ The beginning expressions are Eqs. 2.43 and 2.45 for the transverse electric field and for the partial time derivative of the plasma current

$$\nabla^2 \mathbf{E}_T = \frac{4\pi}{c^2} \left(\frac{\partial \mathbf{J}_p}{\partial t} + \frac{\partial \mathbf{J}_{\text{ext}}}{\partial t} \right)_T \quad (\text{A1})$$

$$\begin{aligned} \frac{\partial \mathbf{J}_p(\mathbf{x})}{\partial t} = & q_p \frac{e}{m} \sum_j^{\text{electrons}} S(\mathbf{x} - \mathbf{x}_j) \int \mathbf{E}_{\parallel}(\mathbf{x}') S(\mathbf{x}' - \mathbf{x}_j) d\mathbf{x}' \\ & + q_p \frac{e}{M} \sum_j^{\text{ions}} S(\mathbf{x} - \mathbf{x}_j) \int \left[\mathbf{E}(\mathbf{x}') + \frac{\mathbf{v}_j}{c} \times \mathbf{B}(\mathbf{x}') \right] S(\mathbf{x}' - \mathbf{x}_j) d\mathbf{x}' \\ & - \nabla \cdot \sum_j^{\text{all particles}} q_{pj} \mathbf{v}_j \mathbf{v}_j S(\mathbf{x} - \mathbf{x}_j) \end{aligned} \quad (\text{A2})$$

where

$$\mathbf{E}_{\parallel}(\mathbf{x}) = \hat{b}(\mathbf{x}) \left[\hat{b}(\mathbf{x}) \cdot \mathbf{E}(\mathbf{x}) \right].$$

We will rearrange Eqs. (A1) and (A2) moving all terms containing the transverse electric field to the left-hand side of the equation while retaining all other terms on the right-hand side.

The last term on the right-hand side of Eq. (A2) is already expressed in terms of known information. Define the variable \mathbf{D} as

$$\mathbf{D}(\mathbf{x}) = -\nabla \cdot \sum_j^{\text{all particles}} q_{pj} \mathbf{v}_j \mathbf{v}_j S(\mathbf{x} - \mathbf{x}_j). \quad (\text{A2})$$

The tensor formed by the product of the two velocities is computed on the grid in the same manner as the current density. This product formed on the

grid will be denoted by the variable IP such that

$$\mathbf{D}(\mathbf{x}) = -q_p \nabla \cdot \sum_g IP(\mathbf{x}_g) S(\mathbf{x} - \mathbf{x}_g). \quad (A3)$$

Since FFT techniques are used to solve Eq. (A1), we will want to compute the Fourier transform of Eq. (A3) which is given by

$$\mathbf{D}(\mathbf{k}) = -N_g q_p i\mathbf{k} \cdot IP(\mathbf{k}) S(\mathbf{k}). \quad (A4)$$

The summation of (A3) is then replaced by a simple product in Fourier space.

The remaining three terms are evaluated by following the same basic procedure. This procedure is followed for the electron acceleration term and ion acceleration terms. For convenience, the temporary vector \mathbf{A} is introduced as

$$\mathbf{A}(\mathbf{x}) = \sum_j^{\text{electrons}} S(\mathbf{x} - \mathbf{x}_j) \int \mathbf{E}_{\parallel}(\mathbf{x}') S(\mathbf{x}' - \mathbf{x}_j) d\mathbf{x}'. \quad (A5)$$

The integral can be formulated as a product in Fourier space in the following way

$$\mathbf{A}(\mathbf{x}) = \sum_j^{\text{electrons}} S(\mathbf{x} - \mathbf{x}_j) \sum_{\mathbf{k}'} V \mathbf{E}_{\parallel}(\mathbf{k}') S(-\mathbf{k}') e^{i\mathbf{k}' \cdot \mathbf{x}_j}.$$

We further Fourier transform $S(\mathbf{x} - \mathbf{x}_j)$ to yield

$$\begin{aligned} \mathbf{A}(\mathbf{x}) &= \sum_j^{\text{electrons}} V \sum_{\mathbf{k}} S(\mathbf{k}) e^{i\mathbf{k} \cdot (\mathbf{x} - \mathbf{x}_j)} \sum_{\mathbf{k}'} S(-\mathbf{k}') \mathbf{E}_{\parallel}(\mathbf{k}') e^{i\mathbf{k}' \cdot \mathbf{x}_j} \\ \mathbf{A}(\mathbf{x}) &= V \sum_{\mathbf{k}} S(\mathbf{k}) e^{i\mathbf{k} \cdot \mathbf{x}} \sum_{\mathbf{k}'} S(-\mathbf{k}') \mathbf{E}_{\parallel}(\mathbf{k}') \sum_j^{\text{electrons}} e^{i(\mathbf{k}' - \mathbf{k}) \cdot \mathbf{x}_j}. \end{aligned} \quad (A6)$$

The particle dependence has been reduced to a sum of exponential functions. The subtracted dipole scheme (SUDS) can now be used to interpolate this to the grid with the result

$$\sum_j^{\text{electrons}} e^{i(\mathbf{k}' - \mathbf{k}) \cdot \mathbf{x}_j} = \sum_g n_e(\mathbf{x}_g) e^{i(\mathbf{k}' - \mathbf{k}) \cdot \mathbf{x}_g}. \quad (A7)$$

The electron number density, which represents the number of finite size electrons in the neighborhood of \mathbf{x}_g , weights the exponential function to the grid. We further note that the right-hand side of Eq. (A7) yields the inverse Fourier transform of n_e

$$\sum_j^{\text{electrons}} e^{i(\mathbf{k}'-\mathbf{k})\cdot\mathbf{x}_j} = N_g n_e(\mathbf{k}-\mathbf{k}'). \quad (\text{A8})$$

With the use of Eq. (A8), the Fourier transform of Eq. (A5) becomes

$$\mathbf{A}(\mathbf{k}) = V N_g S(\mathbf{k}) \sum_{\mathbf{k}'} n_e(\mathbf{k}') S(\mathbf{k}'-\mathbf{k}) \mathbf{E}_{\parallel}(\mathbf{k}-\mathbf{k}') \quad (\text{A9})$$

where we have changed the summation indices such that $\mathbf{k}-\mathbf{k}' \rightarrow \mathbf{k}'$. The integral is thus replaced by a more tractable summation upon the application of the Fourier transform.

The analysis of the ion acceleration driven by the electric field term follows the exact same path as developed for the parallel electron acceleration term. By direct inspection of Eqs. (A5) and (A9), we can write

$$\begin{aligned} FFT^{-1} \left\{ \sum_j^{\text{ions}} S(\mathbf{x}-\mathbf{x}_j) \int \mathbf{E}(\mathbf{x}') S(\mathbf{x}'-\mathbf{x}_j) d\mathbf{x}' \right\}(\mathbf{k}) \\ = V N_g S(\mathbf{k}) \sum_{\mathbf{k}'} n_i(\mathbf{k}') S(\mathbf{k}'-\mathbf{k}) \mathbf{E}(\mathbf{k}-\mathbf{k}') \end{aligned} \quad (\text{A10})$$

for the ion electric field acceleration term of Eq. (A2), where n_i is the ion number density. The analysis of the ion Lorentz acceleration, the third term on the right-hand side of Eq. (A2), differs slightly because of its dependence on the velocity. This mainly manifests itself as the replacement of

$$\begin{aligned} \sum_j e^{i(\mathbf{k}'-\mathbf{k})\cdot\mathbf{x}_j} \\ \sum_j \mathbf{v}_j e^{i(\mathbf{k}'-\mathbf{k})\cdot\mathbf{x}_j} \end{aligned}$$

This summation involving ion velocities is similar to the accumulation of the current density. After being weighted to the grid, the summation can be written as

$$\sum_j \mathbf{v}_j e^{i(\mathbf{k}' - \mathbf{k}) \cdot \mathbf{x}_j} = N_g \mathbf{U}_i(\mathbf{k}).$$

We can then show that

$$\begin{aligned} FFT^{-1} \left\{ \sum_j S(\mathbf{x} - \mathbf{x}_j) \int \frac{\mathbf{v}_j}{c} \times \mathbf{B}(\mathbf{x}') S(\mathbf{x}' - \mathbf{x}'_j) d\mathbf{x}' \right\}(\mathbf{k}) \\ = V N_g S(\mathbf{k}) \sum_{\mathbf{k}'} \frac{\mathbf{U}_i(\mathbf{k}')}{c} \times \mathbf{B}(\mathbf{k} - \mathbf{k}') S(\mathbf{k}' - \mathbf{k}). \end{aligned} \quad (A11)$$

This expression simplifies if the magnetic field \mathbf{B} is replaced by its equivalent force \mathbf{F}_B . Remembering that

$$\mathbf{F}_B(\mathbf{k}) = V S(-\mathbf{k}) B(\mathbf{k}),$$

then the right-hand side of Eq. (A11) becomes

$$N_g S(\mathbf{k}) \sum_{\mathbf{k}'} \frac{\mathbf{U}_i(\mathbf{k}')}{c} \times \mathbf{F}_B(\mathbf{k} - \mathbf{k}').$$

The summation over \mathbf{k}' can prove to be computatively expensive if many k -components are kept in the model. This discrete convolution can be altered to

$$\begin{aligned} \sum_{\mathbf{k}'} \mathbf{U}_i(\mathbf{k}') \times \mathbf{F}_B(\mathbf{k} - \mathbf{k}') &= \frac{1}{N_g} \sum_g \mathbf{U}_i(\mathbf{x}_g) \times \mathbf{F}_B(\mathbf{x}_g) e^{-i\mathbf{k} \cdot \mathbf{x}_g} \\ &= FFT^{-1} \{ \mathbf{U}_i(\mathbf{x}_g) \times \mathbf{F}_B(\mathbf{x}_g) \}(\mathbf{k}). \end{aligned} \quad (A12)$$

It is usually more efficient to form the cross-product of \mathbf{U}_i and \mathbf{F}_B in configuration space on the grid and subsequently Fourier transform the product to \mathbf{k} -space. All of the quantities in the above expression are known prior to solving for the transverse electric field.

The Fourier transform of Eq. (A1) is used to solve for the transverse electric field. We can use Eqs. (A2), (A4), (A9), (A10) and (A12) to find the Fourier transform of the partial time derivative of the plasma current thusly,

$$\begin{aligned} \frac{\partial}{\partial t} \mathbf{J}_p(\mathbf{k}) = q_p \frac{e}{m} N_g S(\mathbf{k}) \left\{ \sum_{\mathbf{k}'} V n_e(\mathbf{k}') S(\mathbf{k}' - \mathbf{k}) \mathbf{E}_{\parallel}(\mathbf{k} - \mathbf{k}') \right. \\ \left. + \frac{m}{M} \sum_{\mathbf{k}'} V n_i(\mathbf{k}') S(\mathbf{k}' - \mathbf{k}) \mathbf{E}(\mathbf{k} - \mathbf{k}') + \frac{m}{M} \sum_{\mathbf{k}'} \frac{\mathbf{U}_i(\mathbf{k}')}{c} \times \mathbf{F}_B(\mathbf{k} - \mathbf{k}') \right\} \\ - q_p N_g S(\mathbf{k}) i\mathbf{k} \cdot \mathbf{I}P(\mathbf{k}). \end{aligned} \quad (\text{A13})$$

However, we solve for the force, \mathbf{F}_T rather than the field \mathbf{E}_T . The forces \mathbf{F}_T , \mathbf{F}_{\parallel} , \mathbf{F}_L , and \mathbf{F}_E are defined

$$\mathbf{F}_T(\mathbf{k}) = V S(-\mathbf{k}) \mathbf{E}_T(\mathbf{k})$$

$$\mathbf{F}_{\parallel}(\mathbf{k}) = V S(-\mathbf{k}) \mathbf{E}_{\parallel}(\mathbf{k})$$

$$\mathbf{F}_L(\mathbf{k}) = V S(-\mathbf{k}) \mathbf{E}_L(\mathbf{k})$$

$$\mathbf{F}_E(\mathbf{k}) = \mathbf{F}_T(\mathbf{k}) + \mathbf{F}_L(\mathbf{k}).$$

Using the above definitions and Eqs. (A1) and (A13), we have the following expression for the transverse electric force.

$$\begin{aligned} \frac{k^2 c^2}{V^2 |S(k)|^2} \frac{N_0}{N_g} \mathbf{F}_T(\mathbf{k}) + \omega_{pi}^2 \left[\sum_{\mathbf{k}'} n_i(\mathbf{k}') \mathbf{F}_E(\mathbf{k} - \mathbf{k}') \right]_T \\ + \omega_{pe}^2 \left[\sum_{\mathbf{k}'} n_e(\mathbf{k}') \mathbf{F}_{\parallel}(\mathbf{k} - \mathbf{k}') \right]_T = \mathbf{\Gamma}_T(\mathbf{k}) \end{aligned} \quad (\text{A14})$$

where

$$\begin{aligned} \mathbf{\Gamma}(\mathbf{k}) = -\omega_{pi}^2 \sum_{\mathbf{k}'} \frac{\mathbf{U}_i(\mathbf{k}')}{c} \times \mathbf{F}_B(\mathbf{k} - \mathbf{k}') \\ + \frac{m}{e} \omega_{pe}^2 i\mathbf{k} \cdot \mathbf{I}P(\mathbf{k}) - \frac{4\pi}{V S(\mathbf{k})} \frac{N_0}{N_g} \frac{\partial}{\partial t} \mathbf{J}_{\text{ext}}(\mathbf{k}). \end{aligned} \quad (\text{A15})$$

The right-hand side of Eq. (A14) consists of known quantities and is therefore a source term which we call \mathbf{F} . The source term \mathbf{F} is accumulated on the grid from the particle velocities. Equation (A14) can be written in matrix form as

$$[L] [F_T] = [I_T]$$

and has a formal solution of

$$[F_T] = [L]^{-1} [I_T].$$

However, it proves to be prohibitively expensive to invert $[L]$ at every time step for the dimensions of the simulation codes used here. We instead use an iterative procedure to solve Eq. (14). This unfortunately places limits on the applicability of the simulation model. These limits are discussed in the main body of the dissertation.

The iterative procedure involves removing the $\mathbf{k}' = 0$ terms from the summations on the left side of Eq. (A14) and transposing the other $\mathbf{k}' \neq 0$ terms to the right side. As a first approximation, the transverse electric force is solved setting the $\mathbf{k}' \neq 0$ terms containing the transverse electric force equal to zero. The transverse electric force equation is solved again with the values from the first solution placed in the summations with $\mathbf{k}' \neq 0$ terms on the source side of the equation. This process repeats itself until a convergence criteria is satisfied. This technique resembles the renormalization methods used to describe weak turbulence.

For the term depending on the ion number density, a straightforward application of this procedure yields

$$\sum_{\mathbf{k}'} n_i(\mathbf{k}') \mathbf{F}_E(\mathbf{k} - \mathbf{k}') = \frac{N_0}{N_g} \mathbf{F}(\mathbf{k}) + \mathbf{T}(\mathbf{k})$$

where the average number density is given by the division of the total number of particles by the number of grid points, e.g.,

$$n_i(\mathbf{k}' = 0) = \frac{N_0}{N_g} = n_e(\mathbf{k}' = 0)$$

and where

$$\mathbf{T}(\mathbf{k}) = \sum_{\mathbf{k}' \neq 0} n_i(\mathbf{k}') \mathbf{F}_E(\mathbf{k} - \mathbf{k}').$$

The summation over $\mathbf{k}' \neq 0$ is transposed to the right side of Eq. (A14). As was shown with Eq. (A12), the summation over $\mathbf{k}' \neq 0$ can be expressed as

$$\mathbf{T}(\mathbf{k}) = \text{FFT}^{-1} \left\{ \left[n_i(\mathbf{x}_g) - \frac{N_0}{N_g} \right] \mathbf{F}_E(\mathbf{x}_g) \right\}.$$

The summation over $\mathbf{k}' \neq 0$ is evaluated as a product in configuration space and is subsequently inverse Fourier transformed.

The evaluation of the electron term is more complicated since an electron is accelerated only in the locally parallel direction. This acceleration has contributions from both the longitudinal and transverse electric forces. Since we are solving for \mathbf{F}_T , we split the electric force into its longitudinal and transverse components thusly,

$$\begin{aligned} \sum_{\mathbf{k}'} n_e(\mathbf{k}') \mathbf{F}_{\parallel}(\mathbf{k} - \mathbf{k}') &= \frac{1}{N_G} \sum_g n_e(\mathbf{x}_g) \mathbf{F}_{\parallel}(\mathbf{x}_g) e^{-i\mathbf{k} \cdot \mathbf{x}_g} \\ &= \frac{1}{N_G} \sum_g n_e(\mathbf{x}_g) \hat{b}(\mathbf{x}_g) \hat{b}(\mathbf{x}_g) \cdot \mathbf{F}_T(\mathbf{x}_g) e^{-i\mathbf{k} \cdot \mathbf{x}_g} + \mathbf{G}(\mathbf{k}) \end{aligned} \quad (\text{A16})$$

where

$$\mathbf{G}(\mathbf{k}) = \frac{1}{N_g} \sum_g n_e(\mathbf{x}_g) \hat{b}(\mathbf{x}_g) \hat{b}(\mathbf{x}_g) \cdot \mathbf{F}_L(\mathbf{x}_g) e^{-i\mathbf{k} \cdot \mathbf{x}_g}.$$

Since it can be computed from known information, \mathbf{G} is transposed to the right side of Eq. (A14). To handle the summation containing the transverse electric force, we define

$$\delta n_e(\mathbf{x}_g) = n_e(\mathbf{x}_g) - \frac{N_0}{N_g}$$

$$\delta\hat{b}(\mathbf{x}_g) = \hat{b}(\mathbf{x}_g) - \langle \hat{b} \rangle$$

where

$$\langle \hat{b} \rangle = \frac{1}{N_g} \sum_g \hat{b}(\mathbf{x}_g).$$

The remaining summation with \mathbf{F}_T on the right side of Eq. (A15) can be further decomposed into

$$\frac{1}{N_g} \sum_g n_e(\mathbf{x}_g) \hat{b}(\mathbf{x}_g) \hat{b}(\mathbf{x}_g) \cdot \mathbf{F}_T(\mathbf{x}_g) e^{-i\mathbf{k} \cdot \mathbf{x}_g} = \frac{N_0}{N_g} \langle \hat{b} \rangle \langle \hat{b} \rangle \cdot \mathbf{F}_T(\mathbf{k}) + \mathbf{H}(\mathbf{k}) \quad (\text{A17})$$

where

$$\mathbf{H}(\mathbf{k}) = \frac{1}{N_g} \sum_g e^{-i\mathbf{k} \cdot \mathbf{x}_g} \left\{ \delta n_e(\mathbf{x}_g) \hat{b}(\mathbf{x}_g) \hat{b}(\mathbf{x}_g) \cdot \mathbf{F}_T(\mathbf{x}_g) + \frac{N_0}{N_g} \delta \hat{b}(\mathbf{x}_g) \hat{b}(\mathbf{x}_g) \cdot \mathbf{F}_T(\mathbf{x}_g) + \frac{N_0}{N_g} \langle \hat{b} \rangle \delta \hat{b}(\mathbf{x}_g) \cdot \mathbf{F}_T(\mathbf{x}_g) \right\}.$$

The variable \mathbf{H} is transposed to the right side of Eq. (A14) as a renormalization term.

With the help of Eqs. (A15)-(A17), we are able to write the left side of Eq. (A14) retaining lowest order terms of \mathbf{F}_T . Replacing the summations over \mathbf{k}' with their equivalent expressions from Eqs. (A15)-(A17), Eq. (A14) becomes

$$\left[\omega_{pi}^2 + \frac{k^2 c^2}{V^2 |S(\mathbf{k})|^2} \right] \frac{N_0}{N_g} \mathbf{F}_T(\mathbf{k}) + \frac{N_0}{N_g} \omega_{pe}^2 \left[\langle \hat{b} \rangle \langle \hat{b} \rangle \cdot \mathbf{F}_T(\mathbf{k}) \right]_T = \mathbf{F}'_T(\mathbf{k}') \quad (\text{A18})$$

where

$$\mathbf{F}'(\mathbf{k}) = \mathbf{F}(\mathbf{k}) - \omega_{pe}^2 \mathbf{T}(\mathbf{k}) - \omega_{pe}^2 \mathbf{G}(\mathbf{k}) - \omega_{pe}^2 \mathbf{H}(\mathbf{k}).$$

The ion term, \mathbf{T} , contains both the transverse and longitudinal electric force. The part of \mathbf{T} that is dependent on the longitudinal electric force and the variables \mathbf{F} and \mathbf{G} are kept for the first round solution since all physical

quantities represented by them are already known. The part of \mathbf{T} that is dependent on the transverse electric force and the variable \mathbf{H} are renormalization terms used in later iterations for the solution.

Let us examine Eq. (A18) for the specific case of a $2\frac{1}{2}$ dimension simulation with a background magnetic field in the y - z plane. The angle θ is defined such that

$$\tan \theta = \frac{\langle B_y \rangle}{\langle B_z \rangle}.$$

The mean magnetic field unit vector $\langle \hat{b} \rangle$ is easily seen to be

$$\langle \hat{b} \rangle = \sin \theta \hat{j} + \cos \theta \hat{k}.$$

Since the z -direction is ignorable for a $2\frac{1}{2} - D$ code, the wavenumber vector \mathbf{k} lies in the x - y plane. Under these circumstances, the components of Eq. (A18) are

$$R(k)F_{Tx}(\mathbf{k}) = \Gamma'_{Tx}(\mathbf{k}) + \frac{N_0}{N_g} \omega_{pe}^2 \frac{k_x k_y}{k^2} \sin \theta [F_{Ty}(\mathbf{k}) \sin \theta + F_{Tz}(\mathbf{k}) \cos \theta] \quad (\text{A19})$$

$$\left[R(k) + \frac{N_0}{N_g} \omega_{pe}^2 \frac{k_x^2}{k^2} \sin^2 \theta \right] F_{Ty}(\mathbf{k}) = \Gamma'_{Ty}(\mathbf{k}) - \frac{N_0}{N_g} \omega_{pe}^2 \frac{k_x^2}{k^2} \sin \theta \cos \theta F_{Tz}(\mathbf{k}) \quad (\text{A20})$$

$$\left[R(k) + \frac{N_0}{N_g} \omega_{pe}^2 \cos^2 \theta \right] F_{Tz}(\mathbf{k}) = \Gamma'_{Tz}(\mathbf{k}) - \frac{N_0}{N_g} \omega_{pe}^2 \sin \theta \cos \theta F_{Ty}(\mathbf{k}) \quad (\text{A21})$$

where

$$R(k) = \frac{N_0}{N_g} \left(\omega_{pe}^2 + \frac{k^2 c^2}{V^2 |S(k)|^2} \right).$$

The simulation code solves Eqs. (A19)-(A21) for the transverse electric force. The terms on the right-hand side of Eq. (A19)-(A21) involving the transverse electric force are set to zero for the first solution. Previous iteration values are used for subsequent solutions.

REFERENCES

1. H. Alfvén, *Nature* **150**, 405 (1942).
2. V.V. Dolgoplov and K.N. Stepanov, *Nucl. Fus.* **5**, 276 (1965).
3. V.V. Dolgoplov and K.N. Stepanov, *Sov. Phys. Tech. Physics* **11**, 741 (1966).
4. A. Hasegawa and L. Chen, *Phys. Rev. Lett.* **32**, 454 (1974).
5. A.A. Tataronis and W. Grossman, *Z. Physik* **16**, 667 (1973).
6. B. Balet, K. Appert and J. Vaclavik, *Plasma Phys.* **24**, 1005 (1982).
7. K. Appert, R. Gruber, F. Troyon, and J. Vaclavik, *Plasma Phys.* **24**, 1147 (1982).
8. K. Appert, B. Balet, R. Gruber, F. Troyon, T. Tsunematsu, and J. Vaclavik, *Nucl. Fus.* **22**, 903 (1982).
9. K. Appert and J. Vaclavik, *Plasma Phys.* **25**, 551 (1973).
10. A. Hasegawa and L. Chen, *Phys. Rev. Lett.* **35**, 370 (1975).
11. A. Hasegawa and L. Chen, *Phys. Fluids* **19**, 1924 (1976).
12. D.W. Ross, G.L. Chen and S.M. Mahajan, *Phys. Fluids* **25**, 652 (1982).
13. S.M. Mahajan, D.W. Ross and G.L. Chen, *Phys. Fluids* **26**, 2195 (1983).
14. S.N. Golvato, J.L. Shohet and J.A. Tataronis, *Phys. Rev. Lett.* **37**, 1272 (1976).
15. S.N. Golvato and J.L. Shohet, *Phys. Fluids* **21**, 1421 (1978).
16. T. Obiki, T. Mutoh, S. Adachi, A. Sasaki, A. Iiyoshi, and K. Uo, *Phys. Ref. Lett.* **39**, 812 (1977).
17. R.A. DeMirkhanov, A.G. Korov, S.N. Lozovskij, F.M. Nekrasov, A.G. Elfimov, S.E. Il'inskij, and V.V. Onishenko,

- Plasma Phys. Cont. Fus. Res. (IAEA Vienna 1977) **3**, 31.
18. A. Chambrier, A.D. Cheetham, A. Heym, F. Hofmann, B. Joye, R. Keller, A. Lietti, J.B. Lister, and A. Pochelon, Plasma Phys. **24**, 893 (1982).
 19. A. deChambrier, A. Heym, F. Hofmann, B. Joye, R. Keller, A. Lietti, J.B. Lister, P.D. Morgan, M.J. Peacock, A. Pochelon, and M.F. Stap, Plasma Phys. **25**, 1021 (1983).
 20. R. Behn, A. deChambrier, G.A. Collins, P-A. Dupperrex, A. Heym, F. Hofmann, Ch. Hollenstein, B. Joye, R. Keller, A. Lietti, J.B. Lister, J-M. Moret, S. Nowak, J. O'Rourke, A. Pochelon, and W. Simm, Plasma Phys. and Cont. Fusion **26**, 173 (1984).
 21. K. Appert, G.A. Collins, F. Hofmann, R. Keller, A. Lietti, J.B. Lister, A. Pochelon, and L. Villard, Phys. Rev. Lett. **54**, 1671 (1985).
 22. T.E. Evans, P.M. Valanju, J.F. Benesch, Roger D. Bengtson, Y-M. Li, S.M. Mahajan, M.F. Oakes, D.W. Ross, X-Z. Wang, J.G. Watkins, and C.M. Surko, Phys. Rev. Lett. **53**, 1743 (1984).
 23. F.D. Witherspoon, S.C. Prager and J.C. Sprott, Phys. Rev. Lett. **53**, 1559 (1984).
 24. J.A. Ionson, A.P. J. **226**, 318 (1978).
 25. C.K. Goertz, Planet. Space Sci. **32**, 1387 (1984).
 26. A.T. Lin, C-C. Lin and J.M. Dawson, Phys. Fluids **25**, 646 (1982).
 27. A.T. Lin and C-C. Lin, Phys. Fluids **26**, 3612 (1983).
 28. A.J. Lin and C-C. Lin, Phys. Fluids **27**, 2208 (1984).

29. B.L. Smith, H. Okuda and H. Abe, Phys. Fluids **28**, 1772 (1985).
30. V.K. Decyk, J.M. Dawson and G.J. Morales, Phys. Fluids **22**, 507 (1979).
31. V.K. Decyk, G.J. Morales and J.M. Dawson, Phys. Fluids **23**, 826 (1980).
32. H. Abe, R. Itatani and H. Momota, Phys. Fluids **22**, 1533 (1979).
33. N. Nakajima, H. Abe and R. Itatani, Phys. Fluids **25**, 2234 (1982).
34. J. Busnardo-Neto, J.M. Dawson, T. Kamimura, and A.T. Lin, Phys. Rev. Lett. **36** 28 (1975).
35. J.M. Kinder, A.T. Lin, J.M. Dawson, and R. Martinez, Phys. Fluids **24**, 498 (1981).
36. H. Abe, H. Okada, R. Itatani, M. Ono, and H. Okuda, Phys. Rev. Lett. **53**, 1153 (1984).
37. K. Sakai, S. Takeuchi, M. Matsumoto, and r. Sugihara, Plasma Phys. Cont. Fus. Res. (IAEA Vienna 1984), 546.
38. C.K. Birdsall and A.B. Langdon, *Plasma Physics Via Plasma Simulation* (McGraw-Hill, Inc., 1985).
39. R.W. Hockney and J.W. Eastwood, *Computer Simulation Using Particles* (McGraw-Hill, Inc., 1981).
40. J.M. Dawson, Rev. Mod. Phys. **55**, 403 (1983).
41. W.W. Lee and H Okuda, J. Comp. Phys. **26**, 139 (1978).
42. R.J. Mason, J. Comp. Phys. **41**, 233 (1981).
43. J. Denavit, J. Comp. Phys. **42**, 337 (1981).
44. D.C. Barnes, T. Kamimura, J-N. Lebouef, and T. Tajima, J.

- Comp. Phys. **52**, 480 (1983).
45. C.G. Darwin, *Phil. Mag.* **39**, 537 (1920).
 46. W.W. Lee, M.S. Chance and H. Okuda, *Phys. Rev. Lett.* **46**, 1675 (1981).
 47. H. Alfvén, *Cosmical Electrodynamics*, (Clarendon Press, Oxford, 1950).
 48. J. Busnardo-Neto, P.L. Pritchett, A.T. Lin, and J.M. Dawson, *J. Comp. Phys.* **23**, 300 (1977).
 49. C.W. Nielson and H.R. Lewis, in *Methods in Computational Physics*, Vol. 16, (J. Killeen, Ed., Academic Press, New York, 1976).
 50. H. Naitou, S. Tokuda and T. Kamimura, *J. Comp. Phys.* **33**, 86 (1979).
 51. H. Naitou, S. Tokuda and T. Kamimura, *J. Comp. Phys.* **38**, 265 (1980).
 52. M.B. Priestley, *Spectral Analysis and Time Series*, Vol. 1, (Academic Press, London, 1981).
 53. T. Kamimura, T. Wagner and J.M. Dawson, *Phys. Fluid* **21**, 1151 (1978).
 54. E. Parzen, *Technometrics* **3**, 167 (1961).
 55. S. Ichimaru, *Basic Principles of Plasma Physics*, (W.A. Benjamin, Inc., Reading, Massachusetts, 1973).
 56. C. Chu, J.M. Dawson and H. Okuda, *Phys. Fluids* **12**, 1762 (1975).
 57. L. Landau and E. Lifshitz, *Statistical Physics" Part 1* (Pergamon Press, Elmsford, New York, USA, 1980) 3rd Ed.
 58. A.B. Langdon and C.K. Birdsall, *Phys. Fluids* **13**, 2115 (1970).

59. A.G. Sitenko, *Electromagnetic Fluctuations in Plasma* (Academic Press, New York, NY, 1967) p. 78.
60. C. Chu, M.S. Chu and T. Ohkawa, *Phys. Rev. Lett.* **41**, 653 (1978).
61. D.W. Swift and J.J. Ambrosiano, *J. Comp. Phys.* **44**, 302 (1981).
62. H. Grad, *Phys. Today* **22**, 34 (1969).
63. T.H. Stix, *2nd International Symposium on Heating in Toroidal Plasmas* (Cuomo, Italy, 1980).
64. T.E. Evans, Ph.D. dissertation.
65. Y.M. Li, S.M. Mahajan and D.W. Ross, FRCR#276, The University of Texas at Austin (1985).

VITA

James Leonard Geary Jr. was born on January 11, 1954, in Creston, Iowa, the son of James Leonard Geary and Norma Ann (Davis) Geary. After completing his high school education at Orient-Macksburg High School in Orient, Iowa, he entered the Massachusetts Institute of Technology in the Fall of 1972. In May, 1976, he received the degree of Bachelor of Science in Physics. In September, 1977, he entered The University of Texas at Austin and has been employed as research assistant since January, 1978. On November 1, 1980 he was married to Helena Yau-Choi Luk.

Permanent Address: 611 New York Avenue
Hillcrest Acres Mobile Home Court
Creston, Iowa 50801

ERRATUM

COMPUTER SIMULATION OF DRIVEN ALFVÉN WAVES

James Leonard Geary, Jr.

Institute for Fusion Studies

The University of Texas at Austin

Austin, Texas 78712-1060

Page 68.— The top equation of the page should be corrected to read:

$$\frac{\langle B^2 \rangle_{\mathbf{k}}}{8\pi} = \int_{-\infty}^{\infty} \times \frac{T^i k^2 v_A^2}{\omega \omega_{pi}^2} \frac{[\omega^2(k^2 c^2 + \omega_{pi}^2) - k^2 c^2 \Omega_i^2]}{(\omega - \omega_w)} \left[\frac{\delta(\omega - \omega_s)}{(\omega + \omega_s)} + \frac{\delta(\omega + \omega_s)}{(\omega - \omega_s)} \right] d\omega$$

Page 73 — Equation (2.88) should have the form:

$$\frac{\langle B^2 \rangle_{\mathbf{k}}}{8\pi} = \frac{T}{2} \frac{k^2 c^2 \omega_{pe}^2}{(k^2 c^2 + \omega_{pi}^2)} \frac{1}{(\omega_{pe}^2 + k^2 c^2 + \omega_{pi}^2)}. \quad (2.88)$$